

Effects of Spin-Dependent
Polariton-Polariton Interactions in
Semiconductor Microcavities: Spin Rings,
Bright Spatial Solitons and Soliton Patterns

Maksym Sich

Department of Physics and Astronomy
The University of Sheffield

Physics PhD Thesis

April 2013

Contents

Abstract	5
Acknowledgements	7
1 Introduction	9
1.1 Microcavity polaritons	12
1.2 Condensation of polaritons	16
1.3 Polariton optical parametric amplifier and optical parametric oscillator	20
1.4 Bistability	23
1.4.1 Bistability and parametric instability in the OPO	24
1.5 Polariton polarisation multistability	26
1.6 Effects of interactions in polariton high density states	32
1.7 Polariton spatial solitons	36

1.7.1	Oblique dark solitons	36
1.7.2	Propagating wavepackets	37
1.7.3	Dissipative solitons	39
1.7.4	Known solutions for dissipative polariton spatial solitons	40
1.7.5	Other suggestions	45
1.8	Experimental techniques	46
1.8.1	Near-field and far-field imaging	47
1.8.2	Streak-camera	49
1.8.3	Core experimental setup	50
2	Spin rings	53
2.1	Observation of polarisation multistability	54
2.2	Measurement of cross-polarisation interactions	58
2.3	Observation of spin rings	59
2.4	Discussion and conclusions	61
3	Bright polariton solitons	65
3.1	Experimental setup	67

3.2	Observation of bright polariton solitons	69
3.2.1	Negative effective mass	69
3.2.2	Bistability	70
3.3	Characterisation of solitons	73
3.3.1	Soliton velocity	73
3.3.2	Soliton size	75
3.3.3	Soliton intensity	76
3.3.4	Soliton energy-momentum spectrum	78
3.3.5	Soliton sustainability	82
3.4	Coherent control of soliton	83
3.5	Comparison with the TOPO	87
3.6	Discussion and conclusions	90
4	Polarisation properties of polariton solitons	93
4.1	Experimental setup	94
4.2	Soliton polarisation multi-state behaviour	98
4.3	Linearly polarised pump and writing beam	104
4.4	Discussion and conclusions	106

5	Polariton soliton arrays	109
5.1	Experimental setup	110
5.2	Observation of soliton trains	111
5.3	Soliton-soliton interactions	113
5.4	Discussion and conclusions	120
6	Conclusions and future plans	123
	Bibliography	125

Abstract

Semiconductor microcavity polaritons are composite half-light half-matter quasiparticles that arise from strong coupling of photons and excitons in semiconductor microcavities. Polaritons have recently been demonstrated to exhibit rich physical properties resulting from polariton-polariton interactions, such as non-equilibrium condensation, parametric scattering and superfluidity.

This work is focused on exploring spin-dependent polariton-polariton interactions and their implications. In the second chapter polariton polarisation multistability is studied. Spin-rings resulting from the multistability are reported and characterised.

In the third chapter bright spatial polariton solitons arising from polariton modulational instability are reported and thoroughly characterised. The fourth chapter deals with the polarisation properties of polariton solitons, which are closely linked to polariton polarisation multistability. Finally, in the fifth chapter, the formation of soliton arrays (trains) is demonstrated along with possible soliton-soliton interactions.

Acknowledgements

First of all I want to thank my father without whose insistence I would not have embarked on a PhD route.

I greatly thank Prof. Maurice Skolnick and Mrs Catherine Annabel for finding a way through bureaucratic thorns for me.

Support, foresight and persistence of Dr Dmitry Krizhanovskii brought us to fruitful results, I am thankful for this rich and memorable experience. I also thank Prof. Maurice Skolnick for his supervision and advice.

I am very grateful to everyone in the LDS group for their very warm welcome when I arrived at the university and for the nice and friendly atmosphere always present in our labs and offices. Also I have to mention that without Matt I may have not been able to come to Sheffield at all. François, thank you very much for the exciting philosophical discussions and productive co-operation in the lab.

Finally, I express my greatest gratitude to my Wife, my Family and my Friends for your constant support and understanding.

Chapter 1

Introduction

The year 2012 marked the 20th anniversary of the first observation of exciton-polaritons in semiconductor microcavities [1], which triggered a rapid development in the field of semiconductor polariton physics. The first prediction of strong coupling between excitons and light was made by the Ukrainian physicist S. I. Pekar [2]. The term *polariton* was introduced by J. J. Hopfield [3] and V. M. Agranovich [4] in order to describe coupling between light (photons) and electric dipoles (excitons) in bulk crystals. In the present work 2D exciton-polaritons (referred to in the text also as polaritons) in microcavity devices are studied. These devices are GaAs-based planar microcavities with distributed Bragg reflectors with embedded GaAs or InGaAs quantum wells, where excitons are excited.

Polaritons have been recently demonstrated to exhibit a number of fundamental physical effects: condensation [5], superfluidity [6], parametric scattering [7], quantised vortices [8] and dark oblique solitons [9].

This work complements an important link between two fields of the

fundamental interest: polariton physics and soliton physics. The study of solitons, which emerged from J. S. Russell's experiment on water waves [10] (figure 1.1(1)), can be found in many areas. Solitons are the temporal or spatial waves that are localised and stabilised through non-linear interactions. Solitary waves in oceans and seas are often formed in straits [11, 12], for example see figure 1.1(2). In the sky, clouds that form with air flows over specific topological objects are also believed to be stable solitary structures [13, 14, 15] (figure 1.1(3)). Even ball lightning can be possibly described as a soliton [16].

In the field of nonlinear optics bright and dark solitons have been demonstrated in different media. $\chi(2)$ quadratic solitons result from second-harmonic generation from input fundamental fields (at frequency ω), and mix via $\chi(2)$ to generate a second harmonic (2ω). The conversion requires wave vector conversion which results in modification of dispersion which stabilises these wavepackets [17]. Kerr-type solitons resulting from the Kerr nonlinearity (when $\Delta n \sim E^2$) were observed in a planar glass waveguide [18]. Solitons arising in saturable self-focusing nonlinear medium (low pressure rubidium vapour) were also extensively studied [19]. In photorefractive medium, in contrast to Kerr nonlinearity, focusing effect is produced by an internal nonlocal space-charge DC field. Incident light on such a medium through two-wave mixing (interference) induces local interference gratings which then localise input light [20]. Low power densities and independence of focusing properties on beam power allowed the observation of complicated soliton patterns (figure 1.1(5)) [21] and soliton-soliton interactions (figure 1.1(6)) [22].

Finally solitons have been observed in optical fibres [26, 27, 28] and fi-

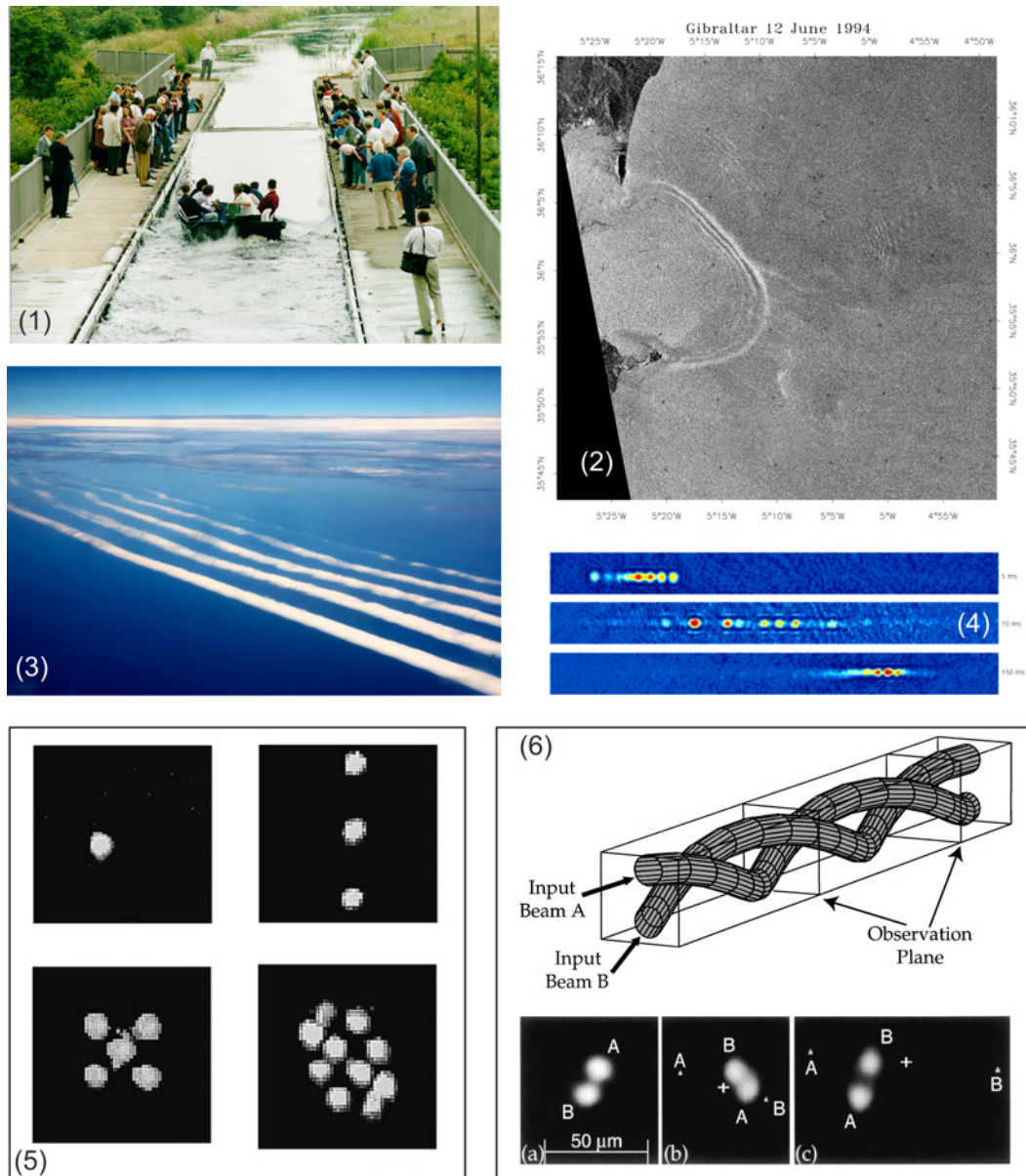


Figure 1.1. (1) - a photo of reconstruction of the soliton observed by J. S. Russell. Source: [23]. (2) - satellite photon of solitons propagating in Mediterranean sea from Gibraltar strait. Source: [12]. (3) - photo of a Morning Glory cloud formation. Source: [24]. (4) - Soliton trains formed from atomic BEC. Source: [25]. (5) - weakly interacting localised structures (solitons) in a photorefractive oscillator system (BaTiO_3) with nonlinear saturable absorber. Once it is in a special shape optical resonator (confocal ring resonator in this case) it respond with the self-build up of gratings in the crystal and formation of stable soliton beams. Source: [21]. (6) Spiralling of solitons induced by phase engineering in photorefractive Strontium-Barium Niobate crystal. Source: [22].

bre ring cavities [29], atomic condensates (figure 1.1(4))[30, 25] and VCSELs (essentially microcavities in the weak coupling regime) [31, 32, 33, 34]. The latter is closely linked to the solitons discussed in this work. The solitons in VCSELs are also stabilised via resonator bistability.

§ 1.1 Microcavity polaritons

A typical structure of a microcavity used is schematically shown in figure 1.2. It consists of two distributed Bragg reflectors (DBR) forming the cavity with quantum wells incorporated into the cavity active region. Quantum wells (QWs), which are positioned at the antinodes of the optical field confined by the microcavity, are used to localise direct excitons in the plane of the cavity. Excitons in QWs possess larger oscillator strength than in bulk due to confinement. This configuration allows for better coupling efficiency between excitons and photons, and, crucially, creates a 2D polariton system.

First of all, the dispersion of the system will be discussed. The photons in an empty microcavity generally obey the following quadratic dispersion relation:

$$\omega_c = \frac{2\pi c}{n_c L_c} + \frac{\hbar k_{xy}^2}{2m_{ph}}, \quad (1.1)$$

where L_c is effective length of the cavity, n_c is the refractive index, $m_{ph} = \hbar n_c / (c L_c)$ is the effective mass of a photon, which is very light comparing to free exciton mass: typically $m_{ph} \approx 10^{-5} - 10^{-4} m_0$. This dispersion is depicted in figure 1.3 (black dashed line). At the same time, since the exciton mass

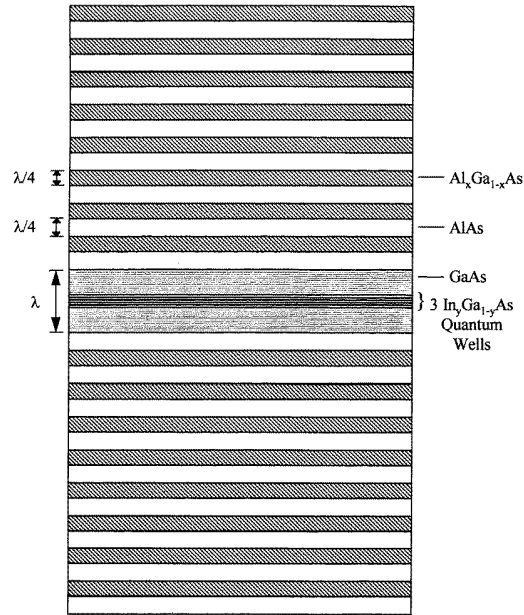


Figure 1.2. A schematic diagram of a λ GaAs microcavity with embedded quantum wells. Source: [35].

is $m_{ex} \approx 10^{4-5} m_{ph}$, the exciton dispersion is nearly constant for a range of k-vectors of excitons which are optically active [36, 37, 38]. This is shown by red dashed line in figure 1.3.

Strong coupling between photons and excitons is most efficient when the values of their energies and momenta in the cavity are in resonance. The coupling between excitons and photons is determined by the oscillator strength of the exciton and the amplitude of the cavity photon electromagnetic field at the location of the QW. If the coupling strength is greater than the width of the cavity photon and exciton mode the so-called strong coupling regime occurs. In this regime energy oscillates between the exciton and the cavity photon mode resulting in the formation of hybrid light-matter quasiparticles termed polaritons. These oscillations are called Rabi oscillations. Rabi frequency is a characteristic of the coupling energy between the excitons and the photons in the cavity. This splitting can be ex-

pressed as [35]:

$$\hbar\Omega_0 \approx 2\hbar \left(\frac{2\Gamma_0 c N_{QW}}{n_c L_c} \right)^{1/2}, \quad (1.2)$$

where N_{QW} is the number of quantum wells in the cavity, Ω_0 is the Rabi frequency and $\hbar\Gamma_0 \sim f_{ex}$ is the radiative width of a free exciton, which is proportional to the oscillator strength of the exciton (f_{ex}). Qualitatively the polariton can be considered as follows: a photon with wavevector k is absorbed by the QW, which creates an exciton with the same k vector. The exciton emits a photon and so-on, until the photon escapes or the exciton scatters.

Typical polariton dispersion is shown in figure 1.3. Anticrossing between the exciton and the cavity modes leads to the appearance of the upper (UPB) and the lower (LPB) polariton branches in the vicinity of the strong coupling region. This work will be concerned with the lower polariton branch.

An important characteristic of the lower polariton branch relevant to soliton studies here is the polariton effective mass defined as follows:

$$m^* = \frac{\hbar^2}{\partial^2 E / \partial k^2}. \quad (1.3)$$

It is instructive to analyse the effective mass pattern of the lower polariton branch as a function of k -vector. The dispersion and derived effective mass are shown in figure 1.4. Importantly, the dispersion curve has the point of inflection which separates two regions with different signs of effective mass.

Finally, it is important to highlight effects of saturation of excitonic

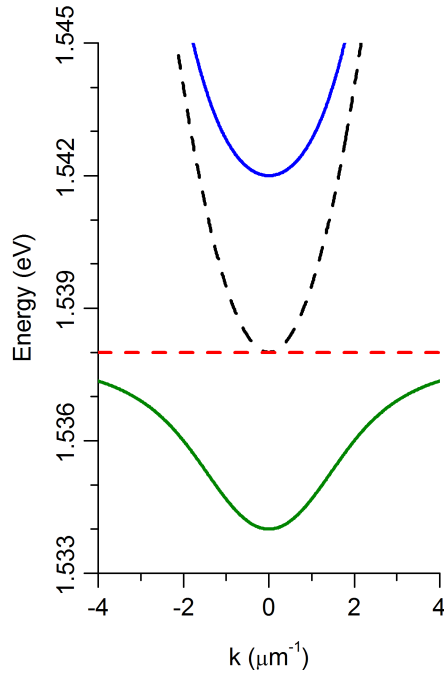


Figure 1.3. Simulated polariton dispersion of a typical GaAs microcavity. Black dashed line is dispersion of uncoupled photons, red dashed - uncoupled exciton, blue solid - upper polariton branch and green solid - lower polariton branch.

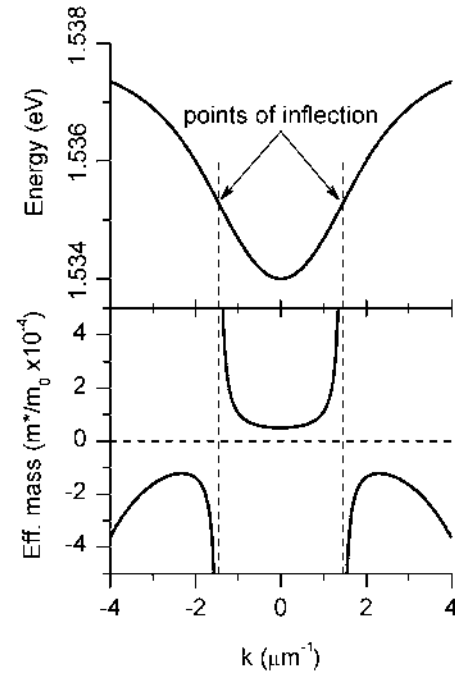


Figure 1.4. Lower polariton branch (the same as in figure 1.3), upper panel, and corresponding effective mass, lower panel, as a ratio to free electron mass (m_0) show two points of inflection which divide regions of positive and negative effective masses of polaritons.

resonance, in the case of high densities. It was shown for the 1s excitonic resonance that with increasing density Coulomb exchange interaction between excitons increases, which leads to a blueshift and exciton dephasing. The increased role of dephasing mechanisms also leads to a broadening of the exciton resonance while the exciton oscillator strength is almost not affected. This leads to a blueshift of the LPB and its broadening, but there is no significant reduction in coupling strength until the exciton is fully saturated [39]. At higher density, particle-particle interactions may lead to fast exciton ionisation and, as a result, collapse of strong exciton-photon coupling.

§ 1.2 Condensation of polaritons

The concept of what is now called Bose-Einstein condensate (BEC) was developed at the dawn of the Quantum Physics by Einstein in 1924-1925 in a series of three papers, and was specifically discussed in the second one [40]. Einstein's work was closely bound to the ideas expressed by Bose [41], where he proposed a derivation of the famous Planck's formula for black body radiation based on the statistical description of quanta of light. The same quantum statistical approach led Einstein to predict a phase transition in a gas of noninteracting atoms. This phase transition (Bose-Einstein condensation) occurs when a large number of atoms condenses in the state of lowest energy.¹

In 1938 Kapitza [44] and Allen & Meissner [45] discovered superfluidity of liquid helium. The intuition behind this discovery, that it may be a manifestation of BEC [46, 47], quickly led to the development of superfluidity theory by Landau [48] in 1941. Finally, Landau & Lifshitz [49] and Penrose [50] in 1951 introduced the concept of offdiagonal long-range order, corresponding to a δ -like term in the ground state of momentum distribution. Presence of this term is now considered a litmus test for determination of BEC.

It was only in 1995 that BEC was firstly reliably observed in Rb-89 atoms [51]. Excitons also have integer spin and comparably light mass, and observation of exciton BEC was first claimed in 2002 [52, 53]. Photons (ef-

¹Notably, Bose and Einstein's work appeared before Fermi's [42]. Furthermore, it was only 1927 when all particles were finally classified into bosons and fermions depending on their spin [43].

fective mass $\approx 10^{-6}m_e$) are even lighter and their BEC can be observed even at room temperatures, which was only observed in 2010 [54]. These are just three benchmarking experiments, but discussion of BEC is an incredibly rich topic, which is generally beyond the scope of this work. However, several main features of polariton condensation should be highlighted for a comprehensive discussion of polariton solitons.

Photons have spin $s_{ph} = 1$. Excitons are composed of electrons with $s_e = 1/2$ and heavy holes with $s_h = 3/2$ and therefore exciton spin is also integer: $s_{ex}^b = 1, s_{ex}^d = 2$ ². Excitons with spin $s_{ex}^b = 1$ are called bright, since they can interact with photons as they have the same spin, and therefore can be detected with light. Polaritons, therefore, also have integer spin and exhibit bosonic behaviour. Polaritons have very low in-plane effective mass (10^9 lighter than Rubidium atoms used to demonstrate Bose-Einstein condensation [51] and 10^5 lighter than the mass of an electron). As it was already mentioned, it is possible to show [56] that particles obeying Bose-Einstein statistics at high enough densities (overlapping between wavefunctions of separate particles should be of the order of their de-Broglie wavelength) and low enough temperatures can undergo a phase transition from a Bose gas to a condensate – the lowest energy macroscopically occupied state. The condensate can then be described by a single macroscopic wavefunction.

Microcavity polaritons are a two-dimensional system. For an equilibrium noninteracting Bose gas, Bose-Einstein condensation at finite temperature is only possible when it has more than two dimensions; for two-dimensional systems condensation can only occur at $T = 0$. However, in the case of a weakly interacting equilibrium Bose gas, it can undergo quasi-

²Although, separate excitons possibly may not behave as bosons, an exciton gas behaves as a Bose gas [55].

condensation at temperatures below T_{BKT} (so-called Berezinskii-Kosterlitz-Thouless transition) [56]. The condensate wavefunctions exhibit a macroscopic coherence length which does not extend to infinity (in contrast to the strict BEC).

Excitons and polaritons in the system with high wave-vectors have to go through relaxation processes in order to reach the region of strong coupling. To do so they have to dissipate a large amount of energy (5-10 meV) comparing to a typical energy loss from a single polariton-phonon scattering event (≈ 1 meV), each of which takes about 10 ps. Although the phonon energy in semiconductors can range from 0 to 30 meV, 1 meV is the energy that corresponds to a phonon wavelength of 10 nm – the typical size of QW [57, 58, 59]. Since the polariton lifetime is ≈ 5 ps, the scattering rate to the lowest energy polariton states is low enough to prevent polaritons from achieving thermodynamic equilibrium. As a result, most polaritons accumulate at high-k states close to the exciton level. This is referred to as a bottleneck effect [59, 60]. However, at high enough powers, polariton-polariton scattering dominates allowing efficient relaxation to the bottom of the LPB, which can be achieved either using non-resonant excitation or resonant laser excitation into the LPB. Although, the limited polariton lifetime does not allow the polariton system to fit into a semi-classical description of condensation (as in [61]), there are now several claims that quasi thermal equilibrium can be achieved with some effective temperature, but not in thermal equilibrium with the crystal lattice. However, the recent observation of polariton lifetimes of the order of a 100 ps [62] can possibly challenge this problem and provide condensates in equilibrium with the crystal lattice.

It is now common to refer to the condensate that can be created in the polariton system as the polariton Bose-Einstein condensate, which is a relaxed definition, and the discussion is still open [63, 64]. The modern definition of BEC stipulates that it is a build-up of long range spatial coherence, with no strict demand for thermal equilibrium, which perfectly fits the polariton system.

Independently of the outcome of the discussion, it is important to highlight the key properties of the state: it is a high density macroscopically occupied energy state. It possesses a high degree of spatial and temporal coherence, i.e. it is narrow in momentum and energy space. The coherence time of the polariton condensate $\tau_{cc} \sim N_{pol}\tau_1$ (τ_1 – polariton lifetime) was measured to be of the order of 200-500 ps [65, 66]. Recently the coherence time of polariton condensates was reported to reach 3 ns [67].

The demonstration of coherence and occupation of the lowest energy state via off-resonant pumping [5] led to wider acceptance of polariton condensation. The famous illustration (figure 1.5) shows the build-up of population and finally condensation of polaritons. Condensation of polaritons in GaAs-based microcavities has been also demonstrated, for instance in a trap created within a small area where an external mechanical force was applied [68]. Finally, polariton lasing and condensation has been demonstrated in microcavity pillars and wires [69, 70, 71].

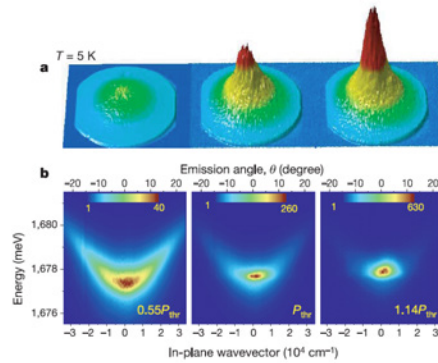


Figure 1.5. (a) top row images show far-field angular emission intensity distribution, (b) bottom row images show energy resolved data from (a). Left panels - pump below threshold, centre at the threshold, right - above the threshold. Source: [5].

§ 1.3 Polariton optical parametric amplifier and optical parametric oscillator

A major advance in polariton physics was the discovery of parametric polariton-polariton scattering [60, 7] where the cavity is pumped at a certain incident angle with respect to the normal to the sample with the pump photon energy matching polariton energy at that k -vector. As the result of polariton-polariton interactions in the pump, one polariton is scattered to the signal state at $k_{signal} = 0$ and second is scattered to the idler state $k_{idler} = 2k_{pump}$.

The scattering processes were observed in an *optical parametric amplifier* (OPA) configuration [72]. In this experiment, the probe applied at $k = 0$ triggers scattering processes of the pump polaritons (see figure 1.6) to this state, therefore no scattering self-organisation occurs. These results were shortly followed by a theoretical explanation [73].

The coherence of the signal polariton population (at $k = 0$) was studied

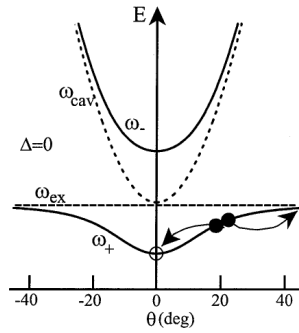


Figure 1.6. Polariton dispersion relation vs incident angle θ at zero detuning. Cavity (exciton) energies ω_{cav} (ω_{ex}) shown dashed. Probe polariton (o) stimulates the scattering of pump polaritons (•). Source: [72].

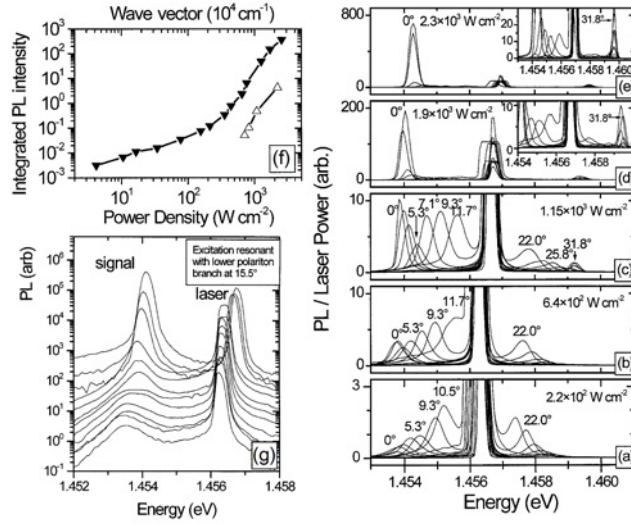


Figure 1.7. PL spectra (a) below and (b) close to threshold, (c), (d), (e) above threshold as a function of detection angle. A very strong change is seen between low and high excitation power. (f) PL intensity collected from $k = 0$ as a function of pump power demonstrating threshold behaviour. (g) PL spectra collected at $k = 0$ as a function of pump power demonstrating energy blue-shift. Source: [7].

by means of coherent control [74] of the OPA. First, a 1 ps pulse was applied at non-zero incidence angle to create a pump population. Then two phase locked probe pulses were sequentially applied to the sample at normal incidence. The first of the probe pulses above certain threshold, I_0 , triggered stimulated scattering of the pump polaritons into the $k = 0$ state. Then the second probe pulse seeded polaritons that would interfere with the existing population at $k = 0$. The results show (figure 1.8) high coherence of polaritons at $k = 0$, and very long coherence times (figure 1.9) much longer than 10 ps.

When a pump beam is used alone and is applied resonantly to the microcavity, at high power excitations (above a certain threshold) stimulated scattering occurs (so-called self-organisation of multiple polariton-

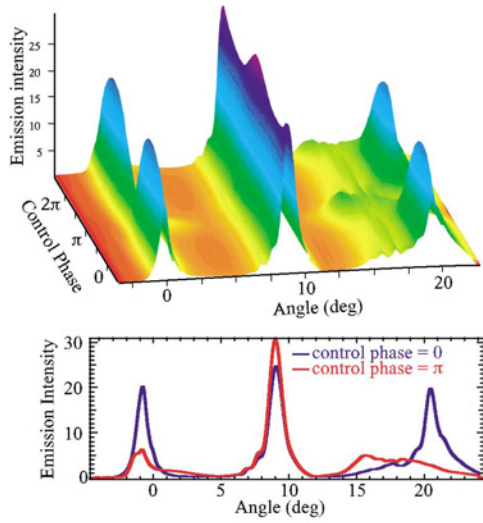


Figure 1.8. Angular pattern of the emission in transmission geometry as a function of the control phase (time delay 2ps). The lower panel shows plots for constructive and destructive control phase. Source: [74].

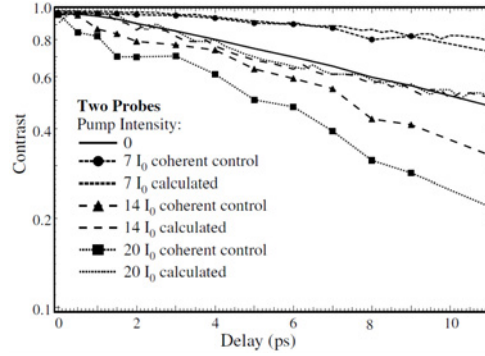


Figure 1.9. Contrast of coherent control oscillations versus the delay between the two probe pulses; the first probe pulse is synchronous with the pump. I_0 is the threshold intensity of the first probe which triggers stimulated scattering. Source: [74].

polariton scattering [75]). When the occupancy of the final state ($k_{\text{signal}} = 0$) becomes close to 1, *stimulated* scattering of polaritons into this state occurs. As a result the final state becomes macroscopically occupied. This process is referred to as the *optical parametric oscillator* or the *OPO*. Three coupled states – pump, signal and idler – form the OPO. It is notable that scattering to many states is allowed by energy and momentum conservation rules, but at high power self-organisation occurs with only one signal state at $k \approx 0$ strongly amplified [75].

Experimentally, PL emission exhibits a threshold-like behaviour as a function of the CW pump power (figure 1.7(f)) [7], and PL emission is also concentrated around $k = 0$ (figure 1.7(a)-(e)) with $\Delta k = \pm 2^\circ$ and linewidth narrowing is observed. Based on the above observations and given the bosonic nature of polaritons, the authors suggested that the ob-

served threshold behaviour may be a transition to a condensate phase. Also polariton-polariton interactions at the higher pump powers lead to renormalisation of the polariton dispersion which manifests itself as a blueshift in the observed emission energy at high pump powers (figure 1.7(g))³. The efficiency of this process is much higher than that of off-resonant excitation since the population of the exciton reservoir is avoided.

The coherence time of the final state was measured to be of the order of 500 ps [66]. It was suggested also that it is limited by interactions and particle fluctuations in the pump, signal and idler states.

§ 1.4 Bistability

The effect of *bistability* in polariton systems is a consequence of polariton-polariton interactions. It was first demonstrated by applying a slightly blueshifted pump beam with respect to the LBP at $k = 0$ [77, 78]. As the pump intensity is increased it creates more polaritons which leads to renormalisation of the polariton dispersion, which shifts upwards in energy. Once the blueshift of the lower polariton branch is high enough (higher bistability threshold) to match the pump laser energy, a sharp increase in transmission (or increase in amplitude of internal cavity field) is observed. Then if the pump intensity is decreased, the polariton resonance will remain at the same energy (as that of the pump) and maintain a high transmission

³The blueshift of the LPB at high densities of polaritons enables them to screen potential disorder and to overcome TE-TM splitting [76].

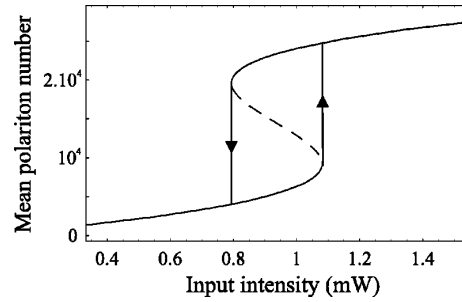


Figure 1.10. Calculation of intensity of the polariton field (the mean number of polaritons) vs the input power I_{in} in milliwatts. The spot size is taken $50 \mu\text{m}$ in diameter. The cavity and exciton linewidths are $\gamma_c = 0.12 \text{ meV}$ and $\gamma_{exc} = 0.075 \text{ meV}$. The cavity-exciton detuning is $\delta = 0$. The laser detuning is $\delta_{pump} = 12.5\gamma_{polariton}$. In the bistable region, the dotted line is the unstable branch. The arrows indicate the hysteresis cycle obtained by scanning the input power in both directions. Source: [77].

rate until dispersion falls back to the un-blueshifted values (lower bistability threshold), see figure 1.10. In some cases this bistability range can reach up to 50% of the applied pump power.

§ 1.4.1 Bistability and parametric instability in the OPO

The polariton system in the OPO configuration, as it was noted before, undergoes a phase transition above a certain threshold power. In the case of the OPO, the pump only bistability threshold may coincide with the threshold for stimulated parametric scattering to $k \approx 0$ (which is also referred in some literature as *parametric instability* [79]). As a result the OPO emission may also exhibit hysteresis as a function of pump power [80, 75]. A general

condition for bistability in the OPO to appear can be written as [80]:

$$\Delta\Delta_{pump} > 1, \quad (1.4)$$

where $\Delta_{signal} = \Delta_{idler} = \Delta$ and Δ_{pump} are the signal, idler and pump detunings normalized to their half width at half maximum (HWHM) respectively. The first observation of bistability was made by Baas *et al.* [80]. The main result of their work is shown in figure 1.11. The extent of bistability and the actual threshold values depend on the angle of excitation. The threshold power of the OPO is $p \sim \sqrt{\gamma_{idler}\gamma_{signal}}$, where γ is the polariton relaxation rate at k-vectors of signal and idler [80]. Experimental and theoretical findings on this topic were summarised by Whittaker [81]. The key result can be seen in figure 1.12. It shows the s-shaped curve of the internal pump only field vs pump power and the angular range where the pump only state is unstable (shaded area). It breaks into signal and idler modes, which are always at $k_{signal} = 0$ and $k_{idler} = 2k_{pump}$. It was shown that hysteresis in the OPO emission is a result of interplay between bistability of the pump only mode and stimulated scattering [79].

Notably, the signal state (at high density phase) has very similar properties to condensates obtained via off-resonant pumping, discussed in section 1.2. Its high population is localised in the energy minimum at $k = 0$ and it is narrow in energy and momentum, and at the same time the signal has long-range spatial coherence. Importantly the coherence of the signal state is not inherited from the pump, since scattering to signal and idler states brings a random phase:

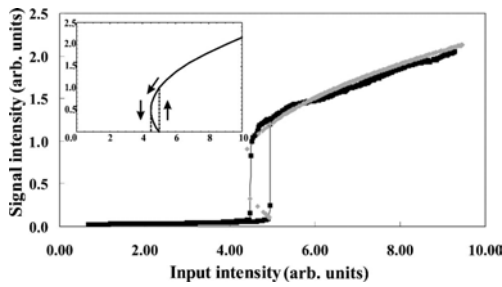


Figure 1.11. Variation of the signal emission as a function of the pump power for a pump detuning $\Delta_{pump} = 0.42\text{meV}$. The gray curve is the result of a fit. The inset shows more clearly the calculated unstable branch. Source: [80].

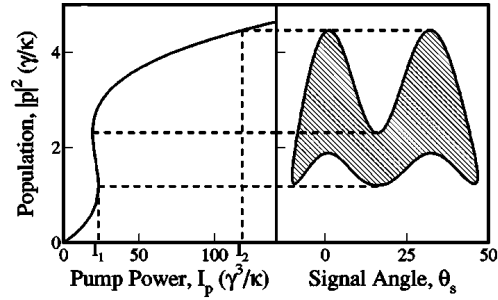


Figure 1.12. Left. S curve showing the bistable relationship between the pump polariton population and external pump power. Right. Values of polariton populations (shaded region) for which the pump only state is unstable as a function of the signal angle. Source: [81].

$$2\varphi_{pump} + \varphi_{signal} + \varphi_{idler} = 2\pi, \quad (1.5)$$

where φ_{signal} and φ_{idler} are random phases since only φ_{pump} is fixed [81, 82].

The coherence build-up is only seen in the high density state. Ultimately this state can also be referred to as a condensate, as it doesn't inherit its phase from the pump.

§ 1.5 Polariton polarisation multistability

Most of the effects studied in polariton physics are collective. A large number of polaritons is created and then some macroscopic characteristic is measured, i.e. intensity or density. The same applies to polarisation ef-

fects and measurements in microcavities. A single exciton spin in quantum wells has ± 1 and ± 2 projections along the growth axis. $|+1\rangle$ and $|-1\rangle$ excitons can be excited by (and can emit) σ^+ and σ^- photons. However the overall measured polarisation of the polariton gas can be any combination of these, which can be conveniently represented using the Poincaré sphere and Stokes vector formalism for a full polarisation description. In this work the following definitions are used for Stokes vector components:

$$\vec{S} = \begin{pmatrix} I \\ Q \\ U \\ V \end{pmatrix}, \quad (1.6)$$

where I is total intensity normalised to 1. Q is the degree of linear polarisation (DLP):

$$Q = \frac{I_x - I_y}{I_x + I_y}. \quad (1.7)$$

U is the degree of linear polarisation in the diagonal basis (DDP):

$$U = \frac{I_a - I_b}{I_a + I_b}. \quad (1.8)$$

V is the degree of circular polarisation (DCP):

$$V = \frac{I_l - I_r}{I_l + I_r} \equiv \frac{I_{\sigma^+} - I_{\sigma^-}}{I_{\sigma^+} + I_{\sigma^-}}. \quad (1.9)$$

Here I_x and I_y are intensities of polarisation components in the linear polarisation basis with horizontal and vertical axis orientation; I_a and I_b are

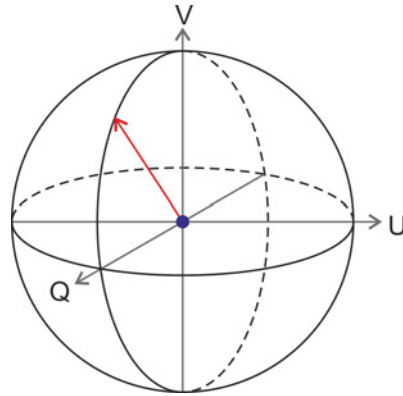


Figure 1.13. Poincaré sphere. Red vector depicts fully polarised light. Blue dot corresponds to fully unpolarised light.

when the axes are diagonal; I_l and I_r correspond to intensities in the left and right circularly polarised basis. The Poincaré sphere is a unit sphere where each of three orthonormal axis correspond to Q , U and V . Fully polarised light corresponds to a unit vector with the beginning in the centre of the sphere and the end on its surface. Fully unpolarised light corresponds to a zero length vector – a point in the centre (figure 1.13).

Polariton-polariton interactions are mediated by excitonic components of polaritons. The main mechanism responsible for polariton-polariton scattering is the Coulomb interaction between excitons [83]. Excitons participating in polariton formation are bright excitons with spin $|\pm 1\rangle$. According to the work by Ciuti *et al.* [84] $|+1\rangle = |\downarrow\uparrow\rangle$ (single and double arrows correspond to electron and hole spins respectively) exciton can only directly scatter with exciton with the same spin, while scattering of polaritons with opposite spins $|\downarrow\uparrow\rangle \otimes |\uparrow\downarrow\rangle$ can only happen via dark exciton states which can be described as follows:

$$|\downarrow\uparrow\rangle \otimes |\downarrow\uparrow\rangle \rightarrow |\downarrow\uparrow\rangle \otimes |\downarrow\uparrow\rangle, \quad (1.10)$$

$$|\uparrow\downarrow\rangle \otimes |\uparrow\downarrow\rangle \rightarrow |\uparrow\downarrow\rangle \otimes |\uparrow\downarrow\rangle, \quad (1.11)$$

$$|\downarrow\uparrow\rangle \otimes |\uparrow\downarrow\rangle \rightarrow |\downarrow\downarrow\rangle \otimes |\uparrow\uparrow\rangle \rightarrow |\uparrow\downarrow\rangle \otimes |\downarrow\uparrow\rangle, \quad (1.12)$$

$$\rightarrow |\downarrow\uparrow\rangle \otimes |\uparrow\downarrow\rangle, \quad (1.13)$$

$$\rightarrow |\uparrow\uparrow\rangle \otimes |\downarrow\downarrow\rangle \rightarrow |\uparrow\downarrow\rangle \otimes |\downarrow\uparrow\rangle, \quad (1.14)$$

$$\rightarrow |\downarrow\uparrow\rangle \otimes |\uparrow\downarrow\rangle. \quad (1.15)$$

Furthermore, let V_1 denote matrix element of the interaction between excitons with the same polarisations and V_2 with the opposite. Renucci *et al.* [83] have shown that $V_1 > 0$, $V_2 < 0$ and $|V_2| \ll |V_1|$ for negative or zero detuned cavities, which means that polaritons with the same spin repel and polaritons with opposite spin attract, although this interaction is much weaker.

The presence of a small $V_2 \neq 0$ and a polariton spin flip mechanism lead to a feedback mechanism between the two polarisations. If the polariton lifetime was infinite, after the initial seeding pulse, independently of its polarisation, the polariton system would return to equal populations of σ^+ and σ^- polaritons. However, the limited polariton lifetime does not allow such equilibrium to be achieved – polarisation behaviour becomes more complex.

Gippius *et al.* in their work [85] considered a polariton system which is pumped at $k = 0$, which normally exhibits bistable behaviour, with additional degree of interest - polarisation. The aforementioned considerations

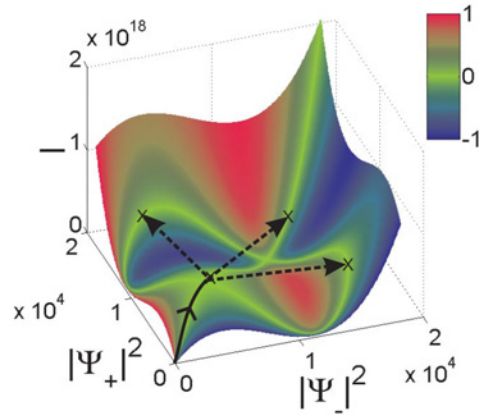


Figure 1.14. Dependence of the signal polarisation and intensity on the pump power I and polarisation (colour). $|\Psi_-|^2$ and $|\Psi_+|^2$ correspond to intensities of the σ^- and the σ^+ components of the internal polariton field. Green colour corresponds to linearly polarised pump, blue to σ^- and red to σ^+ . Crosses mark stable points for the signal corresponding to the same linearly polarized pump intensity. Arrows show three possible jumps in case if the pump intensity is slightly increased. Source: [85].

led them to conclude that the polariton system should exhibit polarisation multistability. This can be explained using figure 1.14, which was calculated for the case when $V_2 = -0.1V_1$.

The black solid shows evolution of the system as the pump power is increased starting from 0 whilst the pump polarisation is kept linear. When the pump reaches bistability threshold the system can jump into one of the three possible states: highly linearly polarised, right- and left-circularly polarised. The possible jumps are indicated by dashed black arrows, and the choice of the final state is random and is driven by fluctuations. It was also noted that the jump of the system to one of the circularly polarised final states results in a redshift of the cross-circular component because $V_2 < 0$. This in turn drives this component out of resonance with the pump leading to a stronger polarisation of the internal polariton field.

Similar multistable behaviour can be expected in the case of the OPO

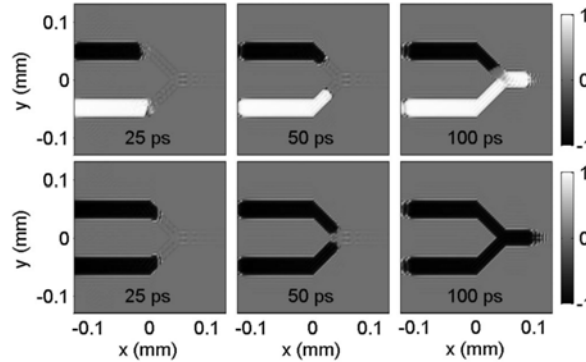


Figure 1.15. Logical gate based on polariton polarisation multistability. Colour scale shows degree of circular polarisation. Here CW pump is elliptical and biased towards σ^+ and maintains the system within bistability range at low density state. Then two writing beams σ^+ and σ^- trigger switching of the high density state in σ^+ and σ^- polarisations which spread along the Y-shaped cavity. Once the two states merge only σ^+ survives, since it has stronger pumping field. In case when both beams are σ^- the resulting polarisation on the end of the neuron is also σ^- . In this way it constitutes an OR logical gate. In calculations $V_2 = -0.5V_1$. Source: [86].

configuration of the excitation. If the pump bistability coincides with parametric instability, polarisation multistability can be observed in OPO signal emission.

Finally, the existence of polarisation multistability can lead to different interesting effects and applications, such as polariton neurons [86] (figure 1.15), spin switches [87] and the appearance of spin rings [88]. The latter is the subject of the experimental investigation presented in Chapter 2.

§ 1.6 Effects of interactions in polariton high density states

From the time of the first observation of polariton condensate there has been a growing interest in studying its fundamental properties. One of the key properties of a condensate is the healing length, a distance from a perturbation over which a locally perturbed condensate wavefunction returns to the homogeneous solution. It reflects the characteristic length of interactions inside the condensate. In the case of polariton condensate it can be derived from the following [61]:

$$E_{shift} \approx \frac{\hbar^2}{2m^*(k_{pump})\xi^2} \quad (1.16)$$

where E_{shift} is energy blueshift of the condensate due to polariton-polariton interactions, m^* is effective mass of polaritons for a given pump k-vector, ξ is healing length. For typical condensates in GaAs-based microcavities the healing length was shown to be in the order of a few microns [89].

The existence of quantised vortices in superfluids was predicted by Onsager [90] and Feynman [91]. After the discovery of polariton condensation there has been a considerable effort in studying nucleation and dynamics of quantum vortices and half-vortices [8, 92, 89, 93, 94, 95]. Vortices in superfluids are formed by rotation of superfluids around their core. Vortices have quantized phase (an integer multiple of 2π) and are characterised by the vanishing of the superfluid population at their core. The study of vortices is of great importance as it allows the examination of interactions in

a Bose gas on distances of the order or less than the healing length, since the vortex size is given by the healing length and hence depends on interactions [89]. Half-vortices are formed when, in condensate consisting of two populations of σ^+ and σ^- polaritons, the superfluid is rotating only in one polarisation⁴.

Superfluidity is a state of matter where it flows without viscosity. It is closely related to BEC. Polariton systems can undergo a Berezinskii-Kosterlitz-Thouless transition towards superfluidity below the critical the temperature T_{BKT} . If the temperature of the system is higher than T_{BKT} , the superfluid will no longer exist. Once superfluid, a Bose gas has a peculiar shape of its dispersion. The dispersion relation was first introduced by Landau to describe superfluid helium-II [48]. This spectrum of excitations (figure 1.16) was confirmed by Bogoliubov's microscopic theory of BEC [98]. Interactions lead to linear Bogoliubov dispersion at low k-vectors for helium-II. As a result, if the condensate propagates against an inelastic obstacle with velocity less than the sound velocity of Bogoliubov excitations, scattering is suppressed.

Another type of topological defect that can be created in condensates are solitons, which are of high relevance to the current work. They can be created as a result of scattering of a moving superfluid on a defect. In a superfluid, fluctuations of particle energies less than the phonon energy for a given condensate are energetically unfavourable and motion is dissipationless. Therefore, if the speed of sound c_s is less than the velocity of the defect in the fluid, it is not superfluid any more: in this case, the condensate has velocity v and is flowing onto an obstacle, which is stationary in the labora-

⁴Half-vortices (or vortices in spinor condensates) can be also treated as magnetic monopoles [96, 97].

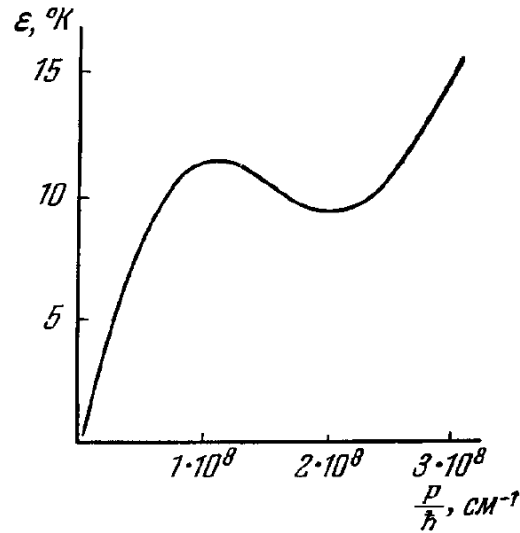


Figure 1.16. Excitation spectrum of liquid helium. Notably dispersion is linear for low wavenumbers, which is obtained for parabolic spectrum. Source: [48].

tory frame. The defect excites Bogoliubov modes whose energy is $\omega(k) = 0$. When a condensate starts to move its dispersion of excitation in the laboratory frame is tilted, with group velocities being $v_g^{l,r} = c_s \pm v$. In the subsonic regime only $k = 0$ modes can be excited, i.e. motion is dissipationless. In the supersonic regime there are regions where $\omega(k) = 0$, and some energy is dissipated in Bogoliubov modes. This is the so-called Cherenkov scattering [99].

Polariton dispersion can be approximated with parabola at low k -vectors and a linear spectrum can be obtained for the polariton condensate [100, 101] with a flat region near $k = 0$ in the dispersion due to their nonequilibrium character [102]. Although polariton condensates are not ideal superfluids, superfluidity can be observed for polaritons driven resonantly with a CW laser and propagating against an obstacle. Superfluidity of polaritons was demonstrated in the resonant excitation regime in the transmission configuration by Amo *et al.* [6]. In this configuration the created

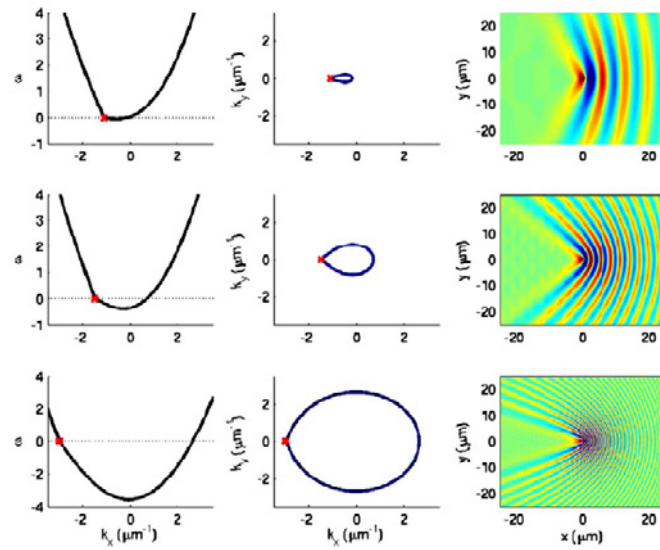


Figure 1.17. Dispersion of Bogoliubov modes (left column), k space describing the resonantly excited Bogoliubov modes (center column), and the spatial density profile (right column). The supersonic flows are $v = c_s \cdot 1.1, 1.5, 3$ in each row, respectively. Source: [99].

polariton density increases with increasing pump power. Once it reaches the threshold value, polaritons exhibit superfluid behaviour with no scattering around a defect. In addition authors managed to observe Cherenkov scattering regime, when the flow velocity exceeded the speed of sound.

§ 1.7 Polariton spatial solitons

§ 1.7.1 Oblique dark solitons

Cherenkov scattering at some conditions can create stable oblique traces which can be described as dark solitons. This approach was used by Ciuti *et. al.* in their theoretical work [103]. They considered hydrodynamic effects of a defect situated on the edge of a propagating polariton fluid. Depending on the polariton flow velocity they could observe Cherenkov-like scattering from the defect. By increasing flow velocity further they could observe nucleation of vortices and finally creation of solitons as is shown in figure 1.18. The created one-dimensional soliton is stationary in the laboratory frame while the polariton flow is moving against it. The size of a soliton here depends on the healing length (ξ). In addition the number of solitons created by the defect depends on the ratio between defect size and healing length. When the defect size is $d \approx 4\xi$ one pair of solitons is observed, if $d \approx 8\xi$ two pairs of solitons may appear. These dark solitons were observed by Amo *et. al.* [9]. They have observed all [103] types of solitons predicted theoretically: one pair and two pairs depending on the defect size. Justification for calling these traces solitons is based on the fundamental property of solitons to change the phase of the surrounding field by π , which was also observed. Similar oblique dark solitons have been also predicted to be seen in atomic condensates [104, 105].

Oblique half-solitons were also predicted [106]. Analogous with half-

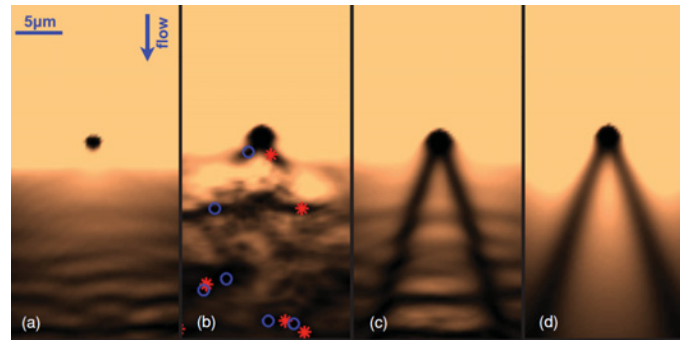


Figure 1.18. (a) Superfluid flow, $\omega/c_s \ll 0.43$ at the defect position. $\omega/c_s = 0.43$ is a critical value above which regime of unperturbed flow cannot survive; (b) Creation of dynamic vortex-antivortex pairs, $\omega/c_s = 0.76$. (c) $\omega/c_s = 0.93$, (d) $\omega/c_s = 1.02$ Cherenkov-like scattering and creation of solitons. The defect size is of the order of polariton healing length. Source: [103].

vortices, dark half-solitons only appear in either σ^+ or σ^- polarisation while the whole condensate has linear polarisation. Dark half-solitons were also predicted to behave as magnetic monopoles, which were recently experimentally demonstrated [107], where soliton trajectories were splitting under the influence of a magnetic field induced by the TE-TM splitting.

It is notable that dark solitons in polariton fluids are conservative - they exist within the polariton lifetime and are described by Nonlinear Schrödinger equations, which does not take into account the effect of gain and losses.

§ 1.7.2 Propagating wavepackets

Before discussing spatial solitons themselves it is worth mentioning work that has been done on wavepackets. Freixanet *et al.* in their work [108] used a single pulsed laser to resonantly excite polaritons at a fixed angle

but different cavity detunings. Experimental observations have shown that polaritons sustain their initial momentum on a scale of tens of picoseconds which depends on the detuning. The group velocity of this polariton bullet replicates the slope of the dispersion curve at a given cavity detuning and incidence angle.

In [109] the authors consider semiconductor microcavity system pumped resonantly with a CW laser resonant with the lower polariton branch. The pump power is set slightly above the OPO threshold, and the signal state is formed at $k = 0$. Then a pulsed probe beam is applied at higher momenta, $k_{probe} < k_{idler}$ (see figure 1.19). This probe triggers scattering processes, which induce a corresponding signal state with nonzero momentum $k_{s1} = 2k_{pump} - k_{probe}$. This pulsed signal moves on top of the CW condensate. In this way it is possible to probe the excitation spectrum of the condensate. However, for the probe spot size $\Delta r = 15 - 20 \mu\text{m}$ the momentum distribution is very small, and observed effects of dispersion are negligible. Almost no broadening of the wavepacket is observed during its propagation time – as seen in figure 1.20(a).

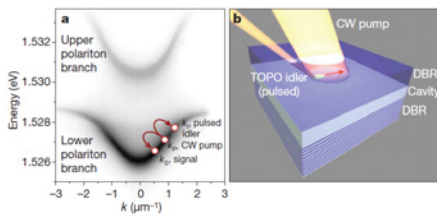


Figure 1.19. (a) - TOPO configuration of the experiment ([109]); (b) - experimental set-up. Source: [109].

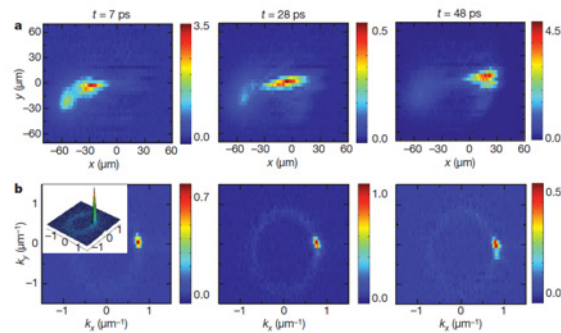


Figure 1.20. (a) - real space images of far field emission (condensate background subtracted) in time; and (b) corresponding momentum space measurements. Source: [109].

§ 1.7.3 Dissipative solitons

Although the term *soliton* was originally used to describe waves (wavepackets in solitude) that propagate in a medium and are stabilised by some non-linear process, it is now used in much broader contexts. Dissipative solitons generally describe the existence over extended periods of time of profiles of intensity, temperature, magnetic field, etc. in open systems. They may or may not be moving relative to the laboratory frame.

The existence of dissipative solitons critically depends on gain that compensates losses in addition to conditions needed for localisation or stabilisation, and is mainly determined by the parameters of the system not by the initial conditions. The gain and loss present in these systems lead to continuous energy redistribution and flow inside the soliton.

In polariton systems it is currently possible to maintain large areas where bistability or multistability can be observed. Their size can reach up to 100 μm , which is much larger than the typical interaction length of polaritons ($\approx 5\mu\text{m}$). This leads to the possibility of observing spatial hysteresis. It means that neighbouring areas in a system can exist in different states: high and low density states in the case of bistability. Which can lead to formation of patterns or solitons that are stabilised by nonlinear interactions.

These properties have been studied in great detail for optical and magneto-optical systems. For instance, temporal solitons in optical fibres were proposed to be used for long haul data transmission and compression [26]. Soliton collisions in laser systems can lead to creation of soliton complexes [29].

Additional insight into the kind of interactions observed in polaritons systems can be taken from atomic physics, where different soliton patterns and soliton trains were observed, once the size of the atomic condensate sufficiently exceeded the corresponding healing length [30, 25].

The formation of dissipative soliton patterns arising from stabilisation of interference-induced patterns has been studied in microcavity resonators in the weak-coupling regime [110, 111, 112]. These cavity solitons can arise from stabilisation of periodical patterns in dissipative resonators [113] or their formation can be triggered by an external probe while the system is in a bistable regime [110].

§ 1.7.4 Known solutions for dissipative polariton spatial solitons

It is also possible to create spatial polariton dissipative solitons in polariton systems with very short polariton life time, typically 5-10 ps. The formation and sustaining of solitons, as well as many other effects, requires continuous replenishing of the escaped polaritons. To do so, a scheme where the soliton propagates on top of a CW pump field background was proposed by Skryabin *et al.* [114]. The soliton existence and propagation conditions are dependent on the pump field energy, excitation angle and power.

One-dimensional bright solitons (localised in the transverse direction to propagation by a limiting potential) were predicted to exist [115] due to negative effective mass of polaritons with k-vector above the point of inflec-

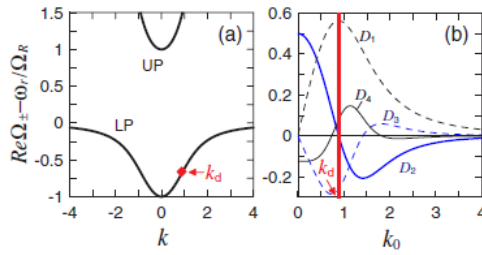


Figure 1.21. (a) Polariton dispersion: lower (LP) and upper (UP) branch in the strong-coupling regime. (b) Dispersion coefficients vs inclination of the holding beam k_0 . Source: [115].

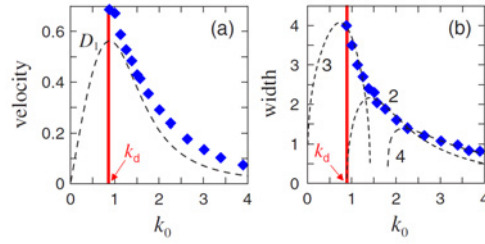


Figure 1.22. (a) Diamonds show numerically computed soliton velocity vs k_0 . Dashed line shows $D_1(k_0)$. (b) Diamonds show the soliton width vs k_0 . Dashed lines show the appropriately scaled $\sqrt[m]{D_m}$, where $m = 2, 3, 4$. Source: [115].

tion. To create such solitons, the pump has to be applied at k -vectors above the point of inflection with a slight blue-shift in energy relative to the unperturbed polariton dispersion. The pump power has to be chosen so that the system is within the bistability range of the pump only state.

In order to have a bright soliton, the pump field should be prepared in the lower, 'off' state in the bistability range. A small writing beam (or strong enough local density fluctuation) then locally 'switches on' the pump to the high density state. Since pump-only bistability coincided with parametric instability, such a switch results in stimulated polariton-polariton scattering to a wide range of k -vectors on the polariton dispersion. In the case of negative polariton effective mass at the pump k -vector, it was shown that such a scattering undergoes self-organisation, forming a soliton – a stable localised wavepacket, stabilised by repulsive polariton-polariton interactions. These are dissipative solitons.

In figure 1.21(b) the decomposition of the dispersion of a moving polariton wavepacket into spectral components using Fourier transformation is shown in the case of slowly changing amplitudes, $D_i \sim \partial^i E(k)/\partial k^i$.

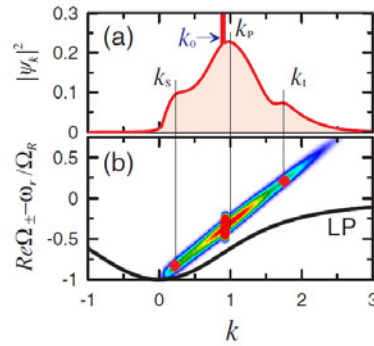


Figure 1.23. (a) Excitonic part of the soliton spectrum ($|\Psi_k|$) of the soliton. (b) The density plot is the 2D generalization of $|\Psi_k|$ from (a). The slope of this plot shows dependence of the soliton frequency on k . The full line is LP dispersion. Source: [115].

The k -vector of the pump field k_{pump} is also expected to influence the velocity and the size of a soliton. Figure 1.22 gives an insight about this, notably, that the soliton width depends on all dispersion orders.

It is important to emphasize that a soliton can only be created within the pump field, which intensity is kept within the bistability region. Moreover, the pump field should be kept in the lower, 'off' state. This condition is crucial for existence of a 'soliton solution' for the polariton system. Qualitatively, this is needed to allow polaritons forming a soliton to occupy a high density state.

The real space localisation of a soliton suggests its broad spectrum in energy-momentum space. Simulations from [115] suggest a linear soliton dispersion in contrast to the conventional polariton dispersion, see figure 1.23. Since the soliton is a non-diffracting wavepacket, its dispersion must be linear in a wide range of k -vectors, contrary to a single-particle polariton dispersion.

All these considerations apply to the processes in the soliton propagation direction. However in the transverse direction the polariton mass is

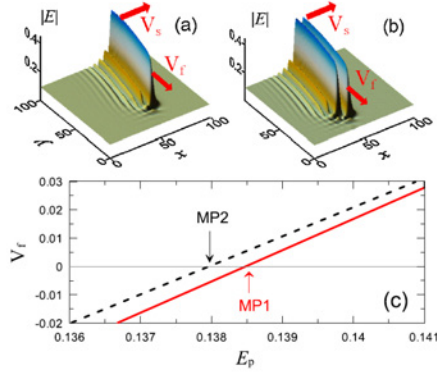


Figure 1.24. Moving fronts connecting 1D singlehump (a) and double-hump (b) CPSs and HS background. (c) Velocities V_f of the single-hump (solid line) and doublehump (dashed line) fronts. $V_f = 0$ at the Maxwell points MP1 and MP2. Source: [114].

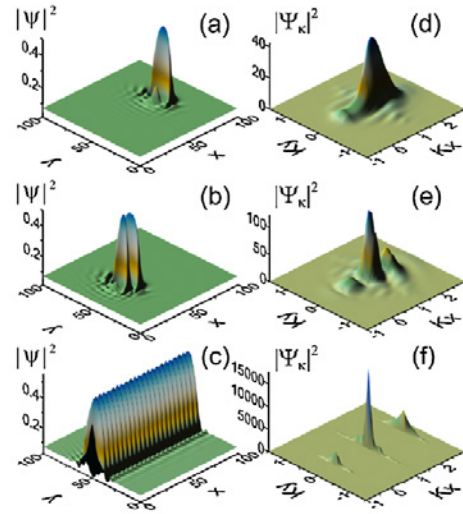


Figure 1.25. Profiles of the excitonic components of the stable bright polariton solitons in the coordinate (a)(c) and momentum (d)(f) space. Panels (a),(b),(d),(e) correspond to the single- and double-hump 2D solitons. Panels (c),(f) correspond to the parametric soliton localized only along y coordinate. Source: [114].

positive. The above mentioned work [115] does not account for the fact that in reality it is hard to create 1D limiting repulsive potentials and therefore there should be a mechanism to sustain a soliton in the transverse direction. It appeared that it is possible to create a stable localised polariton wavepacket in two-dimensional space. In [114] it is argued that the pump field intensity influences the velocity of the wavepacket's side fronts. This velocity decreases with increasing pump intensity and passes through zero at the so-called Maxwell point, which lies inside the bistability region, as is shown in figure 1.24. At the same time, the pump profile can act as an effective barrier for soliton spreading in the transverse direction. Figure 1.26 shows the pump profile dip (black curve) along with soliton and idler profiles, which appears due to local exhaustion of the pump field due to efficient scattering into soliton harmonics.

Two types of stable soliton solutions were found numerically: single-hump and double-hump solitons (figure 1.25). From the experimental point of view, the type of actually excited soliton depends on fluctuation and kick pulse power - the higher it is, the more likely double-hump soliton is excited.

An additional predicted feature of polariton solitons in semiconductor microcavities is the possibility of amplitude modulation which arises from saturation of exciton-photon coupling [116]. A high-enough density of the lower and the upper polariton dispersion branches leads to a blueshift of the LPB and a redshift of the UPB, which in turn results in a new frequency interval. Its frequency is estimated to be high enough to support a stable subwavelength modulation of the excitonic component in the soliton. These oscillations can develop from any perturbation once the excitonic and photonic components exceed certain threshold values.

The other possible type of polariton solitons are dissipative dark solitons where a dip in the density propagates in the high density state driven by the resonant pump at $k \approx 0$ where the polariton effective mass is positive. In [117] the authors consider this type of soliton. They show these are only stable solutions given the repulsive nature of polaritons (see fig. 1.27). Numerical solutions for solitons here were obtained by introducing a small bifurcation to the previously homogeneous system and observing the system's response to it. It has to be noted that the dark type of solitons can exist only in much narrower range of pump powers compared to bright solitons.

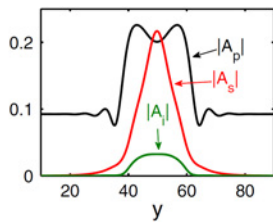


Figure 1.26. y profiles of the pump, signal, and idler components of the photonic component of the parametric CPS shown in figure 1.25(c). Source: [114].

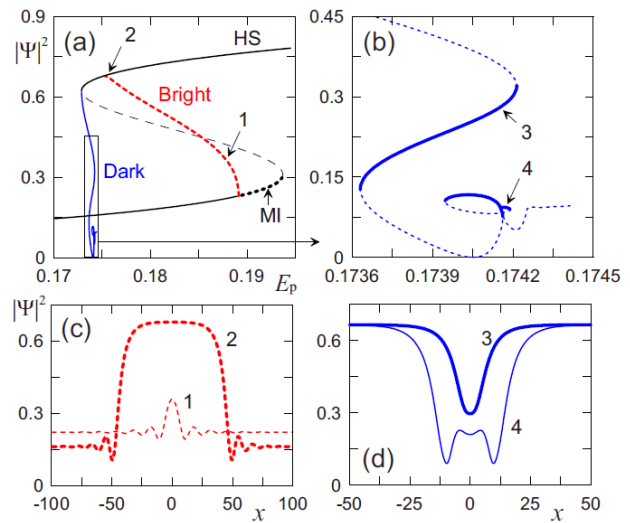


Figure 1.27. (a) Amplitude of the homogeneous state (black line), red line for bright solitons and blue line for dark solitons. (b) is a close-up of the rectangular area from (a) showing bifurcations of dark solitons. (c), (d) Exciton density distribution across bright (c) and dark (d) solitons for the points marked by 1, 2, 3, and 4. Solid and dashed lines in (a)(d) mark stable and unstable solutions, respectively. Source: [117].

§ 1.7.5 Other suggestions

There was an attempt [118] to describe and observe polariton solitons using a phenomenological model developed for the understanding of dark (bright) domain formation in weakly coupled semiconductor microcavities [33] called resonator solitons. However, there was no further experimental evidence published that would confirm validity of the claims.

Previously there was a suggestion to use slightly off resonant laser pulses to excite polariton solitons [119, 120] in bulk semiconductors. In this case the authors considered interactions between upper and lower polariton branches, that would lead to simultaneous propagation of wavepackets of

polaritons in both branches. Calculations have shown that it should be feasible to perform experiments to prove this in CuCl and CdS crystals, however, no experiments are known to be reported that prove these theoretical suggestions.

§ 1.8 Experimental techniques

In this section basic experimental techniques will be discussed and a core experimental setup, used in most of the measurements will be described, setting a consistent background for the presentation of the results in the following chapters.

Micron-sized effects and features are studied in the majority of experiments on semiconductor microcavities. Furthermore, in most of the cases useful emission from the microcavity sample lies in the invisible part of the optical spectrum. Particularly for GaAs-based microcavities, this emission can be typically in the range from 800 nm to 900 nm.

Strong coupling of polaritons in GaAs-based devices is only observed at cryogenic temperatures: below 15 or 20 K. Therefore all experiments are done using cryostats, where samples are mounted and maintained at the needed temperature. Usage of cryostats poses several limitation on the setup. Firstly, any cryostat is connected either to a helium return line, or to a helium dewar and a pumping station, which means that the sample can be subject to relatively high mechanical vibration depending on the actual

cryostat, mounts and vibration damping used. Vibration from the pump transferred via vacuum tubes can be significantly reduced by using a heavy barrel attached to the middle of the vacuum line. It is also not possible to use advanced vibration damping for the optical table since it is connected to the pump and sometimes liquid helium dewar.

Secondly, depending on the model, all cryostats have limited numerical apertures accessible for optical detection or excitation, and due to the presence of cryostat windows, it is usually not possible to use very small focal distance objectives. Altogether, usage of cryostats limits the possible imaging resolution to 2 μm in the best case, being 5 μm with a regular lens.

§ 1.8.1 Near-field and far-field imaging

In near- and far-field imaging experiments a 2D CCD array is used to record the emission. The setup is designed to provide the highest possible resolution, given that a single pixel size on CCD chip is 13 μm , and it usually consists of a collection lens or objective, an imaging lens on the CCD and a magnifying telescope – to adjust the image size to overcome the CCD resolution limit. This is near-field, or real-space, imaging. Its schematic setup is depicted in figure 1.28.

Imaging of dispersion is possible via far-field, or k-space or momentum-energy space, imaging. In this case an image of the Fourier plane of the collecting lens is projected onto the spectrometer input slits. With the diffraction gratings set to the relevant wavelength, it is possible to record disper-

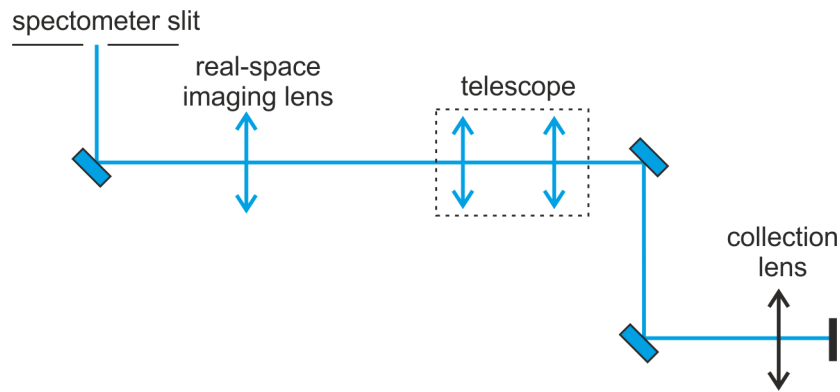


Figure 1.28. Real-space imaging setup.

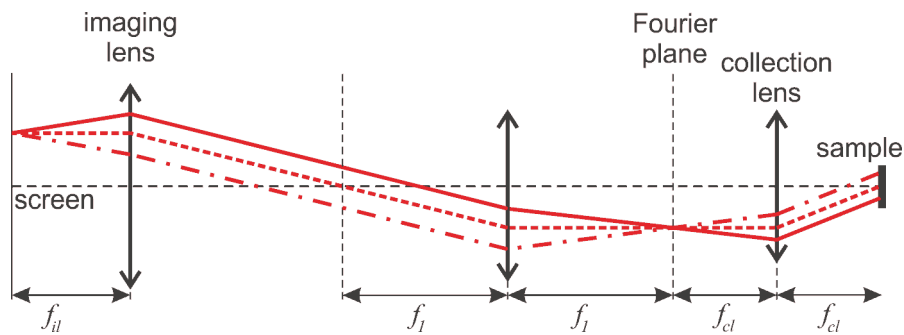


Figure 1.29. k-space imaging setup. All light from the sample that is emitted at the same angle but from different position on the sample is focused to one spot in Fourier plane by the collecting lens. Then this Fourier plane is imaged on the screen.

sion curves: emission intensity as a function of wavelength and angle. This setup is shown in figure 1.29.

The resulting setup for detection is shown in figure 1.30. It consists of real-space and k-space imaging paths and an imaging spectrometer. Its CCD can be used for spectrography or, when diffraction gratings are set to zero order and input slits open, it can be used to take images of real-space.

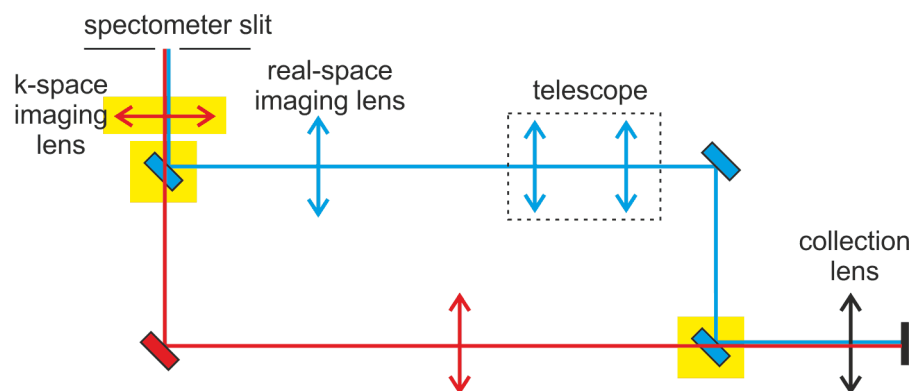


Figure 1.30. Experimental setup for imaging combining real-space imaging path (blue) and k-space imaging path (red). Elements in yellow rectangles are mounted on flip mounts that allow quick switching between imaging.

§ 1.8.2 Streak-camera

A streak-camera allows the recording of images with time resolution of up to 2 ps. The streak-camera's principle of operation can be seen in figure 1.31. Light to be measured is projected onto the slit and focused through the lens on the photocathode of the streak tube, where photons are converted into a number of electrons proportional to the incident light intensity. These electrons are accelerated and then pass through the sweep electrodes. As they pass the sweep electrodes, the applied sweep voltage is changed with time, directing electrons that arrive at different times to different angles. After they hit the MCP plate for additional multiplication, they are bombarded against a phosphor plate where they are converted back to light. This phosphor image is recorded with the CCD.

A streak-camera records a one dimensional real-space image with its evolution in time. However, it is possible to acquire two-dimensional real-space images by scanning vertically with a real-space imaging lens. Within a small range of lens displacement, it is possible to obtain images without

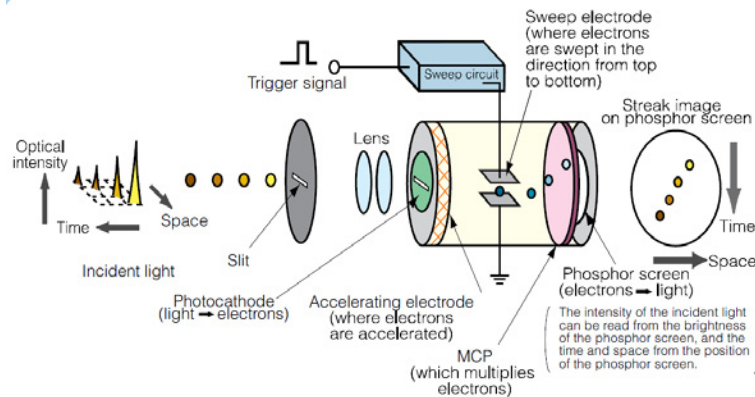


Figure 1.31. Streak-camera principle of operation. Source: Hamamatsu.

any significant aberrations due to lens displacement. Importantly larger focal distances favour such a technique, allowing reconstruction of the evolution of two-dimensional pictures in time.

§ 1.8.3 Core experimental setup

All experiments that study the temporal evolution of polariton systems require the use of pulsed excitation. The typical polariton lifetime of 5 to 10 picoseconds sets requirements to the duration of a pulsed excitation, which should be less than the polariton lifetime. For this purpose a femtosecond laser is used, which is sent through a pulse-shaper with resultant output pulse width of the order of 1-3 ps. The pulse-shaper schematic is shown in figure 1.32.

The core experimental setup is shown in figure 1.33. It combines pulsed and continuous wave (CW) excitations and real-space and k-space imaging paths. Notably, all experiments described in this work, apart from

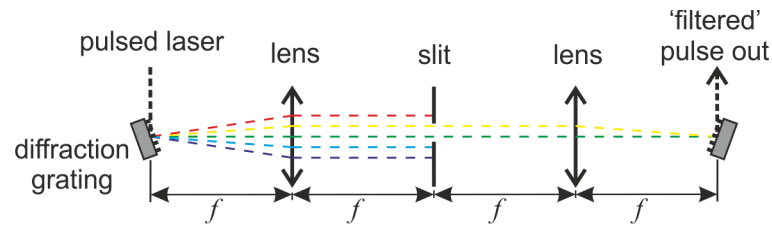


Figure 1.32. Pulse shaper. Spectrally dispersed emission from the first diffraction maximum of the incident light onto diffraction grating is focused into a collimated beam. By passing it through the mechanical slit it is possible to filter only required range wavelengths from the pulse. The accuracy of $\approx 5\mu\text{eV}$ of the method is mostly limited by the quality of optics used.

the spin-ring experiment, are done in the 'reflection' configuration, where excitation of the sample is done on the same side as detection. This is not the most convenient configuration from the point of view of an experiment, but the configuration choice is limited by the availability of good quality samples suitable for work in transmission, which are scarce. Emission of QWs in GaAs samples is around 809 nm, which is above the band gap of the GaAs substrate. Hence transmission is not possible.

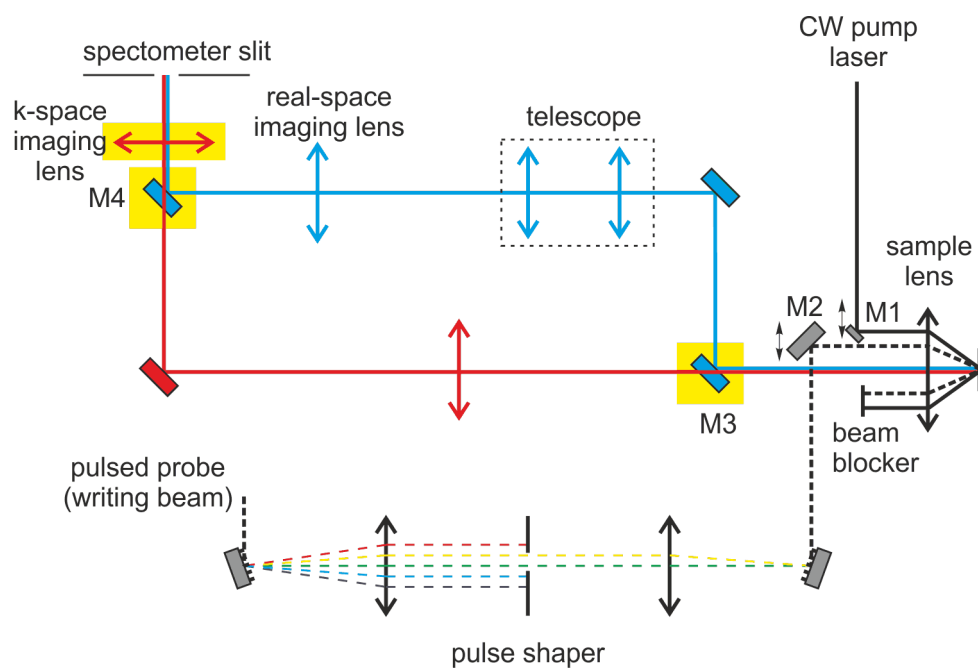


Figure 1.33. The detection path is as described in figure 1.30. Excitation beams are shown in black. Mirrors M1 and M2 are fixed on translational stages to allow for different excitation angles. Reflected beams of the CW and the pulsed laser are blocked by a beam blocker, only emission in the range from $k = 0$ to k_{min} (pump or probe k -vector, whichever is smaller) is detected. Collimation optics for CW and pulsed beams are omitted on the scheme.

Chapter 2

Spin rings

In this chapter, work on the investigation of multistability of a polariton system in the CW regime is presented. As a consequence of the exhibited multistability and Gaussian excitation, the formation of spatial ring patterns of high degree of circular polarisation (DCP) are reported. These results along with theoretical modelling were published in Physical Review Letters [121].

Polaritons with parallel spins repel, polaritons with opposite spins attract. Such interactions provide blueshifts and redshifts, respectively, of the energies of coherent polariton modes. This asymmetry results in the polarisation bistability and multistability described earlier in section 1.5 and in [85]. Polariton polarisation bistability has also been predicted to lead to the formation of spatial spin rings of high degree of circular polarisation [88]. These nonlinear spin properties and spatial patterns may lead to novel optical spin-based devices such as fast optical modulators, spin switches [87, 88], and polariton logic elements (polariton neurons) [86] operating at high picosecond speeds and very low pump powers. Polarisation multista-

bility has been studied for a vapor of atoms in a cavity [122, 123]. It has been also investigated in a number of solid state nonlinear systems including anisotropic crystals, magnetic cavities, and VCSELs [85]. However, in the latter structures pump powers a few orders of magnitude stronger than in the polariton system are required to observe nonlinearities, favouring microcavity polaritons for the development of nonlinear optical devices.

§ 2.1 Observation of polarisation multistability

The sample studied is a $3\lambda/2$ GaAs microcavity grown by metal-organic chemical-vapor disposition (MOCVD) with Rabi splitting of ≈ 6 meV. The data are collected with the quantum well exciton and the optical mode on resonance at $k = 0$. Polarisation multistability was studied in the experiment schematically shown in figure 2.1 in a transmission configuration at normal incidence ($k_{pump} = 0$). The sample was maintained at the temperature of 5 K. The detuning between the photon and exciton modes is close to zero. The energy of the pump laser is tuned ≈ 0.7 meV above the bottom of the lower polariton branch (located at 854.8 nm) and ≈ 2 meV below the exciton level.

As discussed in section 1.5, in such a configuration the polariton system exhibits bistable behaviour of transmission of intensity with respect

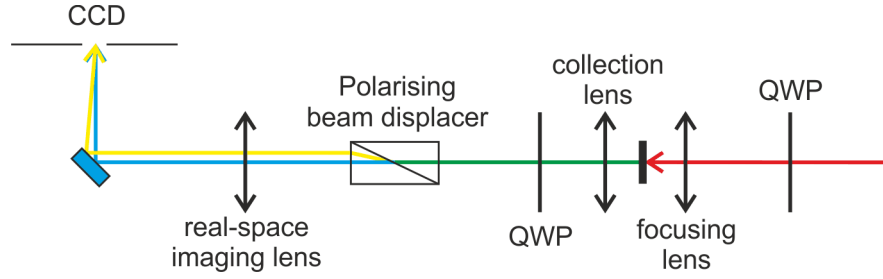


Figure 2.1. Excitation path is marked in red. The pump beam, linearly polarised, is sent through a quarter wave plate (QWP) mounted on a rotational stage in order to change pump polarisation ellipticity. Emission from the sample is collected by the lens, then sent through a QWP to convert σ^+ and σ^- polarisation components to linearly cross-polarised. Then polarising beam displacer is used to separate the components in space, which allows simultaneous detection of both components on a CCD.

to the external pump power. To characterise polarisation multistability σ^+ and σ^- intensity of the transmitted light (as described in figure 2.1) was detected, from purposely selected small regions (approximately $2 \mu\text{m} \times 2 \mu\text{m}$) in the centre of the pump spot, where the pump intensity is nearly constant, while changing the pump power and its degree of circular polarisation (DCP). The DCP of the pump (ρ_p) is defined as follows, in the same way as in (1.7):

$$\rho_p = \frac{I_p(\sigma^+) - I_p(\sigma^-)}{I_p(\sigma^+) + I_p(\sigma^-)}, \quad (2.1)$$

where $I_p(\sigma_{\pm})$ is the intensity of the respective pump component. The summary of the characterisation is presented in figure 2.2. Figures 2.2(a) - 2.2(d) show the intensities ($I_i(\sigma_{\pm})$) of σ^+ (triangles) and σ^- (lines) polarised components of the transmitted beam versus pump power for various pump DCPs. For $\rho_p = 1$ a clear hysteresis loop for σ^+ component is observed in accordance with bistable behaviour [80, 78]. When the pump DCP is reduced from $\rho_p = 1$ to ≈ 0 the bistability threshold power and the transmitted intensity at the threshold for the σ^+ component decrease by a factor of 1.5 and 3, respectively.

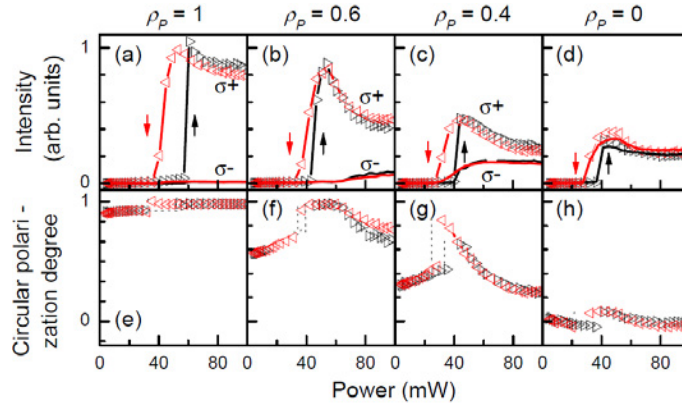


Figure 2.2. (a) - (d) Normal incidence transmitted intensity versus external pump power for ρ_p 1, 0.6, 0.4, and 0. Triangles (blue circles) correspond to the intensity of the component. Arrows show the direction in which the pump intensity is varied. (e) - (h) Corresponding DCP of transmission versus pump power. Reference: [121].

The behavior of the minority σ^- component versus pump power is different. $I_t(\sigma^-)$ is zero for σ^+ circularly polarised excitation (i.e., $\rho_p = 1$), but appears for smaller DCP of the laser until it approaches the same intensity as the σ^+ component for a nearly linearly polarised pump (figure 2.2(d)). In the latter case, as expected both $I_t(\sigma^-)$ and $I_t(\sigma^+)$ show nearly the same threshold, intensity, and hysteresis loop width. For elliptically polarised pumping at $\rho_p = 0.6$ and 0.4 , the σ^- component emerges, respectively, at powers 1.5 times larger or nearly equal to the threshold of the σ^+ component. Surprisingly, $I_t(\sigma^-)$ exhibits a smooth intensity increase at threshold instead of a step intensity jump and shows only a weak ($\rho_p = 0.4$) or no ($\rho_p = 0.6$) hysteresis behaviour.

The corresponding pump power dependence of the DCP of the transmitted light ρ_t , defined in a similar way to 2.1, is shown in figures 2.2(e) 2.2(h). At very low pump powers in the linear regime the DCP of the pump defines ρ_t , which then increases slightly by 10% with increasing pump power. When the threshold power is reached, ρ_t jumps to nearly one for $\rho_p = 0.6$

and 0.4. For $\rho_p = 0$ only a slight change to 0.1 at threshold is observed. With a further increase of pump power, ρ_t decreases again and eventually approaches the pump DCP ρ_p at very high powers. The hysteresis behavior of ρ_t follows that of the σ^+ component of the transmitted intensity, demonstrating polarization bistability.

The fact that the $I_t(\sigma^+)$ dependence has 1.5 times lower threshold than $I_t(\sigma^-)$ at $\rho_p = 0.6$ indicates a difference between the strengths of $\sigma^+\sigma^+$ and $\sigma^-\sigma^-$ polariton-polariton interactions [83, 85]. The sign and the strength of these interactions is strongly influenced by the biexciton resonance [124]. In particular, for pump energies E_p below the biexciton level $2E_p < 2E_X - E_b$ (E_x and $E_b \approx 1$ meV are the exciton energy and the biexciton binding energy, respectively) an attraction (repulsion) between cross- (co-) circularly polarised polaritons is expected [124].

For weak $\sigma^+\sigma^-$ attractive interactions the bistability threshold of $I_t(\sigma^+)$ should be at least 4 and 2.3 times less than that for $I_t(\sigma^-)$ at $\rho_p = 0.6$ and 0.4, respectively [85], according to the ratio of the cross-circularly polarised pump components $I_p(\sigma^+)/I_p(\sigma^-)$. The bistability threshold is expected to be at least a factor of 2 larger for linearly ($\rho_p = 0$) than for circularly ($\rho_p = 1$) polarised pumping. However, we observe in figure 2.2 that $I_t(\sigma^+)$ thresholds at $\rho_p = 0.6$ and $\rho_p = 0.4$ at factors of 1.5 and 1 below $I_t(\sigma^-)$, respectively, and the ratio of the threshold for $\rho_p = 0$ to $\rho_p = 1$ is ≈ 0.7 . This indicates the strong role of a repulsive blue shift interaction, which shifts the σ^- component towards resonance resulting in a rapid increase of the intensity of σ^- when the σ^+ mode is switched on.

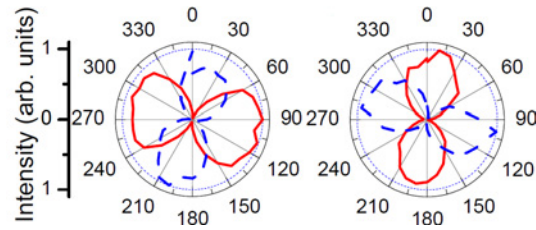


Figure 2.3. Left and right polar plots of normalised signal (dashed line) and the laser intensity (continuous line) for TE (left) and TM (right) polarised pump. Reference: [121].

§ 2.2 Measurement of cross-polarisation interactions

Attractive coupling between coherent σ^+ and σ^- modes is verified by studying the polarisation of the stimulated emission under resonant excitation into the LP branch at k vectors $k_{pump} \approx 1.4 \mu\text{m}^{-1}$ - in the OPO configuration. Polar intensity diagrams of the signal (dashed line) and the pump (solid line) are shown in figure 2.3 for TE and TM polarised pumps. The orientation of the linearly polarised stimulated emission at the signal state at $k = 0$ is rotated by 90 deg with respect to the excitation [125]. The 90 deg rotation has been observed for pump energies in the broad range 1.53 meV below the exciton level. This can only be accounted for by the attractive character of $\sigma^+\sigma^-$ interactions [125].

§ 2.3 Observation of spin rings

Spin rings arise due to the variation of the pump power across the excitation region, resulting in polarisation bistability thresholds being reached at higher total pump power near the edge of the spot than in the center.

Figures 2.4(a)-2.4(d) show spatial images of the transmitted beam at $\rho_p = 0.6$ for a series of pump powers. Note that below threshold (figure 2.4(a)) both σ^+ and σ^- polarised images are identical and strongly modulated by the disorder potential [126]. With increasing power the LP mode in the central area of the spot is blueshifted into resonance with the pump allowing a large intensity of the beam to be transmitted. As the power is increased more the region where the threshold is achieved expands. Note that although the spatial images above threshold (figures 2.4(c) and 2.4(d)) are still distorted by the disorder they have maxima away from the center of the spot at high power as expected for the case of bistability in a homogeneous sample [126]. This arises since the polariton blueshift above threshold is about ≈ 0.7 meV, which is larger than the amplitude of the disorder potential (≈ 0.1 meV), hence reducing the effect of polariton energy fluctuations.

Figures 2.4(e) 2.4(g) show the corresponding 2D spatial structure of the DCP. Below threshold (13 mW) the DCP is about 0.6, given by the pump DCP. Just above threshold (46 mW) the DCP jumps to unity in the middle of the pump spot forming a disk of high DCP (figure 2.4(f)). With increasing pump power the DCP in the center of the spot decreases down to 0.5, when the σ^- mode switches on (figure 2.2(b)). At the same time the DCP jumps from 0.6 to one in a region forming a ring around the spot center

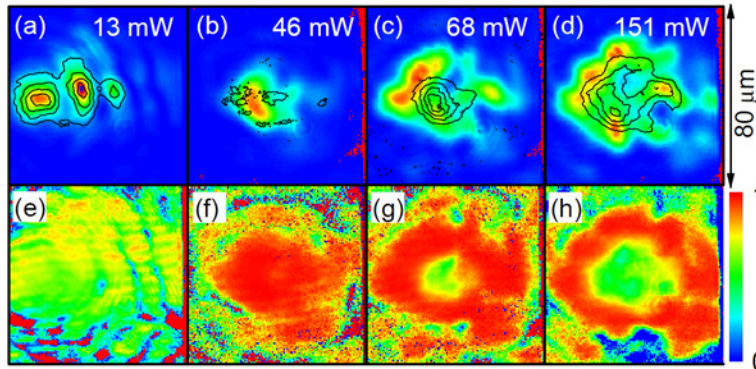


Figure 2.4. Real space images of intensity (a)(d) and corresponding DCP (e)(h) of the transmitted beam for elliptically ($\rho_p = 0.6$) polarised pump beam at different pumps powers. The images (contour lines) in (a)(d) show the intensity of the σ^+ (σ^-) component. Reference: [121].

(figure 2.4(g)), where the bistability threshold is achieved for the σ^+ but not the σ^- mode. This ring of high DCP (spin ring) expands with pump power, as the σ^+ component switches on at larger distances away from the center of the spot (figure 2.4(h)). Because the potential disorder is partially screened, the formation of the DCP rings (figures 2.4(f) and 2.4(g)) is observed as expected for a pure Gaussian spot [88]. This is consistent with the simulations of reference [88], predicting well-defined spin rings even in a disordered system.

In reference [88] it was shown that polariton diffusion affects the size of the σ^+ or σ^- polariton modes above threshold and hence the radii of the resultant spin rings, which are determined by the lower bistability threshold. When with increasing pump power the upper threshold is reached at the center of the excitation spot, for example, for the σ^+ mode, due to polariton diffusion the size of the mode extends to the region with an excitation density corresponding to the lower threshold. By contrast, when with decreasing pump power the lower threshold is achieved in the center of the pump spot, the size of the mode is determined only by that of the

Airy mode of the cavity. Experimentally we observe a difference of 30% in the sizes of the σ^+ modes at the lower and upper bistability thresholds for $\rho_p = 1$ confirming that diffusion affects the spatial distribution of the polariton modes.

§ 2.4 Discussion and conclusions

The experimental results presented in section 2.1 can be explained if one takes into account coupling between the coherently driven polariton modes and the incoherent excitonic reservoir, which provides the necessary blue shift. At energies below the exciton emission this reservoir consists of dark exciton states and weakly coupled localised excitons, which introduce additional damping of polaritons [127]. For the inhomogeneously broadened exciton level (FWHM ≈ 1.5 meV) in our sample the density of localised exciton states at 23 meV below E_X is estimated to be 3-4 orders of magnitude larger than that of polaritons [127].

In the work published [121] the model from [85] was further developed by S. Gavrilov taking into account transitions of the optically driven excitons into the incoherent reservoir in which the overall pseudospin is relaxed. The model considers the intracavity σ^\pm polarised electric field ε_\pm and coherent exciton polarisation P_\pm , coupled with the exciton population N in the incoherent reservoir:

$$i\dot{\varepsilon}_{\pm} = (\omega_c - i\gamma_c)\varepsilon_{\pm} + \alpha F_{\pm} + \beta P_{\pm}, \quad (2.2)$$

$$i\dot{P}_{\pm} = \left(\omega_x + V_1|P_{\pm}|^2 + V_2|P_{\mp}|^2 + (V_1 + V_2)N/2 - i(\gamma_x + V_r|P_{\mp}|^2) \right) P_{\pm} + A\varepsilon_{\pm}, \quad (2.3)$$

$$\dot{N} = -\gamma_r N + 4V_r|P_+|^2|P_-|^2. \quad (2.4)$$

where F is the pump electric field (taken as a plane wave), $\omega_{c,x}$ and $\gamma_{c,x}$ are eigenfrequencies and decay rates of the intracavity photon and exciton modes, α describes the response of the intracavity electric field to the external pump, A and β describe the exciton-photon coupling (Rabi splitting is equal to $2\sqrt{A\beta}$), $V_{1,2}$ are the matrix elements of the interaction between excitons with same (V_1) and opposite (V_2) circular polarisations ($V_1 > 0, V_2 < 0, |V_2| \ll |V_1|$).

The transitions from the coherently driven polariton modes into the reservoir are introduced phenomenologically as exciton nonradiative decay rates in combination with a rate equation for the reservoir occupation (2.4). $V_r|P_{\mp}|^2$ is the decay rate of the P_{\pm} component due to scattering between coherent excitons with opposite σ^{\pm} polarisations. It provides occupation of the reservoir at a rate $4V_r|P_+|^2|P_-|^2$ per unit time. V_r may microscopically arise from the scattering of two bright excitons with opposite spin to dark excitons [128]. It may also arise from transitions into the exciton reservoir via the virtual creation of biexcitons. Exciton decay into the reservoir due to $\sigma^+\sigma^-$ scattering is likely to dominate over $\sigma^+\sigma^+$ scattering, since in pump-probe experiments in MCs the absorption of a σ^- polarized probe is observed to be strongly enhanced by a factor of 3-4 for σ^+ polarised pumping [127]. γ_r is the exciton decay rate in the reservoir. γ_r and V_r correspond to effective mean values.

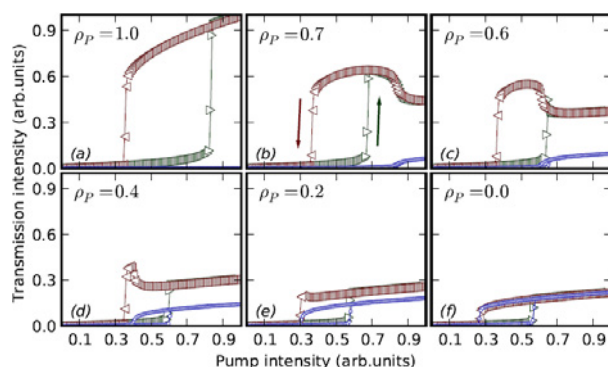


Figure 2.5. The calculated dependences of the MC transmission intensity vs pump intensity, for several DCP of the pump beam (ρ). The σ^+ (σ^-) component is shown by triangles (blue lines). \triangleright (\triangleleft) correspond to increasing (decreasing) pump power. The Rabi splitting, detuning between exciton and photon mode, and detuning between laser energy and LP branch are the same as in the experiment. Reference: [121].

The reservoir provides equal blueshifts for both polarised coherent spin states in addition to the attractive coupling between them which leads to the redshift. If the effect of the reservoir is not taken into account but still assuming repulsive interactions between cross-polarised polaritons, it was not possible to reproduce simultaneously the observed strong jumps of DCP by 40% with pump power (figure 2.2) and the ratio of bistability thresholds for the cases of circularly and linearly polarised pumps. The result of theoretical simulation is presented in figure 2.5 showing very good agreement with the experiment.

To summarise, polarisation bistability and spatial spin patterns as a result of spin anisotropy of polariton-polariton interactions were observed. The experimental results can be described by effective semiclassical equations of motion taking into account coherent macroscopically occupied modes and an incoherent reservoir.

At the time the experiments were performed, experimental results similar to those in figure 2.2 were published [129] although spin patterns

and the effect of the reservoir were unexplored. Spin rings have also been reported virtually simultaneously by another group [130].

Chapter 3

Bright polariton solitons

In this chapter the results of experiments designed relying on theoretical suggestions discussed in section 1.7 are presented. The main goal of this work was to observe polariton spatial solitons and to provide exhaustive characterisation of them. Most of the results discussed in this chapter were published in Nature Photonics [131].

Recently, matter wave solitons have been demonstrated in Bose condensed atomic gases, where the dispersive spreading of the localized wavepackets induced by the kinetic energy of positive mass atoms is balanced by the attractive interatomic interactions and trapping by the external potential [30, 25]. Interactions between the atoms used in condensation experiments are often repulsive. In order to create bright solitons in these cases, the effective atomic mass must be made negative, as demonstrated using optical lattices [132]. The same effect can be achieved for light in photonic crystals [133]. Strong exciton photon coupling in microcavities results in an unusual and advantageous lower polariton branch dispersion exhibiting regions of

either positive or negative effective mass [36, 134] depending on the values of transverse momentum [36, 134]. The transition from positive to negative mass is associated with the point of inflection of the energy-momentum diagram, which was discussed in Section 1.1. The negative mass of polaritons coupled with repulsive polariton-polariton interactions favour the formation of the bright solitons which we realise in the present work.

Discoveries made with microcavity polaritons include condensation [5, 68], vortices [8, 92], superfluidity [6] and follow a pathway similar to the one which led to the observation of coherent matter wave solitons [30, 25]. The observation of low threshold bistability, polarization multistability [85, 130, 121, 129] and parametric scattering [7] of polaritons have further prepared the necessary foundations for the realisation of half-light half-matter solitons. In contrast to atomic systems, polariton microcavities operate under non-equilibrium conditions. Atomic systems are typically described by conservative Hamiltonian models, such as NLS or Gross-Pitaevskii equations, while the polariton system is intrinsically non-Hamiltonian. In the photonic context, this system is often referred to as dissipative, which implies the importance of losses, but also implicitly assumes the presence of an external energy supply [135, 34]. Theoretically, conservative half-light half-matter solitons have been predicted by Safman and Skryabin [136], while dissipative bright spatial polariton solitons in microcavities have been numerically studied in [115, 114].

§ 3.1 Experimental setup

Due to the limited polariton lifetime, bright polariton solitons are dissipative in their nature, as was discussed in section 1.7. Therefore, to sustain soliton propagation over macroscopic distances, continuous replenishing of the escaped polaritons is required, which can be provided by applying an elongated CW pump beam, focused to a 70 μm (FWHM) Gaussian spot. At the same time the second pulsed excitation (writing beam - WB) is required to locally trigger soliton formation within the pump spot. This is schematically shown in figure 3.1. The pump and writing beams are incident along X direction.

The experimental setup was slightly modified comparing to that discussed in section 1.8.3. In order to access all possible excitation angles by both the pump and the writing beam simultaneously, including when $k_{\text{pump}} = k_{\text{wb}}$, a polarising beam splitter was used instead of a mirror (figure 3.2). In this case, however, the pump and the writing beam had to have orthogonal linear polarisations, which excluded a comprehensive polarisation study.

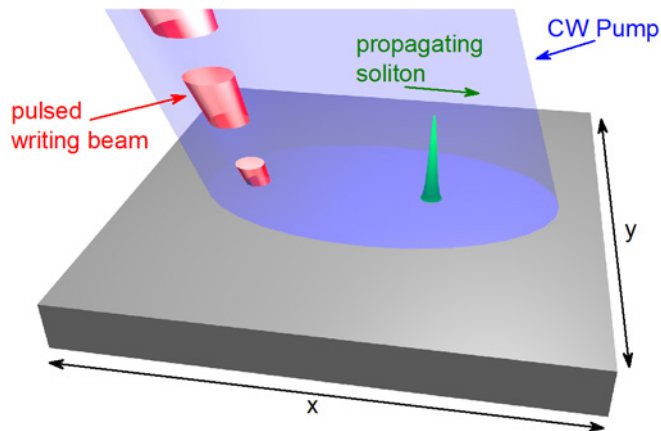


Figure 3.1. Schematic of soliton excitation in the microcavity structure. The CW pump with incident in-plane momentum parallel to the X direction is focused into a large spot. The pulsed writing beam, also incident along X, focused into a small spot triggers soliton formation. Reference: [131].

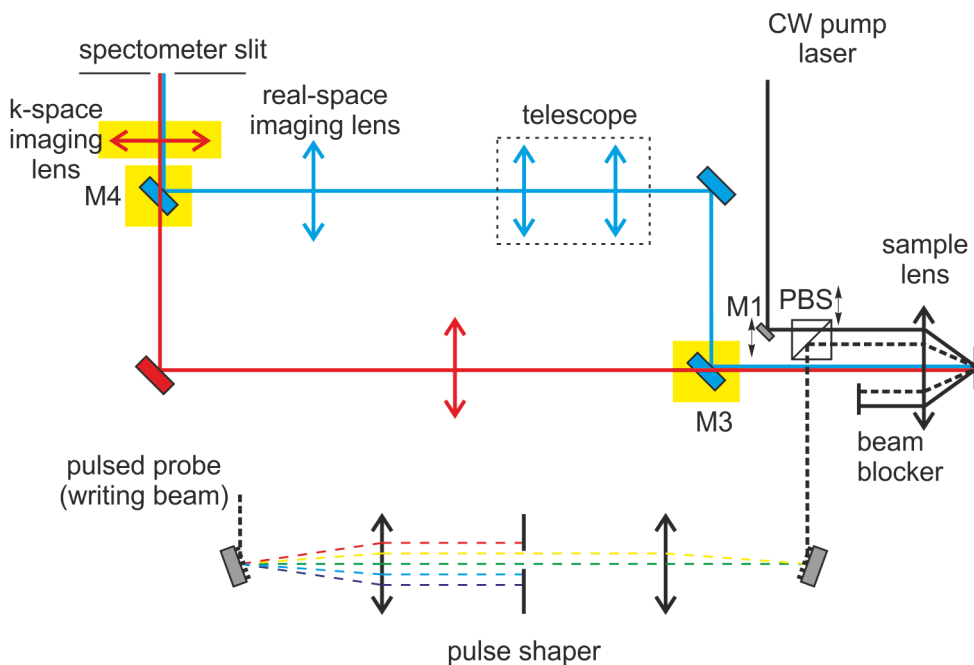


Figure 3.2. A modified experimental setup (polarisation optics not shown) compared to the setup shown in figure 1.33. M2 is replaced with a polarising beam splitter.

§ 3.2 Observation of bright polariton solitons

§ 3.2.1 Negative effective mass

The point of inflection of the polariton dispersion is found at the in-plane polariton momentum $k \approx 2 \mu\text{m}^{-1}$ (see figure 3.3(a)), which corresponds to a group velocity of noninteracting polaritons $\partial E/\partial k \approx 1.8 \mu\text{m}/\text{ps}$, where E is the polariton energy. The experiments were conducted with polaritons having momenta above the point of inflection, where the polariton mass is negative, $m^* \approx -11.2 \cdot 10^{-35} \text{ kg}$ ($-1.25 \cdot 10^{-4} m_0$), according to (1.3), at $k \approx 2.4 \mu\text{m}^{-1}$. The polariton soliton width for a given polariton density, N , can be estimated using the expression for the healing length of a quantum fluid $w = \hbar(\sqrt{2m^*gN})^{-1}$. This is obtained by equating the characteristic kinetic energy K of the dispersive spreading of the wavepacket with width w ($K = \hbar^2/(2m^*w^2)$) to the potential energy U of the polariton-polariton repulsion ($U = gN$, where $g \approx 10 \mu\text{eV} \cdot \mu\text{m}^2$ is the two-body interaction coefficient). For the typical soliton potential energies realised in our experiment $U \approx 0.3 \text{ meV}$ (corresponding to $N \approx 30 \mu\text{m}^{-2}$) from which we deduce $w \approx 2 \mu\text{m}$. The short free polariton lifetime ($\approx 5 \text{ ps}$) means that solitons emerging from this balance will traverse distances of $\approx 10 \mu\text{m}$, before they dissipate. In order to sustain these solitons for longer we need to provide a continuous supply of energy. To sustain these solitons, energy is pumped into the microcavity using a CW pump beam, (figure. 3.1).

§ 3.2.2 Bistability

The polariton density varies strongly across the bright soliton profile reaching its maximum at the center, while the pump beam profile tends to hold the density at a quasi-constant level across the much larger pump spot [115, 114]. Furthermore, due to localisation in real space the soliton profile in momentum space is broad. As a result, solitons can only be expected under conditions when the pump state is unstable with respect to spatially inhomogeneous perturbations at momenta different from that of the pump [115, 114]. If the microcavity is driven by a pump beam slightly blueshifted with respect to the unperturbed LP branch, the pump polariton field exhibits bistability as a function of the pump beam power and angle (Fig. 3.3(c)). The polariton bistability is usually accompanied by parametric (modulational) instability, which was extensively studied in microcavities [79, 137, 75]. This instability is a particular case of polaritonic four-wave mixing. Bright solitons are excited on top of the stable background of the lower branch of the bistability loop (Fig. 3.3(c)) and can be qualitatively interpreted as locally excited islands of the modulationally unstable upper branch solution [115, 114]. Broadband four-wave mixing of polaritons, expanding well beyond the momenta intervals with the parametric amplification, enables coherent scattering from the locally perturbed pump to the continuum of momenta forming the soliton (Fig. 3.3(a)). Simultaneously, the soliton formation requires the transverse momentum of the pump k_{pump} , i.e. the incident angle of the laser beam, to be such that the effective polariton mass is negative, ensuring self-focusing of the repulsively interacting polaritons [115]. This mechanism can lead to self-localisation only along the direction of the pump momentum (1D solitons) [115]. Simul-

taneous localisation in two dimensions involves more subtle physics and the corresponding solitons exist only in a narrow range of pump intensities [114].

Fig. 3.3(c) shows the bistable dependence of the polariton emission intensity collected from our device at nearly zero transverse momenta (direction normal to the cavity plane) as a function of the pump momentum (k_{pump}) at the fixed energy of the pump 1.5363 eV, which is ≈ 0.3 meV above the unperturbed LP branch at $k_{pump} \approx 2.37 \mu\text{m}^{-1}$. With increasing k_{pump} beyond the bistable interval the intracavity polariton field increases abruptly over the excitation pump spot. This transition is also accompanied by the strong parametric generation of polaritons into the state with $k \approx 0$ [72, 79]. According to the above discussion and the predictions of [115, 114], bright polariton solitons should exist within the bistability interval (figure 3.3(c)).

Bright polariton solitons are excited using a ps writing beam focused into a spot (figure 3.1) of diameter in the range $7 \mu\text{m}$ to $15 \mu\text{m}$, which is small compared to the diameter of the pump beam of $70 \mu\text{m}$. The writing beam is TE and the pump beam is TM polarized. The unperturbed polariton density (before the application of the writing beam) was in the state corresponding to the lower branch of the bistability loop (see arrow in figure 3.3(c)) with no indication of the parametric generation of polaritons with momenta different from the pump. The bistability domain was scanned by changing the pump momentum, where it was found that the optimal conditions for clear soliton observations exist close to the right boundary of the bistability interval shown in figure 3.3(c). The solitonic emission was collected along a $2 \mu\text{m}$ stripe of the streak camera image (see Methods) parallel to the direction of incidence of the pump. The light

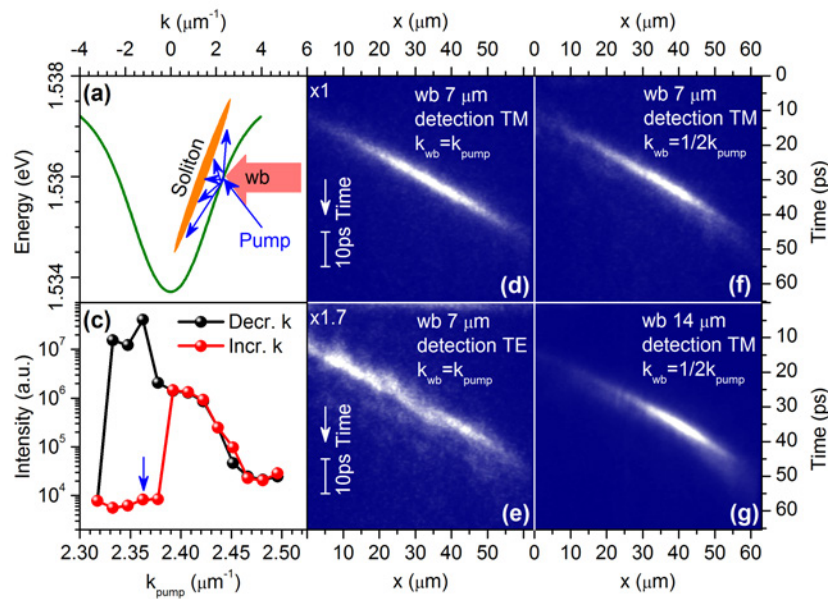


Figure 3.3. (a) Dispersion (energy-momentum) diagram of the lower branch polaritons and schematic representation of the soliton spectrum and the excitation scheme. (c) Bistable polariton density as a function of the pump momentum; The arrow indicates the state of the system created by the pump before incidence of the writing beam. (d-g) Streak camera measurements of the soliton trajectories along the X direction excited under different conditions. (d) and (e) show the components of the soliton in TE and TM polarizations, respectively. This soliton is excited with a $7 \mu\text{m}$ wide writing beam with in-plane momentum the same as that of the pump. (f) is the same as (d), but the writing beam has half the momentum of the pump. (g) is the same as (f), but the writing beam width is $14 \mu\text{m}$.

was collected inside the finite interval of angles corresponding to momenta $0 < k < k_{pump}$, thereby avoiding collection of the reflected pump beam, which otherwise leads to detector saturation. Figures 3.3(d) and (e) show spatio-temporal traces, obtained using a streak camera, of the intensities in TE and TM polarisations, for typical non-diffracting and non-decaying propagating wavepackets excited with the writing beam. Here the $7 \mu\text{m}$ writing beam arrives at position $X = -20 \mu\text{m}$ at time $t = 0$, and the transverse momentum is the same as that of the pump $k_{wb} = k_{pump}$.

§ 3.3 Characterisation of solitons

§ 3.3.1 Soliton velocity

The velocity of the soliton is independent of k_{wb} . The role of the writing beam is to create a local perturbation of the pump state, which in turn results in soliton formation due to scattering from the pump state (figure 3.1). It has been shown numerically for linearly polarised polariton solitons that their velocity is close to the group velocity of the polaritons at the pump momentum [115]. To test this prediction, the momentum of the writing beam was changed to half of the pump momentum, $k_{wb} = k_{pump}/2$ (Figs. 3.3(f,g)). Observed soliton velocity, shown in figure 3.3(f), is $\approx 1.68 \mu\text{m}/\text{ps}$, the same as that in figures 3.3(d) and (e), where $k_{wb} = k_{pump}$. The independence of

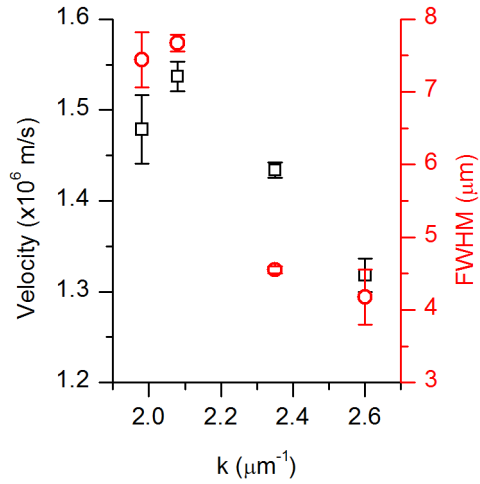


Figure 3.4. Soliton velocity (black) and size, FWHM, (red) as a function of k_{pump} .

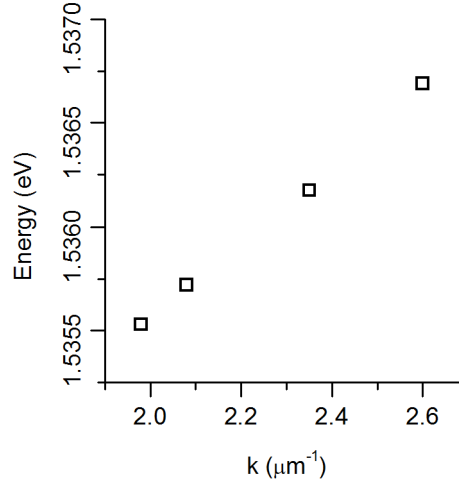


Figure 3.5. Pump energy used for different k_{pump} , that satisfied soliton formation conditions.

the polariton soliton velocity on k_{wb} is in sharp contrast to that expected for conservative solitons, where the soliton velocity is solely determined by the momentum of the writing beam [27].

Furthermore, to demonstrate the role of k_{pump} , the soliton velocity was measured as a function of k_{pump} . In this case the pump energy was also adjusted to satisfy conditions needed for soliton formation for every pump k-vector (see figure 3.5). The results, shown in figure 3.4, highly correlate with theoretical predictions [115], also shown in figure 1.22. The gradual decrease in the soliton velocity is due to diminishing of the first order derivative of the LPB above the point of inflection, which determines the soliton velocity.

§ 3.3.2 Soliton size

The size of the soliton is determined by the pump and cavity parameters and is independent of the size of the writing beam, as is true for other types of dissipative solitons [135, 34]. The size of the excited wavepacket (w) in the soliton regime is expected to be fixed by the potential energy U of the solitons, where U is of the order of the pump energy detuning with respect to the energy of the unperturbed lower branch polaritons ($w \sim 1/\sqrt{U}$ as discussed earlier). This is illustrated in figures 3.6(a-f), which show the profiles of polariton wavepackets along their propagation direction (X) at different times and positions for writing beam sizes of $\approx 7 \mu\text{m}$ (figures 3.6(a-c)) and $\approx 15 \mu\text{m}$ (figures 3.6(d-f)). In the initial stage of the soliton excitation, these writing beams produce polariton wavepackets of very different widths (see figures 3.6(a) and (d)), which then quickly evolve into solitons of the same size $\approx 5 \mu\text{m}$ as shown in figures 3.6(b) and (e), as expected for soliton formation.

In addition, according to the theoretical prediction [115] (see figure 1.22), the soliton size is expected to depend on the pump k -vector. This was experimentally confirmed, as shown in figure 3.4. The soliton size is decreasing when the pump k -vector is increased. This is a consequence of the broader spectrum ($0 < k < 2k_{pump}$, see section 3.3.4) in the case when k_{pump} is larger.

Non-spreading and non-decaying features of the soliton wave packets were observed. Figures 3.6(g) and (h) show the dependences of the intensity and width of the excited wavepackets, respectively, versus their position as a function of the writing beam power, P_{wb} . Within the range of P_{wb} from 1.6 mW to 2.3 mW, the soliton intensity and width are nearly constant. Fur-

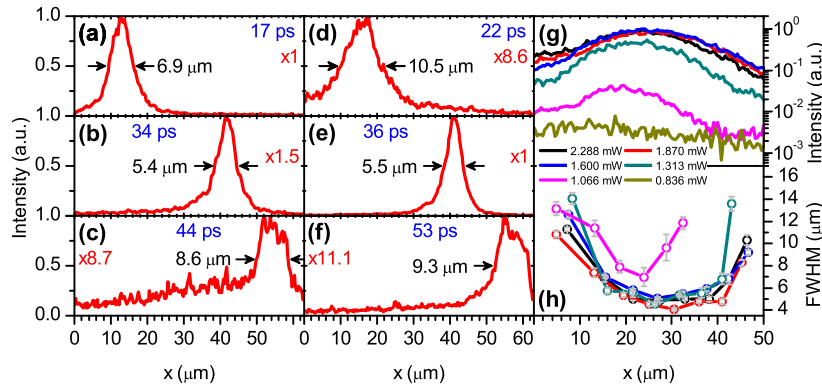


Figure 3.6. (a)-(c) Experimentally measured spatial intensity profiles of a soliton created by the 7 μm writing beam at different times, showing excitation and decay of the soliton; (d)-(f) Intensity profiles of a soliton created by the 15 μm writing beam; (g,h) Dynamics of the peak intensity and width of the wavepackets excited by the 7 μm writing beams with different powers as they propagate across the cavity. The writing powers where the above parameters remain quasi-constant in the interval of 20 to 40 μm correspond to the formation of solitons.

Furthermore, the width versus position dependence (figure 3.6(h)) exhibits a plateau in the interval from ≈ 20 to ≈ 40 μm . These are signatures of polariton soliton formation as well, which were also reproduced with theoretical modelling [131]. At the edge of the pump spot, the pump intensity is insufficient to maintain the system within the bistability region and thus to sustain solitons. This is the main factor determining the practical extent of the soliton trajectory, and leads to spreading and dissipation of the excited wavepackets at times greater than 40-45 ps when the edge of the pump spot is approached, as shown in figures 3.3(d-g) and figures 3.6(c),(f).

§ 3.3.3 Soliton intensity

The intensity of the writing beam must be high enough to enable soliton switching. (figure 3.6(h)). As one reduces the pump intensity below the

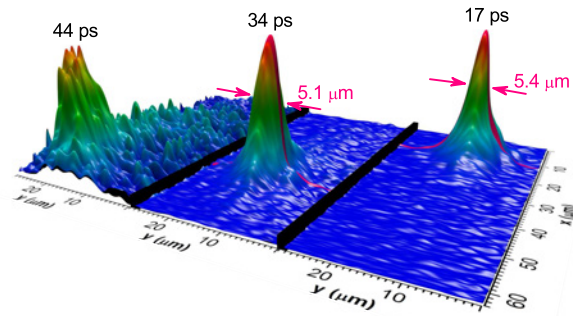


Figure 3.7. Two dimensional streak camera measurements of a soliton traveling across the microcavity plane. Experimental conditions are the same as in Figs. 3.6(a-c). Cross sections taken along the Y direction indicates a soliton full width at half maximum of $5\mu\text{m}$. Reference: [131].

threshold of 1.3 mW (figure 3.6(h)) for soliton switching, an abrupt decrease in the intensity and an increase in width of the wavepacket was observed. On further reducing the pump intensity $P_{wb} < 1$ mW, only quickly decaying non-solitonic wavepackets are excited. For pump momenta that are below the point of inflection, the writing beam triggers switching of the whole pump spot [87] and no soliton formation is observed.

Figure 3.7 shows two dimensional images of solitons. The soliton size along the Y coordinate perpendicular to the propagation direction (see figure 3.1) at 30-40 ps is $\approx 5\mu\text{m}$, narrower than the initial beam size. This indicates suppression of diffraction and localization in the direction where polaritons have a positive effective mass. Whereas localisation in the X direction described above arises from the interplay between the negative effective mass and repulsive interactions, the origin of localisation along Y is different. The exact nature of this effect it still not entirely understood. Two known possibilities exist, both of them were discussed in 1.7.4. On the one hand it can be interpreted in terms of the phase dependent parametric nonlinearity and the interaction of propagating fronts using Maxwell point formalism. On the other hand it can be a selffocusing effect due to satura-

tion of the local pump field (see figure 1.26).

§ 3.3.4 Soliton energy-momentum spectrum

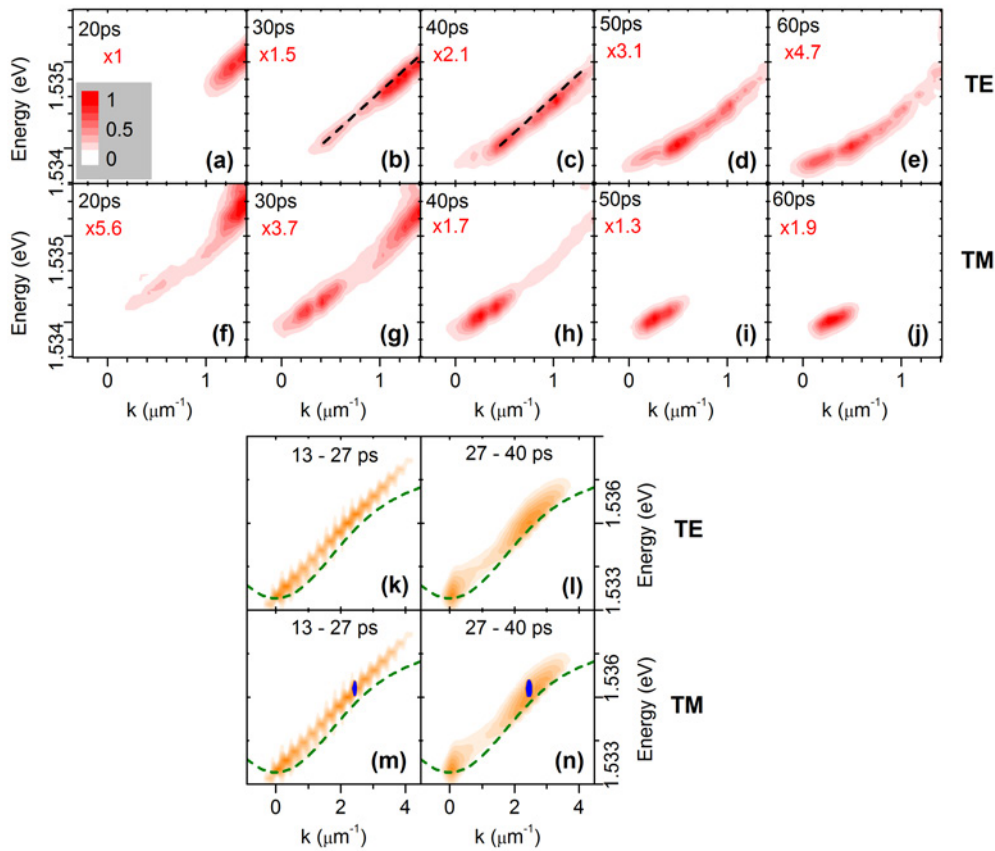


Figure 3.8. Images of polariton emission in energy-momentum space taken at different times after the application of the writing beam in TM (bottom panels) and TE (top panels) polarisations. (a - j) - experimental data, (k - n) - theoretical simulations. Dashed line is a linear fit to the experimental measurements. The energy resolution of 0.1 meV limits the time resolution to ≈ 10 ps. Reference: [131].

The soliton formation can also be viewed as scattering of pump polaritons into a continuum of harmonics spanning a broad range of transverse momenta from 0 to $2k_{pump}$ (see figure 3.3(a)) [115]. Measurements of the energy-momentum ($E(k)$) profile of the solitonic wavepackets over time, as shown in figure 3.8, confirm this point. Initially, for $t < 20$ ps, the polari-

ton emission is concentrated mostly close to k_{pump} , whereas at later times (30-40 ps) the emission is distributed over a broad range of momenta, a characteristic feature of soliton formation [115]. The soliton spectra are expected to form a straight line tangential to the dispersion of nonsoliton radiation [28, 115]. Indeed, the measured dispersion at 30-40 ps can be approximated by a straight line (dashed lines in figure 3.8(b,c)), which is in agreement with numerical modeling [131]. However, soliton emission forms at k -vectors $k \geq 0.5 \mu\text{m}^{-1}$ and spans over the point of inflection, where the dispersion of non-interacting polaritons is also close to linear. Nevertheless, the difference between the solitonic dispersion observed in experiment at around 30-40 ps and the dispersion of the nonsoliton polaritons observed at later times ≥ 50 ps is clear from the data shown in figure 3.8¹. The soliton velocity, $\frac{1}{\hbar} \frac{\partial E}{\partial k}$, deduced from the dashed lines in Figs. 3.8(b, c) is $\approx 1.6 \mu\text{m}/\text{ps}$, consistent with the measurements in figure 3.3 and the numerical modeling [131].

Figure 3.8 represents only a single energy-momentum cut along $k_y \approx 0$. The full k -space map (figure 3.9) provides an excellent comparison between the k -space distribution of a propagating soliton and a dispersive wavepacket. It was obtained by scanning the k -space imaging lens in two dimensions in its plane. Figures 3.9(a)-(j) show soliton k -space maps at different times, corresponding to those shown in figure 3.8, in TE and TM polarisations of detection. Figures 3.9(k)-(n) show k -space maps of a dispersive wavepacket excited with exactly the same writing beam but with the pump switched off. A notable feature of the soliton k -space map is its nar-

¹When spectral emission is time-resolved the resolution of the setup is limited to $\Delta t \approx 15$ ps. This spreading appears because each ray that is diffracted by two adjacent grooves of the diffraction grating is delayed by λ in the first diffraction order. Overall, the time spreading introduced is $\Delta t \sim 1/\Delta\lambda$, where $\Delta\lambda$ is the spectral resolution of a single monochromator. This problem can be overcome by using a double monochromator.

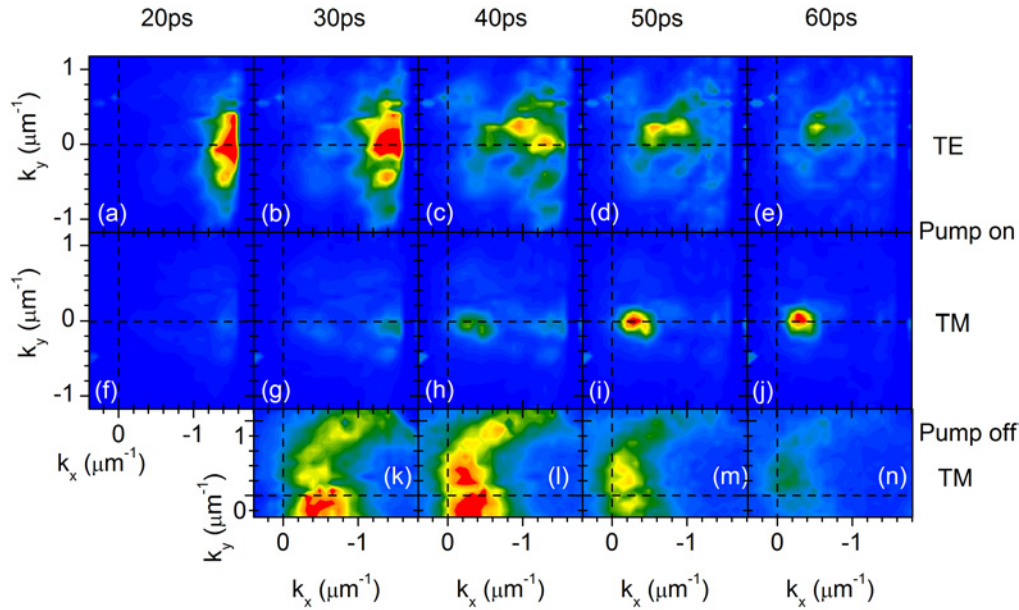


Figure 3.9. K-space map of the soliton ((a)-(e) in TE polarisation and (f)-(j) TM) and a dispersive wavapecket ((k)-(n) in TM polarisation).

row spectrum concentrated along $k_y \approx 0$. This is expected since there is no spreading along the y direction and all parametric processes that stabilise soliton along the x direction involve k vectors with $k_x \neq 0$ and $k_y = 0$. The difference in TE and TM polarisations can be reproduced with modelling, as it was already shown in figure 3.8(k) - (n)[131]. By contrast without pump, polariton-polariton scattering from the writing beam populates k -vectors which form a figure of '8' (figure 3.9(k)-(n)), which is notably different from soliton pattern. This process was studied in detail before by Langbein [138].

The experimental results shown are were also confirmed with theoretical modelling. Numerical studies were performed using mean-field equations describing the evolution of slowly varying amplitudes of the TM (E_{TM}) and TE (E_{TE}) cavity modes and of the corresponding excitonic fields $\psi_{TM,TE}$:

$$\begin{aligned} \partial_t E_{TM} - i \frac{\hbar}{2m_c} (\partial_x^2 + \partial_y^2) E_{TM} + (\gamma_c - i\delta_c) E_{TM} = \\ = i\Omega_R \psi_{TM} + E_{pump}(x, y) e^{ik_{pump}x}, \end{aligned} \quad (3.1)$$

$$\begin{aligned} \partial_t E_{TE} - i \frac{\hbar}{2m_c} (\partial_x^2 + \partial_y^2) E_{TE} + (\gamma_c - i\delta_c) E_{TE} = \\ = i\Omega_R \psi_{TE} - iE_{wb}(x, y, t) e^{i\kappa_{wb}x}, \end{aligned} \quad (3.2)$$

$$\begin{aligned} \partial_t \psi_{TM} + (\gamma_e - i\delta_e) \psi_{TM} + \frac{ig}{4} [(1+r)|\psi_{TM}|^2 + 2|\psi_{TE}|^2] \psi_{TM} - \\ - \frac{ig}{4} (1-r) \psi_{TM}^* \psi_{TE}^2 = i\Omega_R E_{TM}, \end{aligned} \quad (3.3)$$

$$\begin{aligned} \partial_t \psi_{TE} + (\gamma_e - i\delta_e) \psi_{TE} + \frac{ig}{4} [(1+r)|\psi_{TE}|^2 + 2|\psi_{TM}|^2] \psi_{TE} - \\ - \frac{ig}{4} (1-r) \psi_{TE}^* \psi_{TM}^2 = i\Omega_R E_{TE}. \end{aligned} \quad (3.4)$$

Here $m_c = 0.27 \cdot 10^{-34}$ kg is the effective cavity photon mass, $\hbar\Omega_R = 4.9867$ meV is the Rabi splitting, $\hbar\gamma_c = \hbar\gamma_e = 0.2$ meV, where γ_c and γ_e are the cavity photon and the exciton coherence decay rates, $\delta_e = -1.84$ meV, $\delta_c = -2.34$ meV, $g > 0$ is the nonlinear parameter, which can be easily scaled away, $r = -0.05$ parameterizes the nonlinear interaction between the two modes [139]. $E_{pump}(x, y)$ is the pump amplitude with the momentum k_{pump} , the corresponding angle of incidence $\theta = \arcsin[\kappa\lambda_p/(2\pi)]$ and E_{wb} is the writing beam amplitude.

For the case of the homogeneous pump $E_{pump}(x, y) = const$ and $E_{wb}(x, y, t) \equiv$

0 the soliton solutions are sought in the form $E_{TM,TE} = A_{TM,TE}(x-vt)e^{ik_{pump}x}$, $\psi_{TM,TE} = Q_{TM,TE}(x-vt)e^{ik_{pump}x}$. The soliton profiles and the unknown velocity v are found self-consistently using Newton-Raphson iterations. In simulations of the soliton excitation the system of equations (3.1)-(3.4) has been solved directly using the split-step method. The results of the numerical study are shown in figure 3.8(k)-(n).

§ 3.3.5 Soliton sustainability

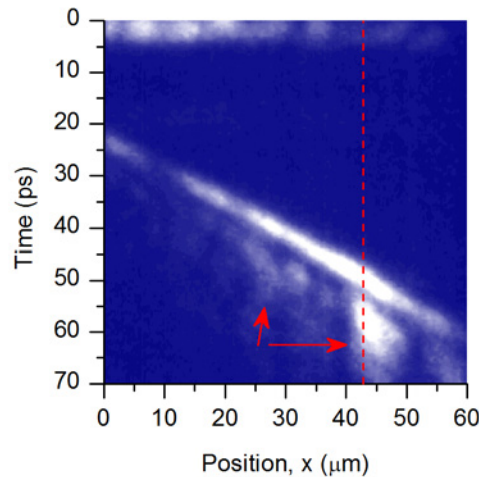


Figure 3.10. Streak camera image of a soliton hitting a photonic defect and continuing propagation afterwards. Soliton hits several defects leaving a trace of scattered polaritons (marked with red arrows), after a major defect at approx. 43 ps it still continues propagation for another 15 μm . In this case soliton travels a distance of 100 μm from the point of initiation by the writing beam.

Another fundamental property of solitons is that they should sustain themselves after collisions with fluctuations which have energy smaller than that of a soliton. Figure 3.10² shows a soliton hitting a defect. During the collision the soliton loses part of its polaritons on the defect, but re-

²This image is taken at a later time compared to the original data, during which the sample has degraded. Also, this soliton is σ^+ polarised, see chapter 4.

plenishes them quickly and continues propagating until it reaches the end of the pump spot. Polaritons scattered from the soliton relax down to $k \approx 0$ and escape the cavity within the polariton lifetime. This is another proof for the solitonic nature of the observed wavepackets. Further discussion of soliton sustainability is presented in the next section 3.4.

§ 3.4 Coherent control of soliton

Soliton formation is triggered by the coherent writing beam. A detailed picture of the process can be described in the following way. The writing beam creates a very high density wavepacket of polaritons, which then propagates and once it reaches the pump bistability region (if seeded outside) it triggers soliton formation. Importantly, polariton solitons created by the writing beam stimulate polariton-polariton scattering from the pump. Since their phase is related to the writing beam, the resultant phase of soliton harmonics will be also linked to the writing beam phase due to the stimulated scattering.

In general the soliton field amplitude can be described as:

$$S(t) = \int A(k, \omega) e^{i(\omega t + kx)} dk, \quad (3.5)$$

where $A(k, \omega)$ is the complex amplitude: $A(k, \omega) = |A(k, \omega)| e^{i\varphi_k}$. At k_{wb} , the writing beam k-vector, $\varphi_k = \varphi_{wb}$ due to stimulated scattering. The phases of different soliton harmonics are related through the scattering. Therefore

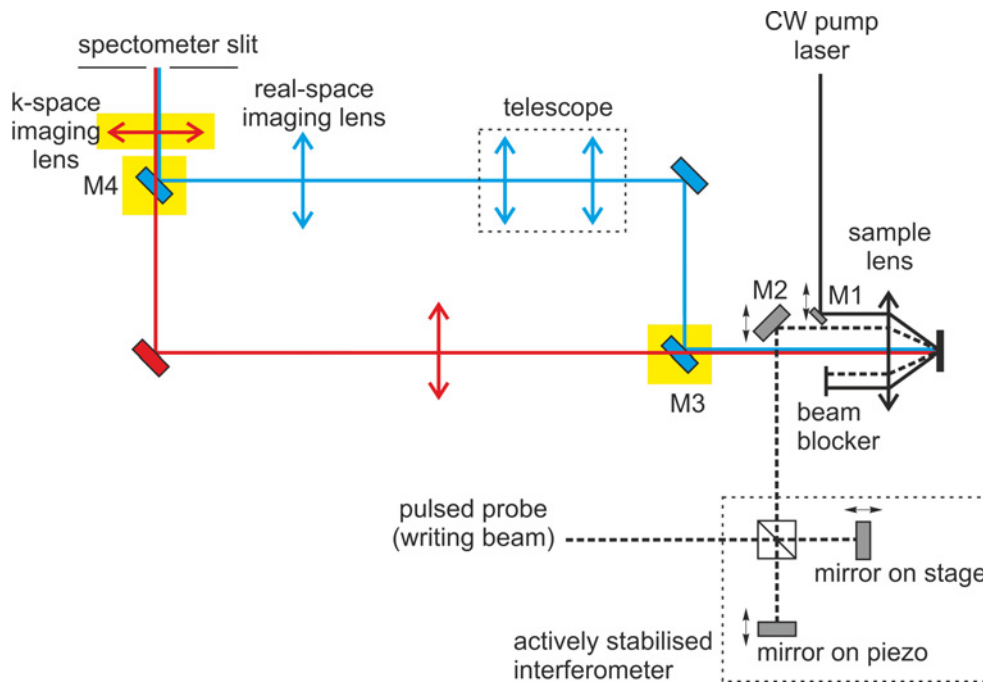


Figure 3.11. A scheme of coherent control experiment. Original pulsed beam after passing through pulse shaper (not shown) is sent to the Michelson interferometer, which has one mirror mounted on a piezo stage for precise phase control and the other is mounted on stage to adjust its relative delay. The interferometer is actively stabilised by applying additional CW laser (HeNe) beam along the pulsed beam path (not shown), which is then reflected from the main beam path using spectrally selective mirror. Interference pattern of the two red HeNe beams is then projected on two photodiodes, then signals from the two PD through feedback electronics are transformed into needed piezo displacement needed to maintain the same phase shift.

it is possible to say that the writing beam defines the phases of all soliton harmonics. The experiment described in this section proves this point.

The setup for the coherent control experiment is shown in figure 3.11. An actively stabilised interferometer³ is used to select and fix the relative phase shift between beams going through two arms of the interferometer. One of the beams (that arrives first) is used as a writing beam to the trigger soliton. The second, control beam, is positioned on the soliton's path and its delay is adjusted to match the time so that it 'hits' the soliton during propagation.

³The interferometer was developed by Dr A. J. Ramsay.

In this experiment, the pump and writing beam were both linearly co-polarised (TM) while detection was conducted in TE polarisation. A summary of the observations is shown in figure 3.12. The first writing beam arrives at 0 ps, the second arrives at approximately 24 ps. The left column corresponds to 'anti-phase' observation, i.e. the regime when the 2nd beam phase is shifted by π with respect to the phase of the soliton harmonic, when destructive interference takes place between the control beam and soliton. The right column corresponds to 'in-phase' observation, for the case of constructive interference, when the phase shift is zero.

The control beam reflection arrives at the streak camera at approximately 24 ps after the writing beam (red dashed line in figures 3.12(a) and (b)). It takes some time for the beam to penetrate the cavity and interfere with the soliton. Figures 3.12(c) and (d) show real-space image of a soliton at time $t = 20$ ps before the control pulse arrival. Then figures 3.12(e) and (f) show how the soliton was influenced by the control beam. In the case of destructive interference (figure (e)), the soliton is heavily distorted and spreads to about $15 \mu\text{m}$ in the transverse direction and its intensity is also decreased by approximately 50%. After constructive interference it is only amplified while maintaining its shape (figures (f) and (b)). Nonetheless, 10 ps later, at time $t = 40$ ps, the soliton recovers itself (figure (g)) after a 'smash' by the control beam shown in figure (e). The soliton continues its propagation as well after the 'in-phase' control beam (figure (h)).

The effect that the control beam has on the soliton can be understood from figure 3.13. The writing and control beam spectra are schematically shown as a blue ellipse, while the soliton spectrum is shown in orange, similarly to figure 3.3(c). The two spectra can only interact in the energy-

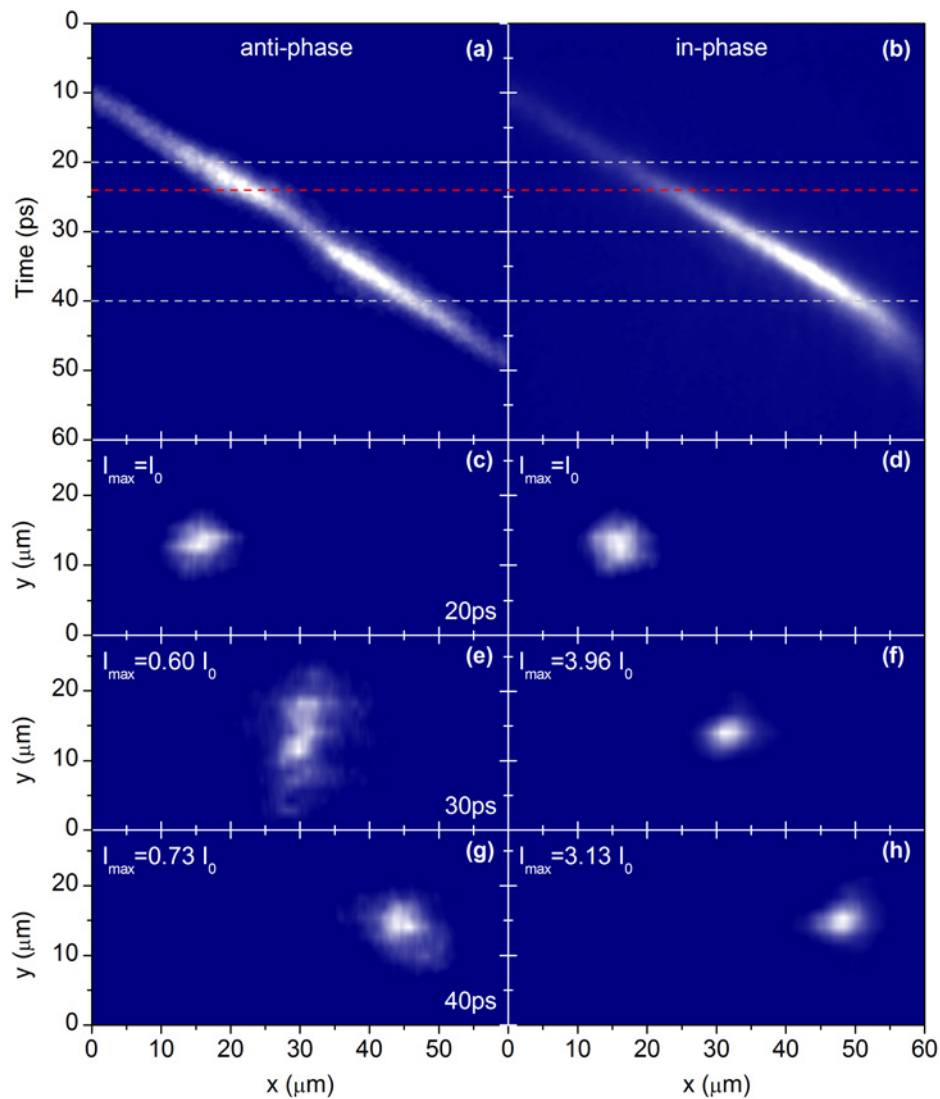


Figure 3.12. Summary of coherent control experiments. (a) and (b) show streak camera images taken along soliton propagation, red dashed line corresponds to arrival of the control beam and grey dashed lines show times of 20, 30 and 40 ps for which full two-dimensional images (c)-(h) are shown below. Left column corresponds to 'anti-phase' measurement and right to 'in-phase'.

momentum area where the two ellipses overlap; effectively all other areas of the soliton spectrum remain intact. Therefore, in the case of destructive interference, only a part of the soliton spectrum is depressed, which leads to a noticeable distortion of the soliton shape as well. However, due to efficient scattering processes from the pump, the soliton spectrum is regenerated and its original shape is restored as well. Furthermore, if the distortion introduced by the control beam is big enough, it can possibly break a single soliton into several solitons. In the case when interference is constructive, the soliton spectrum is simply amplified and the soliton becomes brighter without any significant distortion to its shape.

An additional difficulty with interpreting these results arises from the fact that the soliton polarisation state is not clearly defined in the case of linearly polarised pump and writing beam. The polarisation properties of solitons are discussed in the next chapter.

Overall, it was possible to coherently probe the soliton by using the second phase-locked writing beam. The constructive interference leads to the amplification of the soliton, while the destructive interference leads only to a distortion of the soliton, and it later restores its original shape.

§ 3.5 Comparison with the TOPO

The soliton observations have a very different physical origin to the triggered optical parametric oscillator observations of Ref. [109]. In that case,

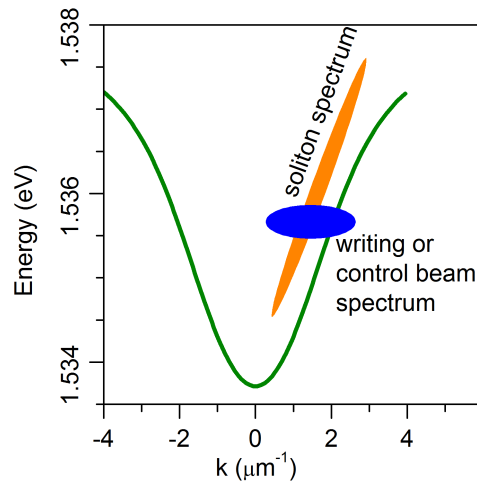


Figure 3.13. A sketch of soliton and control beam spectra, showing their limited overlap.

the system is already in a high density phase before a writing beam is applied and furthermore the system was pumped at low k_{pump} in the region of positive effective mass, where soliton generation cannot occur. As a result, propagating excitations of the polaritonic condensate were studied, as opposed to the bright solitons. If the whole pump spot is switched on, i.e. the system is in the upper state in the bistability region or the k -vector of the pump is above the upper bistability threshold, then a soliton can not be formed. This is demonstrated in the following experiment.

Firstly, the system is set to the upper state (figure 3.3(c)), where a condensed 'signal' state is formed at $k = 0$, with long range spatial coherence over $30 \mu\text{m}$, due to polariton-polariton parametric scattering from the pump state into 'signal' and 'idler' states at $k_{signal} = 0$ and $k_{idler} = 2k_p$. This corresponds to the polariton optical parametric oscillator (OPO), which was studied in [7].

Secondly, a pulsed writing beam (wb) is introduced at $k_{wb} \approx 1.2 \mu\text{m}^{-1}$ focused to a small spot of $\approx 7 \mu\text{m}$ and the propagation of the resulting

wavepacket is observed. The wavepacket is amplified due to polariton-polariton scattering from the switched-on pump state and hence propagates macroscopic distances, superimposed on the signal condensate at $k = 0$. Such a process corresponds to the so-called triggered OPO (TOPO), firstly reported by Amo et. al. [109].

The TOPO propagating wavepacket exhibits very different physical properties to the soliton. Figure 3.14(a) shows the TOPO intensity as a function of time and position X (see figure 3.3(b)) for $k_{pump} \approx 2.38 \mu\text{m}^{-1}$. It is seen that the TOPO wavepacket propagates over long distances of up to $50 \mu\text{m}$. However, in contrast to the soliton propagation, it broadens significantly from $7 \mu\text{m}$ up to $15 - 20 \mu\text{m}$ within $\approx 40 \text{ ps}$ time and propagates at a speed 1.3 times slower than the observed soliton. Moreover the TOPO wavepacket intensity decays with time, again in marked contrast to the soliton behaviour of figure 3.6(g).

The TOPO wavepacket created by the writing beam can be considered as a condensate excitation, which has the properties of a diffusive Goldstone mode [82]. There is competition between polariton-polariton scattering from the pump to the signal state at $k = 0$ and to the localised TOPO wavepacket at k_{wb} . Since the pump state is switched on over the whole excitation spot there are no excitations in the pump state itself. The TOPO wavepacket propagation speed is determined only by the writing beam k -vector $k_{wb} \approx 1.2 \mu\text{m}^{-1}$ and not by that of the pump as in the case of a soliton. The TOPO wavepacket expands since the polariton dispersion at $k_{wb} \approx 1.2 \mu\text{m}^{-1}$ is described by a positive effective mass.

The time dependence of the TOPO wavepacket FWHM is expected

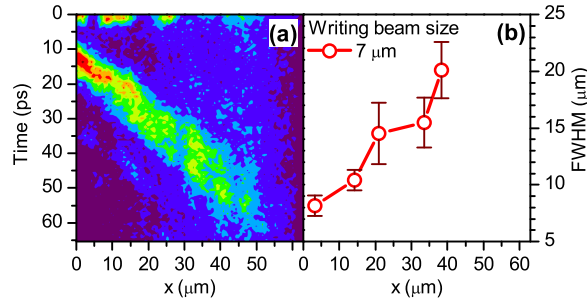


Figure 3.14. (a)- streak camera trace of propagating TOPO wavepacket as a function time and position recorded for $k_{pump} \approx 2.38 \mu\text{m}^{-1}$ and writing beam size $7 \mu\text{m}$. (b) - size (FWHM) of TOPO wavepacket recorded in panel (a) as a function of position.

to be strongly dependent on the initial size of the writing beam. It can be easily shown from the solution of a time dependent Schrodinger equation that the FWHM of a noninteracting wavepacket with initial FWHM Δ with a dispersion described by positive effective mass m_{eff} is given by $2\sqrt{\Delta^2/4 + \frac{\hbar^2}{m_{eff}^2\Delta^2}4t^2}$. It is seen that the size of the wavepacket will increase with time more slowly for initially larger Δ . This is consistent with the above observation (wavepacket with initial size $7 \mu\text{m}$ is expected to spread up to $\approx 20 \mu\text{m}$ within 50 ps) and those in [109], where the TOPO wavepacket of a size $15\text{-}20 \mu\text{m}$ along the propagation direction is initially created and its size changes very little within 40-50 ps. Indeed, using the above formula we can estimate that it should increase only by 2 microns for $m_{eff} \approx 10^{-34} \text{ kg}$.

§ 3.6 Discussion and conclusions

The experimental observations of bright polariton solitons reported above open opportunities for the exploration of their potential applications in ul-

trafast information processing, since their picosecond response time is three orders of magnitude faster than that observed for the pure light cavity solitons in VCSELs [110, 140, 34]. Furthermore, polaritonic nonlinearities are 2-3 orders of magnitude larger than nonlinearities in VCSELs [110, 140, 34]. The measured transverse dimensions of polaritonic solitons are $\approx 5 \mu\text{m}$ (resolution limited), whereas the numerical model using the experimental parameters predicts $\approx 2 \mu\text{m}$, several times less than the $10 \mu\text{m}$ width typical for VCSEL solitons. Polariton solitons can potentially be used as more natural information bits than the propagating domain walls in the recently proposed integrated polariton optical circuits and gates (polariton neurons) [86]. The number of polaritons in the solitons observed is of the order of hundreds, which puts them into the category of mesoscopic structures. The realisation of spatially modulated 1D microcavity structures, with reduced numbers of particles, may create conditions for the observation of quantum solitons and nonlinear functionality relying on few polariton quanta, potentially allowing designs of quantum polariton-soliton circuits. Finally, unlike the well-studied polariton condensates which correspond to macroscopic occupation of a single state in momentum space, the highly occupied polariton soliton is strongly localised in real space with a broad spread in energy and momentum.

Chapter 4

Polarisation properties of polariton solitons

Polariton solitons that arise due to bistability and parametric instability of polariton systems are expected to have rich polarisation properties, since, as it was shown earlier, resonantly driven polariton states may exhibit polarisation multistability.

Excitons in GaAs semiconductor quantum wells with the same spin repel, whereas excitons with opposite spin attract weakly. Such anisotropy in exciton-exciton interactions is shown to be responsible for the rotation of the linear polarisation of scattered polaritons by 90° in polariton-polariton scattering process [125] as was demonstrated earlier in chapter 2. N. Gippius *et al.* predicted in 2007 [85] that if the lower polariton branch is driven resonantly by a linearly or slightly elliptical polarised beam then the polarisation degree of the internal pump field inside the microcavity may acquire different linear (elliptical) or circular polarisations depending on the

pumping history. Later experiments confirmed such predictions. Given that bright polariton solitons are supported by both parametric scattering (parametric instability) and polariton pump bistability, the question is what kind of soliton polarisation can be realised in the case of a circularly or linearly polarised pump.

Furthermore, as was shown in chapter 2, the effect of incoherent reservoir and non-linear spin dependent absorption may also play an important role in the spin properties of polariton solitons.

§ 4.1 Experimental setup

One of the main experimental challenges in the observation of polariton solitons is the stability of the setup. In order to access the sample from a wide range of angles only cold finger cryostats can be used, which causes a major source of mechanical vibration to be transferred along with helium by a transfer tube. When in operation, the transfer tube is connected to both the cryostat and helium dewar, therefore the optical table cannot be used in its active damping regime, which also influences the stability of the lasers used. Finally, lasers are subject to fundamental power output fluctuations of the order of a few percent. The main implication of these fluctuations is a sudden switching on of the OPO process and loss of any soliton propagation. Measures taken to improve the performance the setup included tighter positioning of the lasers, room's better temperature stability and increasing

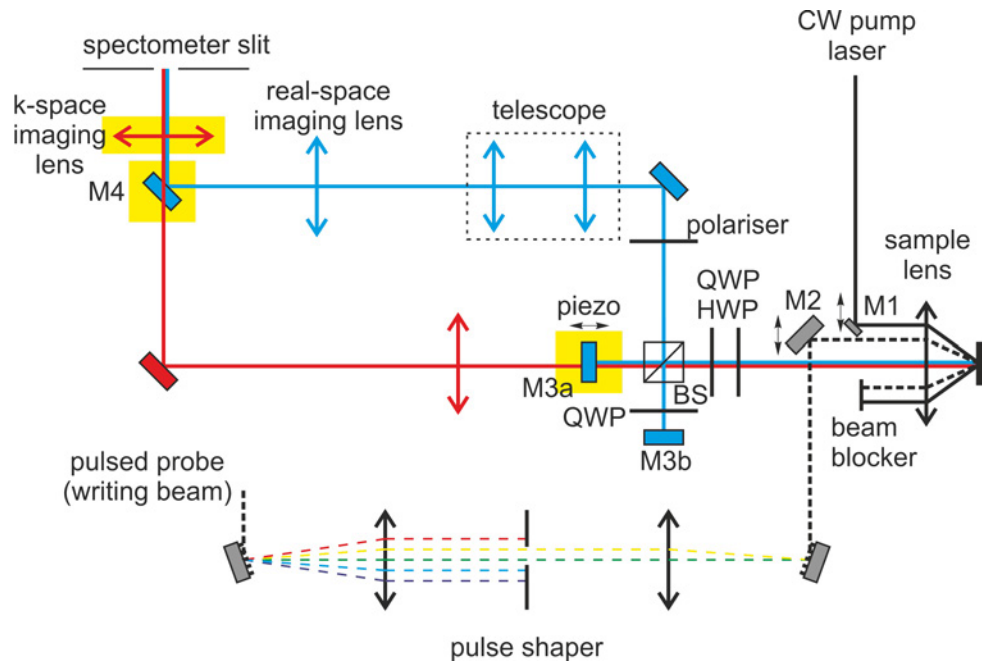


Figure 4.1. A modified experimental setup for polarisation detection. Mirror M3 (see figure 1.33) is replaced with Michelson interferometer (M3a and b) with variable arm length.

power output of the lasers. The latter allowed the possibility of observing bistability over an increased range, since it was possible to pump the system with higher laser energy detuning.

Soliton formation and propagation conditions are extremely sensitive to these fluctuations of laser power and position. In practice this means that any streak camera image taken over a propagating soliton is an average of different conditions. This, nevertheless, allowed reliable measurements to be taken, that were presented in the previous chapter.

In the case of polarisation measurement, a full Stokes vector has to be measured, which consists of six measurements: two for each polarisation basis: TE and TM for Q -component; two cross-diagonal for U -component; σ^+ and σ^- for V -component. With only one streak camera this is only possi-

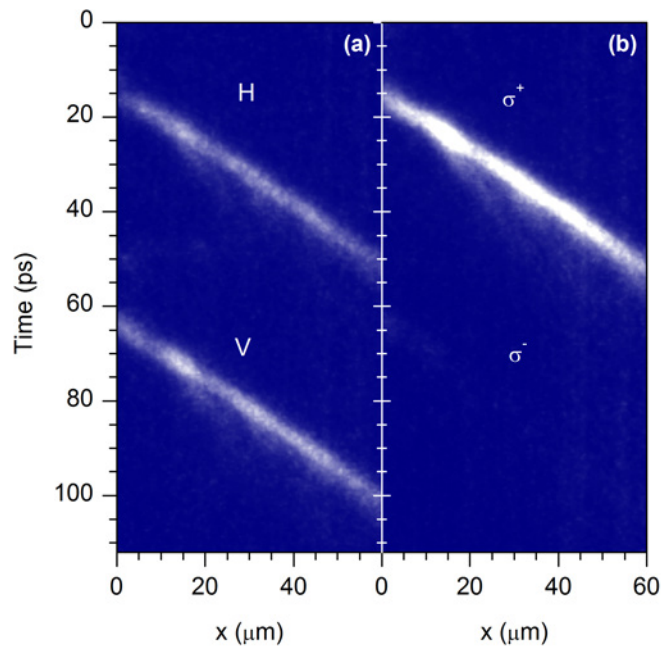


Figure 4.2. Traces of a single σ^+ polarised soliton recorded in linear (H-V) basis (a) and circular ($\sigma^+\sigma^-$) - (b).

ble with successive measurements of each polarisation. To provide accurate results most of the fluctuations have to be accounted for. This is done with the setup shown in figure 4.1.

Mirror M3 (as shown in figure 1.33) is replaced with a beamsplitter (BS) and two mirrors, which effectively form a Michelson interferometer, in front of which a quarter wave plate (QWP) and a half wave plate (HWP) convert any desired basis into a linear X-Y basis. Importantly, one arm of the interferometer is set to have a longer optical path in a way that emission from it arrives approx. 100 ps later than from the other one, still within one frame of the streak camera. At the same time one of the arms has a QWP with its fast axis rotated 45° to the laboratory X-Y basis. Therefore, after emission passes twice through the QWP, its polarisation components are rotated by 90° and two orthogonal polarisations are detected simulta-

neously. To eliminate interferometer alignment errors, this measurement is performed twice with orthogonal polarisations being swapped by the QWP+HWP set before the BS. Additionally, M3a is mounted on a piezo-stage to enable interference measurements. An example of detection of a circularly polarised soliton in the H-V (X-Y) basis using such technique is shown in figure 4.2(a). Detection in the circular basis is shown in figure 4.2(b), which also confirms the proper operation of the setup: in circularly polarised basis only σ^+ emission is observed, as expected, whereas in H-V basis both H and V components have the same intensity.

§ 4.2 Soliton polarisation multi-state behaviour

To study soliton polarisations consistently, full Stokes components of soliton emission (as described in the previous section) were measured for three different writing beam polarisations (σ^+ , TE, σ^-) while changing the pump polarisation from σ^+ through TM to σ^- . The main subject of the study was the degree of circular polarisation (DCP) of a soliton, as defined in (2.1).

Figure 4.3 shows streak camera soliton traces taken for different detection polarisations in the cases of different pump and writing beam polarisations (rows). All of them show that soliton polarisation is constant over its propagation time. First, when the pump and writing beams are both σ^+ (σ^-) polarised, the excited soliton is also σ^+ (σ^-) polarised (figure 4.3 top row, σ^- not shown). When the pump is linear, the soliton polarisation is defined by the polarisation of the writing beam: σ^+ (σ^-) writing beam triggers σ^+ (σ^-) polarised soliton, which is shown on the second (third) row in figure 4.3. However, when the pump and writing beam are both linearly polarised, soliton emission is detected in all polarisations.

Additionally, soliton DCPs for pump and writing beam polarisations (shown in figure 4.3) as a function of time are plotted in figure 4.4 for times when soliton propagation is observed, which further confirms this point. This is in contrast to what was observed in simple ballistic propagation of wavepackets, where polarisation beats occurred due to TE-TM splitting [141], which indicates the effective quenching of TE-TM splitting

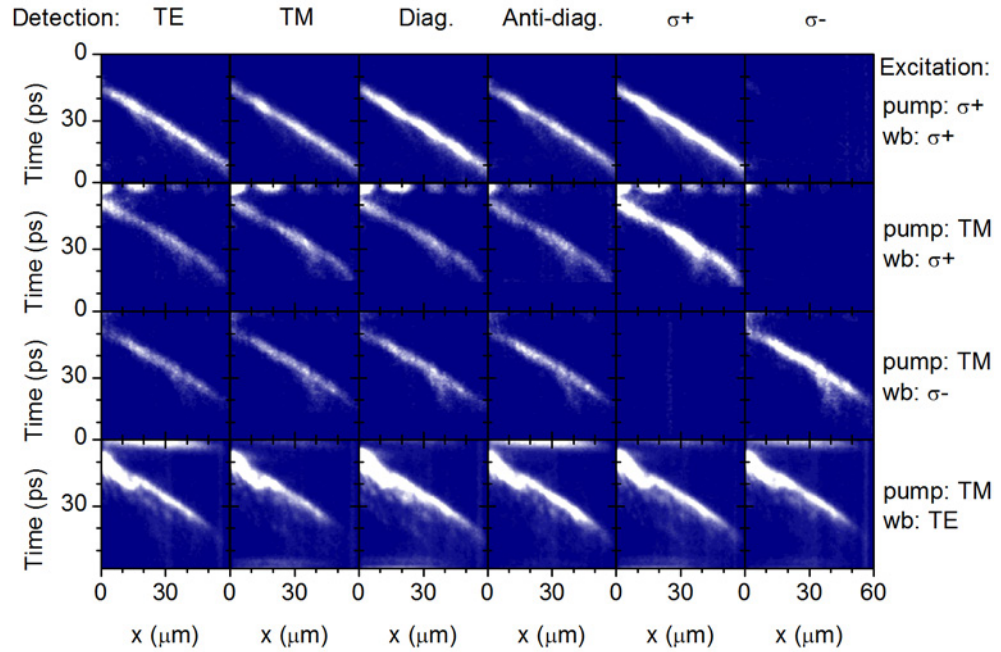


Figure 4.3. A set of streak camera images taken for selected pump and writing beam polarisation configurations taken for different detection polarisations: TE ($=x$), TM ($=y$), a (diag.), b (anti-diag.), σ^+ , σ^- , which show constant soliton polarisation over its propagation range.

in the soliton regime: the energies of both TE and TM polariton components at $k = k_{pump}$ are tuned into resonance with the pump energy in the high density regime. At low excitation densities, the TE-TM splitting of polariton modes is of the order of 0.1 meV at high k-vectors, meaning that the polarisation of the broad polariton wavepacket excited at high momenta oscillates between σ^+ and σ^- polarisations with a period of 20 ps, while over the whole duration of the soliton pulse (approximately 30 ps), DCP is nearly constant.

A systematic study of soliton polarisation as a function of the pump DCP was performed for σ^+ -, TE- and σ^- -polarised writing beam. The pump DCP was changed from -1 through 0 (TM polarisation) to +1. For every pump DCP the full Stokes vector of the soliton emission was obtained in a

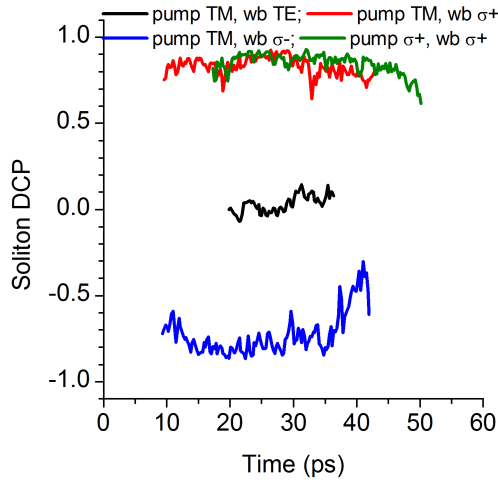


Figure 4.4. Soliton DCP as a function of time for the same sets of pump and writing beam polarisation as in figure 4.3 (data is cut to show the DCP only during soliton actual propagation).

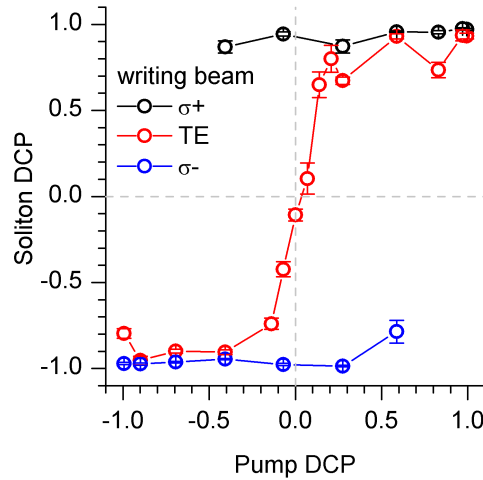


Figure 4.5. Soliton degree of circular polarisation as a function of the DCP of the pump for three different writing beam polarisations (σ^+ , TE, σ^-).

manner described above.

The result of the study of soliton DCP is presented in figure 4.5. It shows that σ^+ (σ^-) solitons can be excited in the range of the pump DCP from 1 to -0.1 (-1 to 0.1) with σ^+ (σ^-) polarised writing beam. It is interesting that for the case of a linearly polarised writing beam, a slight bias of the pump DCP towards σ^+ or σ^- polarisation by 0.1 quickly ensures robust excitation of either σ^+ or σ^- circularly polarised solitons with the DCP of 0.85 - 0.95, respectively. Additionally the linear polarisations of solitons were measured. These results are shown in figures 4.6 and 4.7, which, as expected, show a negligible degree of linear polarisation (DLP) for elliptically polarised solitons. Furthermore, the DLP of a soliton in the case when the pump and writing beams are linearly polarised is also nearly zero.

For a circularly polarised writing beam, it is only possible to excite solitons of that polarisation, and it is only possible when the pump has suf-

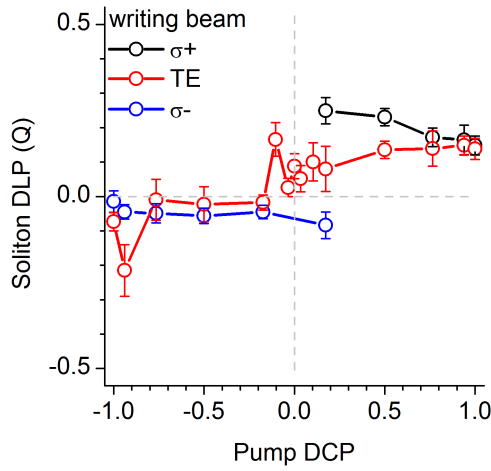


Figure 4.6. Soliton degree of linear polarisation, Q , as defined in (1.6) as a function of DCP of the pump for different writing beam polarisations (σ^+ , TE, σ^-).

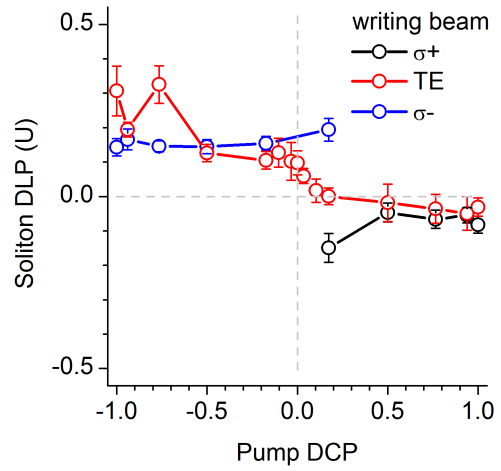


Figure 4.7. Soliton degree of diagonal linear polarisation, U , as defined in (1.6) as a function of DCP of the pump for different writing beam polarisations (σ^+ , TE, σ^-).

sufficient power to sustain the bistability at the polarisation. When the pump has $\text{DCP} = +1$, only solitons in σ^+ polarisation can be excited with a linearly polarised writing beam, because polariton-polariton scattering from the pump populating soliton spectrum conserves polariton spin.

A linearly polarised writing beam which contains both circular polarisations is capable of triggering solitons of both polarisations, a σ^+ and/or σ^- , depending on the pump polarisation. In the case of a linearly polarised pump, the soliton circular polarisation degree is determined by the writing beam polarisation. When the writing beam is circularly polarised, the DCP is about 0.95 over the soliton propagation time (figure 4.4). Such a behaviour arises from the polarisation multistability experienced by the linearly polarised pump. The polarisation of the writing beam determines which polarisation component of the pump will penetrate inside the cavity in the soliton regime. When a σ^+ (σ^-) polarised writing beam arrives, it

creates polariton population causing the blueshift of only σ^+ (σ^-) polarised pump polaritons, since the interaction between σ^+ and σ^- polariton is weak. As a result, only σ^+ (σ^-) polarised solitons are excited. It is interesting that when the pump and writing beams are both linearly polarised, the soliton emission is found to be unpolarised with the degree of circular and linear polarisations being of about 0.1 – 0.2. In this case, the total soliton emission seems to be depolarised. This specific case is addressed in the next section.

In the experiments described in this section, the pump power was kept constant for all pump DCPs. As the pump DCP was changing, the effective power in each of the circular polarisations was changing as well, which required adjustment of the pump excitation angle in order to maintain the system in the bistable regime in the low density state. The adjustment range was of the order of $\pm 0.07^\circ$, which corresponds to a $\Delta E \approx 0.03$ meV change in the relative detuning of the LPB and the pump. While it was possible to excite solitons with a full range of pump DCPs from -1 to +1 in the experiment, the theoretical model used previously (equations (3.1)-(3.4)), provides soliton solutions only in the range of the pump DCPs from -0.45 to +0.45 for the small ΔE values used experimentally. This is most likely due to the fact that the theory does not account for spin-dependent nonlinear absorption (possibly due to the biexciton resonance) or the pump and soliton interactions with an incoherent reservoir, as was discussed in Chapter 2.

Figure 4.8 shows the writing beam threshold power versus the pump DCP for different writing beam polarisations. The threshold power for fully circularly polarised (σ^+) writing beam remains constant and then increases as the pump DCP is changed from -1 towards +1. This can be explained by

a decrease of the effective pump power in that circular polarisation when its DCP is decreased. Hence, a higher writing beam power is required to excite a soliton. The same is observed for a σ^- polarised writing beam when the pump DCP is changed from -1 towards +1.

A linearly polarised writing beam presents an interesting case. Initially, when the pump DCP = 1, the threshold power for a TE polarised writing beam is expected to be twice of that when the writing beam is circularly polarised, since only half of the TE polarised writing beam power is used to trigger circularly polarised solitons. If one assumes that there is no interaction between the σ^+ and σ^- polarisation components among the polaritons injected with the writing beam, a peak in the dependence of the writing beam threshold power is expected to appear when the pump is also linear, following the same argument as in the previous paragraph. It is known though that the interaction between σ^+ and σ^- polaritons is weak. This suggests that the nonlinear spin-dependent absorption and incoherent reservoir plays significant role in the soliton formation process.

Finally, the nonlinear effect of the writing beam density on the intracavity field can be seen in figure 4.9: by changing the writing beam power 5 times, unpolarised soliton emission is observed within the range of pump DCP from approximately -0.25 to +0.25. A change of the writing beam power results in an unbalanced population of σ^+ and σ^- polaritons in the reservoir, which may cause this effect. However, the exact mechanism of the process is not yet entirely understood.

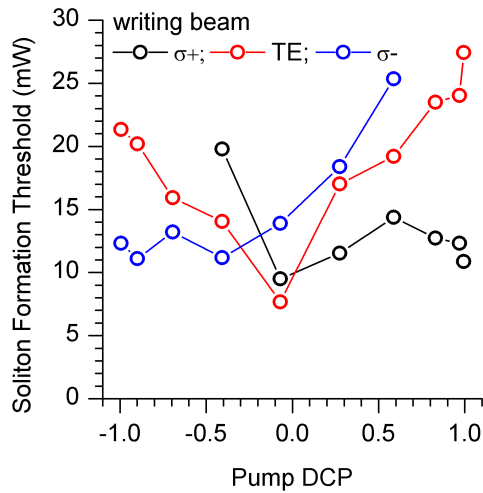


Figure 4.8. Dependence of soliton excitation threshold as a function of degree of circular polarisation of the pump for three different writing beam polarisations (σ^+ , TE, σ^-).

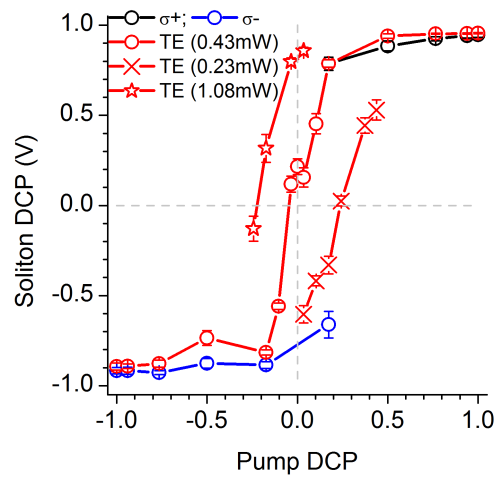


Figure 4.9. The effect on soliton polarisation of effective internal field of polaritons created by the writing beam as a function of different writing beam powers.

§ 4.3 Linearly polarised pump and writing beam

All of the time-resolved data presented here is acquired using the streak camera image integration method, when each separate image is obtained by overlaying typically millions of 'single shot' images. On the one hand, this means that all fluctuations are averaged and a better quality image is obtained. On the other hand, specifically in the case when the detected intensities in all polarisations are the same, it introduces a question about what is actually measured.

There are several possible effects that can happen, and which will produce exactly the same output on the streak camera. The *first* option is that in reality only σ^+ and σ^- solitons can be excited. In this case, when the

pump and writing beam are nearly linear, the probability of exciting each of them is equal, and the actual soliton polarisation excited depends on purely random fluctuations present at the time of excitation. Therefore, when the pump DCP is 1, the observed soliton DCP also tends to 1 as the number of solitons observed tends to infinity, with one thousand solitons already being a sufficiently large number to see the effect. As the pump polarisation becomes slightly elliptical, one of the components obtains a higher probability to be excited with a linear writing beam, and the ratio will now increase (decrease) if the pump ellipticity is changed towards σ^+ (σ^-). A different prediction that any linear soliton is unstable and breaks down to circularly polarised [142] also leads to the same statistics of circularly polarised solitons.

The *second* option is that the excited soliton has a random polarisation, but clearly defined, each time it is excited, with a tendency towards the pump ellipticity. Finally, the *third* option is that a soliton is completely unpolarised each time it is excited and contains emission in all polarisations, or that is contains at least several polarisation components in a single pulse. Hence the soliton state is mixed rather than pure. These possibilities can be conveniently represented on Poincaré sphere as shown in figure 4.10.

An attempt to evaluate these options was made using Hanbury-Brown Twiss (HBT) correlation setup. In addition, the photon counting module of the streak camera was used to collect single shot data from individual solitons. At the time of writing, these arrangements have been tested and evaluated, however; data is not yet available.

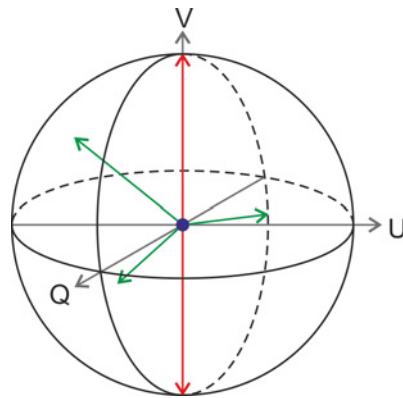


Figure 4.10. Possible soliton polarisations on Poincaré sphere. Each vector corresponds to the polarisation of a single soliton. Red vectors correspond to the case when only σ^+ and σ^- solitons exist. Green vectors show a few random polarisations as the second option, notably all vector have unit length and end on the sphere surface, so that each individual soliton is fully polarised. Blue dot correspond to the third option - each soliton is fully unpolarised.

§ 4.4 Discussion and conclusions

Polariton solitons are shown to exhibit rich polarisation properties. Using the same linear pump polarisation it is possible to excite solitons in three different polarisations: σ^+ , σ^- and, presumably, unpolarised. It is worth mentioning that this behaviour is deterministic and depends on the writing beam polarisation.

For the case of a linearly polarised writing beam, a sharp transition between σ^+ and σ^- soliton polarisation occurs, when the pump DCP is changing its sign passing through zero. It was shown that this is not a statistical effect of the image integration on the streak camera, but a real change in the polarisation state of soliton, however, there is no definite answer at this time about the exact nature of this polarisation state.

It is important to point out the close link between these observations and the previously observed spin switch effect [87], where a writing beam

was able to trigger the switching of the whole pump area. This is also one of the manifestations, along with spin rings [121, 130] and 'polariton neurons' [86], of polariton cross-polarisation interactions.

One very promising future research direction is to make two solitons with orthogonal polarisations collide against each other for pumps with different degrees of ellipticity. Another interesting question, which should be addressed, is the stability of unpolarised solitons compared to fully circularly polarised.

Chapter 5

Polariton soliton arrays

Soliton pattern formation has been previously observed in many systems, for example, the breaking of atomic BEC into a soliton train [25] in ^7Li . The formation of dissipative soliton patterns has been extensively studied in microcavity resonators in the weak-coupling regime [110, 111, 112]. The mechanism of formation of these solitons differs from that studied in this work: these cavity solitons can arise from stabilisation of periodical patterns in dissipative resonators [113] or their formation can be triggered by an external probe while the system is in the bistable regime [110]. Key properties observed are: mobility of such solitons as they move in space towards more favourable locations; the permanent internal energy flow inside the solitons, and finally the fact that single solitons can split into two or more [21].

One of the main manifestations of soliton-soliton interactions is their spatial "behaviour": a way in which the presence of other solitons influences the trajectory and dynamics of the soliton. For example, it was observed that

feedback solitons in resonators have several equilibrium distances between them [143]. Alternatively, dissipative laser solitons have been shown to exhibit complex oscillatory behaviour [144]. Moreover, dark cavity dissipative solitons were predicted to either merge or fly apart after a "spiral dance" in the case of a collision [145].

The aim of this part of the work was to gain insight onto how multiple solitons are formed and what soliton-soliton interactions are in the case of spatial polariton solitons.

§ 5.1 Experimental setup

The main modification to the setup is the introduction of a cigar shaped profile of the writing beam compared to the plain circular profile used in all previous experiments. This is shown schematically in figure 5.1. All other aspect of experimental arrangements remain the same, as shown in figure 4.1.

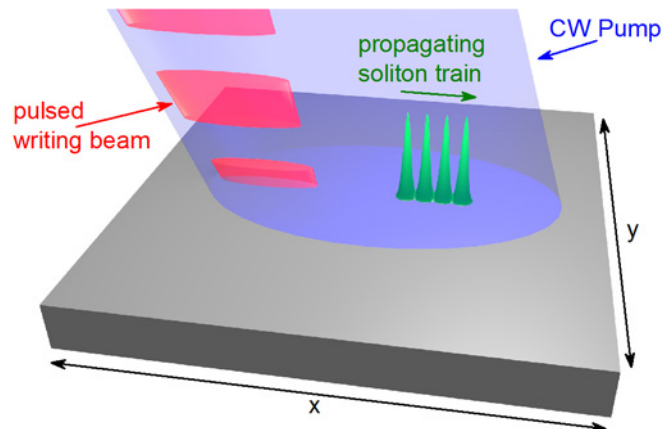


Figure 5.1. Schematic of soliton array excitation in the microcavity structure. The writing beam profile is stretched along the direction of propagation, X , in order to trigger a larger area compared to that in figure 3.1.

§ 5.2 Observation of soliton trains

A combination of σ_+ (or equally σ_-) polarised pump and writing beams provides the best experimental conditions for the observation of solitons, since a larger area can be covered in the bistable regime by the pump. To observe a different number of solitons in a soliton array (or train), the only parameter that was changed was the effective size of the writing beam. This was done by changing its power - the only parameter that can be changed without re-aligning the optics. The effective size can be changed by varying the writing beam power, since the soliton intensity is a nonlinear function of the writing beam intensity. As the writing beam power is increased from zero, at first only the central area of the writing beam is above the threshold for triggering solitons. Due to the Gaussian profile of the writing beam, a further increase in power will increase the area where its intensity is above the threshold.

A summary of observations of different numbers of trains is presented

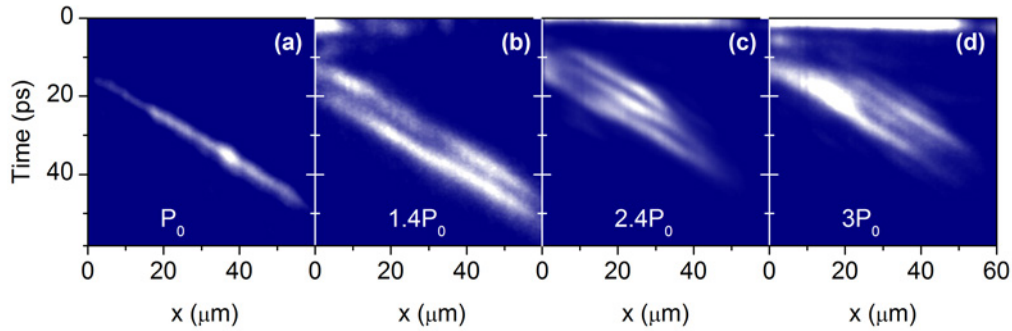


Figure 5.2. Streak camera images of a soliton (a) and soliton trains consisting of two (b), three (c) and four (d) solitons. $P_0 = 230 \mu\text{W}$ in this case.

in figure 5.2. At P_0 only a single soliton is seen. Then, as the writing beam power is increased, more solitons appear in a train. Up to 4 solitons were reliably observed. A reconstructed 2D image of a soliton train at a fixed time of 41 ps after the arrival of the writing beam is shown in figure 5.3.

Figures 5.4 and 5.5 show more detailed analysis of the train shown in figure 5.3 at a time of ≈ 41 ps. Figure 5.4 shows a streak camera image along the X -axis at $Y \approx 5 \mu\text{m}$. The green lines are a guide to the eye along the solitons' trajectories, and the red line shows a cut taken to investigate the soliton sizes and spacing in more detail, which is presented in figure 5.5. The intensity profile of the soliton train is fitted with four gaussian peaks (although ideally the soliton profile is not exactly Gaussian). The spacing between the solitons is $\approx 5 \mu\text{m}$, which is of the order of the characteristic healing length (as discussed in chapter 3). While the soliton sizes are approximately the same as observed before, they are presumably limited by the resolution of the setup.

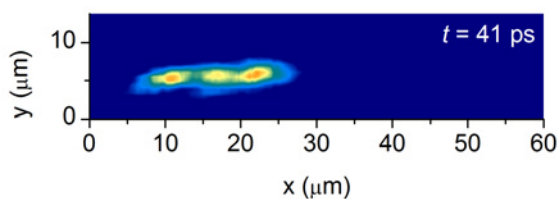


Figure 5.3. 2D pseudocolour image of a soliton train consisting of 4 solitons.

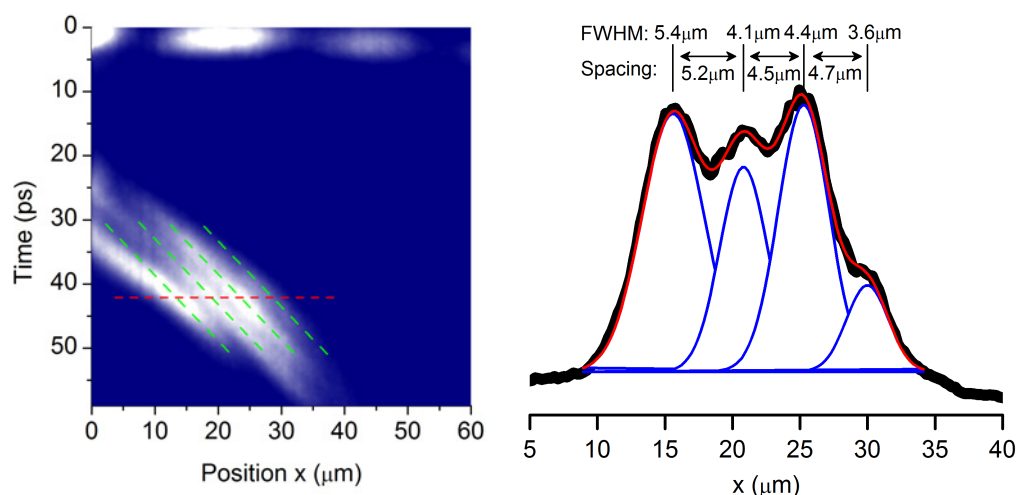


Figure 5.4. A streak camera image of the soliton train of four solitons taken along their propagation at $Y \approx 11 \mu\text{m}$.

Figure 5.5. Intensity profile of the soliton train (figure 5.4) at $\approx 41 \text{ ps}$.

§ 5.3 Soliton-soliton interactions

A soliton is a wavepacket consisting of coherent phase-locked harmonics. The actual phases of the soliton harmonics are determined by the phase of the writing beam pulse (see sections 3.3.4 and 3.4). It was shown that the coherence times of polaritons in the high density phase can be as long as 500 ps [65, 66] while solitons exist for up to 60 ps after the initiation. Therefore, during soliton propagation the coherence with the initial writing beam pulse should not be lost.¹ Moreover, as discussed in section 3.4,

¹In the case of soliton propagation, longer coherence times compared to static condensates can be expected due to different coupling to excitonic reservoirs.

soliton emission maintains coherence with the initial writing beam. Therefore, by probing the phases of solitons with the coherent writing beam, a way to investigate the interaction between solitons, which in our case travel in a 1D array, is created.

In this experiment, in contrast to that described in section 3.4, the control beam is created from the writing beam reflection after it hits the sample, and interference is observed on the streak camera rather than in the cavity, hence providing a non-invasive technique of studying the phases². The phase information extracted from the data relates only to a narrow range of soliton harmonics (see blue area in figure 3.13). This is in contrast to what was measured in atomic BEC [25], where a single condensate breaks up into several solitons. In this case, the macroscopic phase of each separate condensate (soliton) is well defined. The phase difference between adjacent solitons was measured to be π , which was attributed to a soliton stabilisation mechanism arising from the attractive interaction between atoms. Also coherent collisions of solitons in Kerr-type waveguide media in glass [146] showed that attraction and repulsion corresponds to $\Delta\phi = 0$ and π for the fundamental modes. Additionally, in carbon disulfide it was demonstrated that a $\pi/2$ phase difference leads to the most efficient energy transfer from one soliton to another, leading to their merging [147].

Further analysis was conducted mainly with the soliton train shown in figure 5.6. The first step is to trace the soliton trajectories from the real-space image. Figure 5.7 shows the tracing of soliton peaks by fitting multi-Gaussians to the soliton train profile for each point in time during its prop-

²Coherence contrast is greatly increased if only the relevant part of the soliton spectrum is cut for interference with a reference pulse taken from the writing beam. All experiments presented in this chapter were conducted when $k_{wb} < k_{pump}$ due to space limitations.

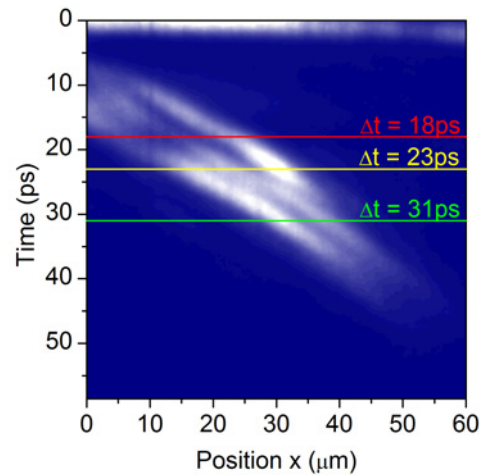


Figure 5.6. A slice of the soliton train consisting of three solitons used in figures 5.7, 5.8 and 5.9 showing times when phase shift was probed.

agation, which provides a reasonable fit. The peak positions as a function of time are shown in figure 5.8. It is observed that the soliton train undergoes two singularity events of merging solitons inside the train. As expected, real-space data provides a very poor estimate of the differences in adjacent soliton velocities, with errors being up to 500%. Phase measurement can provide the most accurate estimate for this.

To conduct phase measurement, the QWP from one of the arms of the interferometer was removed and emission was only detected in the circularly polarised basis (see figure 4.1). Then, the length of one of the arms was increased (by moving M3a mounted on a stage, see figure 4.1) so that the writing beam reflection coming from that arm arrives at the streak camera at the time when the soliton train emission arrives from the other arm. This results in interference pattern formation at the specified time. In this way it was possible to gradually probe the solitons' phases at different times during their propagation. Once the time of interest was selected by the po-

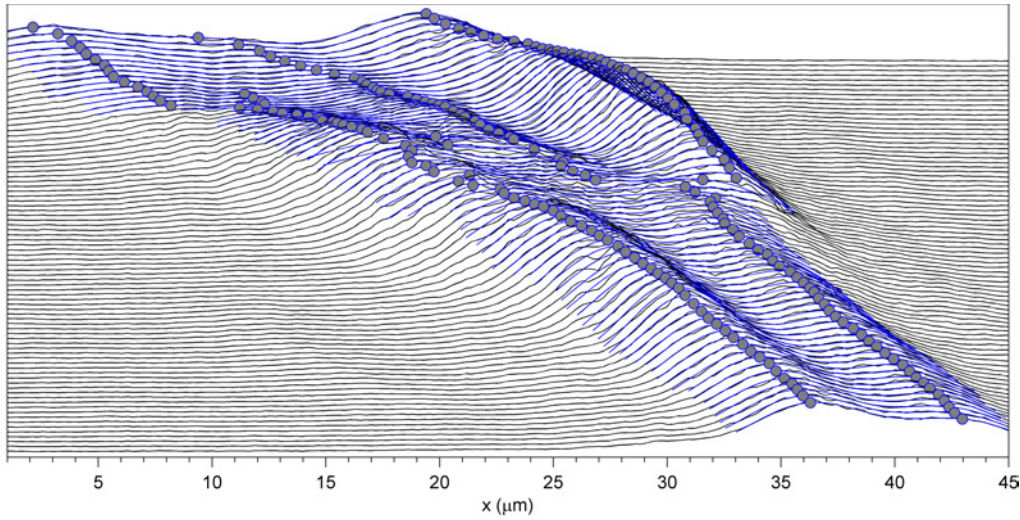


Figure 5.7. Multi-Gaussian fit to profile of soliton train. Black - raw data extracted from figure 5.6, blue - computed fit, blue circles computed position of soliton peaks.

sition of the M3a stage, the piezo stage was used to gradually shift M3a with subwavelength steps and for every step a separate streak camera image was recorded. Then, by comparing intensities in the centres of the solitons during the piezo cycle, it is possible to extract the phases of the separate solitons in the train.

A summary of the phase observations is shown in figure 5.9 and detailed fitting for each point on the graph is shown in figures 5.10, 5.11, 5.12, 5.13 and 5.14. Additionally, figure 5.6 shows a streak camera image of the train with three solitons, where the horizontal coloured lines indicate the times when soliton the phases were probed.

The difference between the phases of adjacent solitons are not constant as they propagate in an array as seen in figure 5.9. This change could be due to either a difference in the velocities of adjacent solitons or because of merging events, or both, since

$$\Delta\phi(t) = k\Delta x - \Delta\omega t. \quad (5.1)$$

Here Δx is the spatial separation and $\Delta\omega$ represents the difference of angular frequencies of the harmonics of the adjacent solitons. A merging event leads to a change of Δx with time. On the other hand, there could be a difference in velocities between solitons (leading to $\Delta\omega \neq 0$), because only in this case can they come close enough to undergo a merging event. The existing data is not sufficient to discriminate between the two effects.

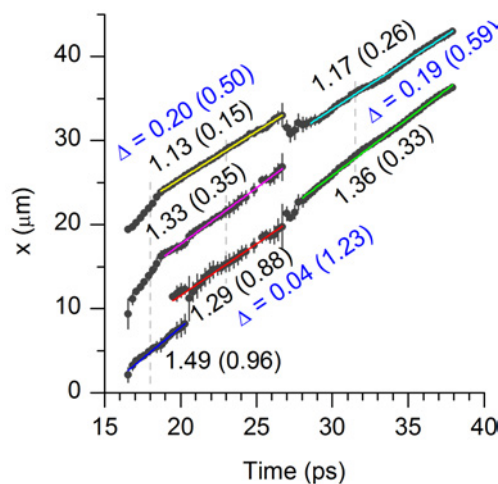


Figure 5.8. Soliton peak traces within the soliton train as function of time. Gray dots with error bars show fitted positions of soliton peaks, coloured lines provide fit to for velocity estimates in $\mu\text{m}/\text{ps}$, fitting errors are in brackets. Blue numbers show difference in velocities between adjacent solitons (errors are in brackets).

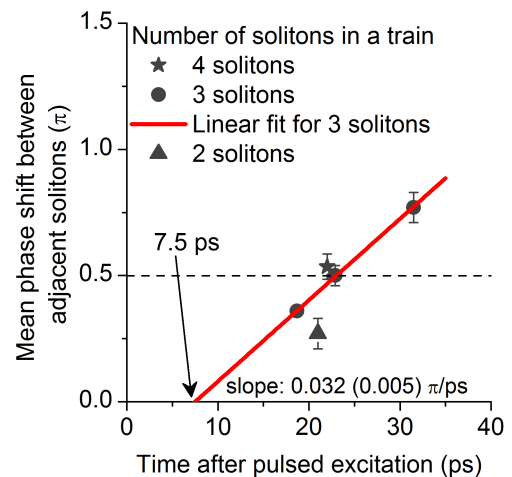


Figure 5.9. A summary of mean phase shift between adjacent solitons for different soliton trains (consisting of two, three and four solitons) as a function of time after the writing beam trigger.

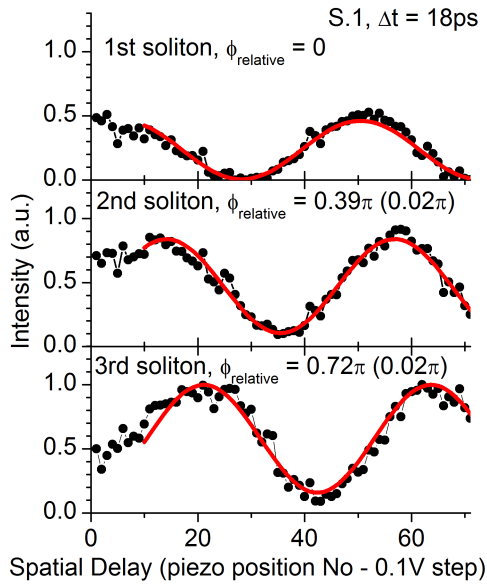


Figure 5.10. Interference pattern extracted for *three* solitons in a train at time $t = 18$ ps after the writing beam.

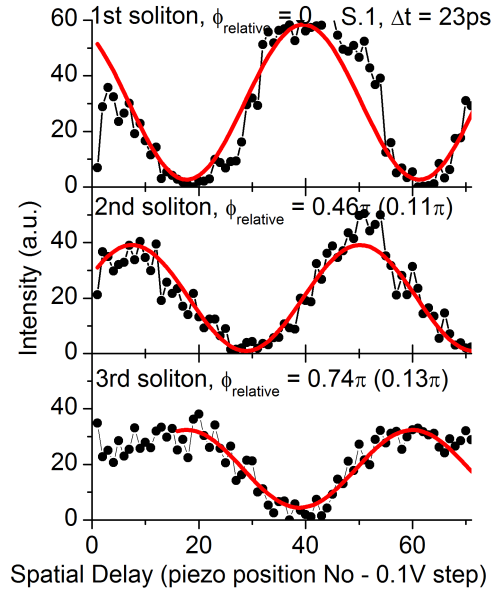


Figure 5.11. Interference pattern extracted for *three* solitons in a train at time $t = 23$ ps after the writing beam.

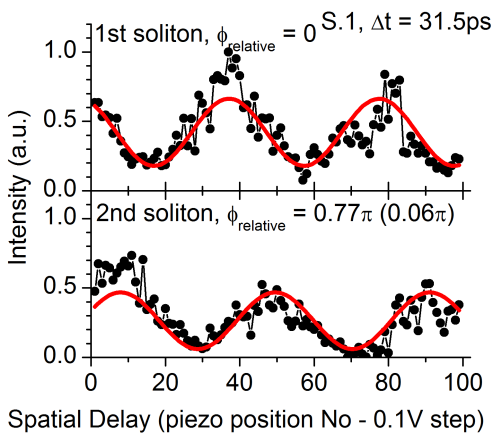


Figure 5.12. Interference pattern extracted for *three* solitons in a train at time $t = 31.5$ ps after the writing beam.

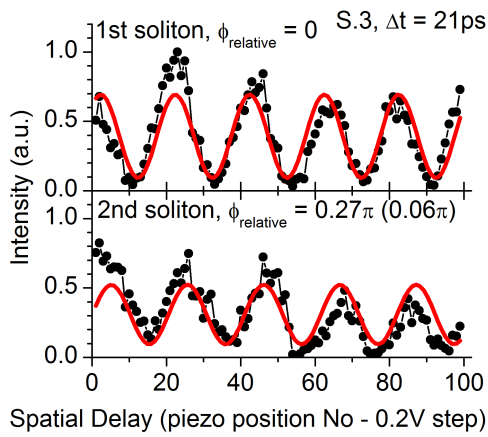


Figure 5.13. Interference pattern extracted for *two* solitons in a train at time $t = 21$ ps after the writing beam.

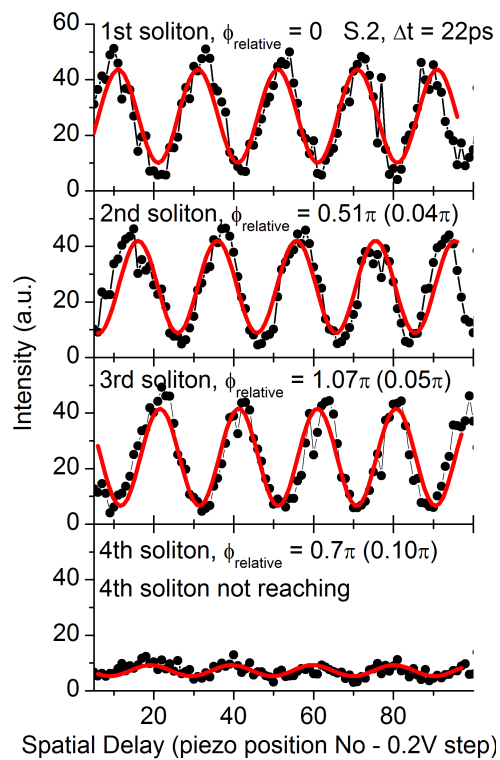


Figure 5.14. Interference pattern extracted for *four* solitons in a train at time $t = 22$ ps after the writing beam. The interference contrast of the last soliton is not sufficient.

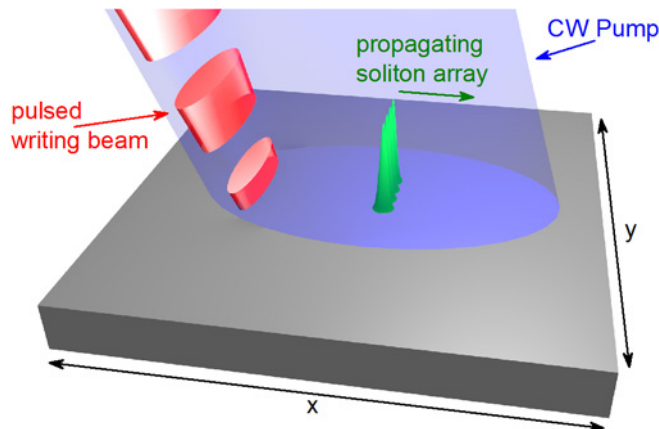


Figure 5.15. Possible future experiment with soliton arrays.

§ 5.4 Discussion and conclusions

In this chapter one type of possible soliton array – a soliton train – was demonstrated. The number of solitons in a train (up to four) is clearly defined by the writing beam size. Trigger population of polaritons, injected by the writing beam, clusters within areas of the size of the corresponding healing length $\approx 5 \mu\text{m}$, which then evolve into separate solitons.

Experimentally, the maximum number of solitons is limited by the relative size of the pump and the writing beam, and the fact that both of them have Gaussian profile.

There is a clear distinction between soliton train and so-called double- or multi-hump solitons[114]. For instance, in a double-hump soliton each peak has a size of $2\text{-}3 \mu\text{m}$ and the same spacing. In the current setup this cannot be resolved and will only look like a single peak. Moreover, peaks in double-hump solitons represent the same wavepacket and have the same set of phases, while in a soliton train each soliton evolves separately.

Further investigation of soliton arrays could be done with experiments where the writing beam profile is rotated by 90° (see figure 5.15, or coherently controlling individual solitons in a soliton train, by analogy with that shown in section 3.4.

Chapter 6

Conclusions and future plans

The work presented in this thesis aimed at exploring new properties of polariton systems with spatial hysteresis. Firstly, the formation of spin density rings was observed and characterised, which has exposed polariton polarisation multistability.

Secondly, the main focus of this work was on research on bright polariton solitons, which have been previously discussed theoretically. The properties of a single polariton soliton, such as its size, velocity, spectrum, sustainability, were studied in great detail. Thirdly, soliton polarisation properties were studied. The complex polarisation picture described in this work arising from polariton polarisation-dependent interactions. Finally, soliton patterns or trains were observed as expected for such a non-linear system.

Future experiments can possibly go in several directions. A separate study concerning interactions of separately created solitons can possibly open a new chapter in this research. Controlled collisions of un- or co- and

cross-polarised solitons, in addition to revealing fundamental insights in soliton physics of polaritons, will enable development of 'proof of concept' experiments for THz digital processing using polariton solitons.

Then spatial solitons should be studied in waveguides. The use of waveguides opens a way to modify the soliton path incorporating bends and turns, as opposed to a straight line in the case of a planar microcavity. 'Y'-splitter waveguide operation is particularly interesting, since it allows for precise control of collisions of two solitons. It is also a crucial part of 'proof of concept' for a soliton based classical OR gate.

Finally, this work has set a ground for studies of spatial soliton and patterns in microcavity polariton systems, allowing further investigations of both a fundamental and applied nature. Soliton pattern formation should be studied with more possible configurations for a better understanding of soliton-soliton interactions in these structures. An example of such an experiment is shown in figure 5.15.

Bibliography

- [1] Weisbuch, C., Nishioka, M., Ishikawa, A. & Arakawa, Y. Observation of the coupled exciton-photon mode splitting in a semiconductor quantum microcavity. *Phys. Rev. Lett.* **69**, 3314 – 3317 (1992).
- [2] Pekar, S. I. Theory of electromagnetic waves in a crystal in which excitons arise. *J. Exp. Teor. Fiz. USSR* **33**, 1022 – 1036 (1957).
- [3] Hopfield, J. J. Theory of the contribution of excitons to the complex dielectric constant of crystals. *Phys. Rev.* **112**, 1555 – 1567 (1958).
- [4] Agranovich, V. M. On the influence of reabsorption on the decay of fluorescence in molecular crystals. *Optica i Spectr.* **3**, 84 (1957).
- [5] Kasprzak, J. *et al.* Bose-Einstein condensation of exciton polaritons. *Nature Phys.* **443**, 409 – 414 (2006).
- [6] Amo, A. *et al.* Superfluidity of polaritons in semiconductor microcavities. *Nature Phys.* **5**, 805 – 810 (2009).
- [7] Stevenson, R. M. *et al.* Continuous wave observation of massive polariton redistribution by stimulated scattering in semiconductor microcavities. *Phys. Rev. Lett.* **85**, 3680 – 3683 (2000).

- [8] Lagoudakis, K. G. *et al.* Quantized vortices in an exciton-polariton condensate. *Nature Phys.* **4**, 706 – 710 (2008).
- [9] Amo, A. *et al.* Polariton superfluids reveal quantum hydrodynamic solitons. *Science* **332**, 1167 – 1170 (2011).
- [10] Russell, J. S. Report on waves. In *Rep. Br. Ass. Advmt Sci.*, vol. 14, 311 – 390, plus plates XLVII–LVII (London, 1845).
- [11] Apel, J. R., Ostrovsky, L. A., Stepanyants, Y. A. & Lynch, J. F. Internal solitons in the ocean. Tech. Rep., Woods Hole Oceanographic Institution (2006).
- [12] Jackson, C. R. *An Atlas of Internal Solitary-like Waves and their Properties* (Global Ocean Associates, Alexandria, Virginia, 2004), 2 edn.
- [13] Baines, P. G. *Topographic Effects in Stratified Flows*. Cambridge Monographs on Mechanics Series (Cambridge University Press, 1998).
- [14] Cummins, P. F., Vagle, S., Armi, L. & Farmer, D. M. Stratified flow over topography: Upstream influence and generation of nonlinear internal waves. *Proc. R. Soc. A* **459**, 1467 – 1487 (2003).
- [15] Porter, A. & Smyth, N. F. Modelling the morning glory of the gulf of carpentaria. *J. Fluid Mech.* **454**, 1 – 20 (2002).
- [16] Finkelstein, D. & Rubinstein, J. Ball lightning. *Phys. Rev.* **135**, A390 – A396 (1964).
- [17] Torruellas, W. E. *et al.* Observation of two-dimensional spatial solitary waves in a quadratic medium. *Phys. Rev. Lett.* **74**, 5036 – 5039 (1995).

- [18] Aitchison, J. S. *et al.* Observation of spatial optical solitons in a non-linear glass waveguide. *Opt. Lett.* **15**, 471 – 473 (1990).
- [19] Tikhonenko, V., Christou, J. & Luther-Davies, B. Three dimensional bright spatial soliton collision and fusion in a saturable nonlinear medium. *Phys. Rev. Lett.* **76**, 2698 – 2701 (1996).
- [20] Duree, G. C. *et al.* Observation of self-trapping of an optical beam due to the photorefractive effect. *Phys. Rev. Lett.* **71**, 533 – 536 (1993).
- [21] Sleky, G., Staliunas, K. & Weiss, C. O. Spatial localized structures in resonators with saturable absorber. *Opt. Commun.* **149**, 113 – 116 (1998).
- [22] Shih, M.-f., Segev, M. & Salamo, G. Three-dimensional spiraling of interacting spatial solitons. *Phys. Rev. Lett.* **78**, 2551 – 2554 (1997).
- [23] Duncan, D. Soliton on the Scott Russell Aqueduct on the Union Canal near Heriot-Watt University (1995). URL <http://www.ma.hw.ac.uk/solitons/soliton1b.html>.
- [24] Fly For Fun. Stratocumulus (Morning Glory) clouds (2011). URL <http://www.flickr.com/photos/flyforfun/5972754080/>.
- [25] Strecker, K. E., Partridge, G. B., Truscott, A. G. & Hulet, R. G. Formation and propagation of matter-wave soliton trains. *Nature* **417**, 150 – 153 (2002).
- [26] Mollenauer, L. F., Stolen, R. H. & Gordon, J. P. Experimental observation of picosecond pulse narrowing and solitons in optical fibers. *Phys. Rev. Lett.* **45**, 1095 – 1098 (1980).

- [27] Kivshar, Y. S. & Agrawal, G. P. *Optical Solitons: From Fibers to Photonic Crystals* (Academic Press, 2001).
- [28] Skryabin, D. V. & Gorbach, A. V. Colloquium: Looking at a soliton through the prism of optical supercontinuum. *Rev. Mod. Phys.* **82**, 1287 – 1299 (2010).
- [29] Kutz, J. N. Mode-locking of fiber lasers via nonlinear mode-coupling. In Akhmediev, N. & Ankiewicz, A. (eds.) *Dissipative Solitons*, vol. 661 of *Lecture Notes in Physics*, 241 – 265 (Springer Berlin Heidelberg, 2005).
- [30] Khaykovich, L. *et al.* Formation of a matter-wave bright soliton. *Science* **296**, 1290 – 1293 (2002).
- [31] Weiss, C. O., Vaupel, M., Staliunas, K., Slekyš, G. & Taranenko, V. B. Solitons and vortices in lasers. *Appl. Phys. B: Lasers Opt.* **68**, 151 – 168 (1999).
- [32] Taranenko, V. B., Ahlers, F. J. & Pierz, K. Coherent switching of semiconductor resonator solitons. *Appl. Phys. B* **75**, 75 – 77 (2002).
- [33] Taranenko, V. B., Slekyš, G. & Weiss, C. O. Spatial resonator solitons. *Chaos* **13**, 777 – 790 (2003).
- [34] Ackemann, T., Firth, W. J. & Oppo, G.-L. Chapter 6. Fundamentals and applications of spatial dissipative solitons in photonic devices. In E. Arimondo, P. R. B. & Lin, C. C. (eds.) *Advances in Atomic, Molecular and Optical Physics*, vol. 57 of *Advances In Atomic, Molecular and Optical Physics*, 323 – 421 (Academic Press, 2009).

- [35] Skolnick, M. S., Fisher, T. A. & Whittaker, D. M. Strong coupling phenomena in quantum microcavity structures. *Semiconductor Science and Technology* **13**, 645 – 669 (1998).
- [36] Kavokin, A., Baumberg, J. J., Malpuech, G. & Laussy, F. P. *Microcavities*. Semiconductor science and technology (Oxford University Press, 2007).
- [37] Houdré, R. *et al.* Measurement of cavity-polariton dispersion curve from angle-resolved photoluminescence experiments. *Phys. Rev. Lett.* **73**, 2043 – 2046 (1994).
- [38] Whittaker, D. M. *et al.* Motional narrowing in semiconductor microcavities. *Phys. Rev. Lett.* **77**, 4792 – 4795 (1996).
- [39] Khitrova, G., Gibbs, H. M., Jahnke, F., Kira, M. & Koch, S. W. Non-linear optics of normal-mode-coupling semiconductor microcavities. *Rev. Mod. Phys.* **71**, 1591 – 1639 (1999).
- [40] Einstein, A. Quantentheorie des einatomigen idealen Gases. Zweite Abhandlung. *Sitzungsberichte der Preussischen Akademie der Wissenschaften (Berlin). Physikalisch-mathematische Klasse* 3 – 14 (1925).
- [41] Bose, S. N. Plancks Gesetz und Lichtquantenhypothese. *Z. Physik* **26**, 178 (1924).
- [42] Fermi, E. Zur Quantelung des Idealen Einatomigen Gases. *Z. Physik* **36**, 902 (1926).
- [43] Griffin, A. A brief history of our understanding of BEC: from Bose to Beliaev. *arXiv:cond-mat/9901123v1* (1999).

- [44] Kapitza, P. S. Viscosity of liquid helium below the λ -point. *Nature* **141**, 74 (1938).
- [45] Allen, J. F. & Misener, A. D. Flow of liquid helium II. *Nature* **141**, 75 (1938).
- [46] London, F. On the Bose-Einstein condensation. *Phys. Rev.* **54**, 947 – 954 (1938).
- [47] Tisza, L. Transport phenomena in helium II. *Nature* **141**, 913 (1938).
- [48] Landau, L. D. The theory of superfluidity of helium II. *J. Phys. USSR* **5**, 71 (1941).
- [49] Landau, L. D. & Lifshitz, E. M. *Statisticheskaya Fizika* (Fizmatgiz, Moscow, 1951).
- [50] Penrose, O. On the quantum mechanics of helium II. *Philos. Mag.* **42**, 1373 – 1377 (1951).
- [51] Anderson, M. H., Ensher, J. R., Matthews, M. R., Wieman, C. E. & Cornell, E. A. Observation of Bose-Einstein condensation in a dilute atomic vapor. *Science* **269**, 198–201 (1995).
- [52] Butov, L. V., Lai, C. W., Ivanov, A. L., Gossard, A. C. & Chemla, D. S. Towards Bose-Einstein condensation of excitons in potential traps. *Nature* **417**, 47 – 52 (2002).
- [53] Butov, L. V., Gossard, A. C. & Chemla, D. S. Macroscopically ordered state in an exciton system. *Nature* **418**, 751 – 754 (2002).
- [54] Klaers, J., Schmitt, J., Vewinger, F. & Weitz, M. Bose-Einstein condensation of photons in an optical microcavity. *Nature* **468**, 545 – 548 (2010).

- [55] Laikhtman, B. Are excitons really bosons? *J. Phys.: Condens. Matter* **19** (2007).
- [56] Landau, L. D. & Lifshitz, E. M. *Statistical Physics*, vol. 5 of *Course of Theoretical Physics* (Butterworth-Heinemann, 1980), 3 edn. Revised and enlarged by E. M. Lifshitz and L. P. Pitaevskii.
- [57] Pau, S., Björk, G., Jacobson, J., Cao, H. & Yamamoto, Y. Stimulated emission of a microcavity dressed exciton and suppression of phonon scattering. *Phys. Rev. B* **51**, 7090 – 7100 (1995).
- [58] Tassone, F., Piermarocchi, C., Savona, V., Quattropani, A. & Schwendimann, P. Photoluminescence decay times in strong-coupling semiconductor microcavities. *Phys. Rev. B* **53**, R7642 – R7645 (1996).
- [59] Tassone, F., Piermarocchi, C., Savona, V., Quattropani, A. & Schwendimann, P. Bottleneck effects in the relaxation and photoluminescence of microcavity polaritons. *Phys. Rev. B* **56**, 7554 – 7563 (1997).
- [60] Tartakovskii, A. I. *et al.* Relaxation bottleneck and its suppression in semiconductor microcavities. *Phys. Rev. B* **62**, 2283 – 2286 (2000).
- [61] Pitaevskii, L. P. & Stringari, S. *Bose-Einstein condensation*. Monographs on Physics (Oxford University Press, 2003).
- [62] Nelsen, B. *et al.* Coherent flow and trapping of polariton condensates with long lifetime. *arXiv:1209.4573v1 [cond-mat.quant-gas]* (2012).
- [63] Butov, L. V. & Kavokin, A. V. The behaviour of exciton-polaritons. *Nature Photon.* **6**, 2 (2012).

- [64] Deveaud-Plédran, B. The behaviour of exciton-polaritons. *Nature Photon.* **6**, 205 (2012).
- [65] Love, A. P. D. *et al.* Intrinsic decoherence mechanisms in the microcavity polariton condensate. *Phys. Rev. Lett.* **101**, 067404 (2008).
- [66] Krizhanovskii, D. N. *et al.* Dominant effect of polariton-polariton interactions on the coherence of the microcavity optical parametric oscillator. *Phys. Rev. Lett.* **97**, 097402 (2006).
- [67] Spano, R. *et al.* Build up of off-diagonal long-range order in microcavity exciton-polaritons across the parametric threshold. *arXiv:1111.4894v1 [cond-mat.mes-hall]* (2011).
- [68] Balili, R., Hartwell, V., Snoke, D., Pfeiffer, L. & West, K. Bose-Einstein condensation of microcavity polaritons in a trap. *Science* **316**, 1007 – 1010 (2007).
- [69] Bajoni, D. *et al.* Polariton laser using single micropillar GaAs-GaAlAs semiconductor cavities. *Phys. Rev. Lett.* **100**, 047401 (2008).
- [70] Wertz, E. *et al.* Spontaneous formation and optical manipulation of extended polariton condensates. *Nature Phys.* **6**, 860 – 864 (2010).
- [71] Ferrier, L. *et al.* Interactions in confined polariton condensates. *Phys. Rev. Lett.* **106**, 126401 (2011).
- [72] Savvidis, P. G. *et al.* Angle-resonant stimulated polariton amplifier. *Phys. Rev. Lett.* **84**, 1547 – 1550 (2000).
- [73] Ciuti, C., Schwendimann, P., Deveaud, B. & Quattropani, A. Theory of the angle-resonant polariton amplifier. *Phys. Rev. B* **62**, 4825 – 4828 (2000).

- [74] Kundermann, S. *et al.* Coherent control of polariton parametric scattering in semiconductor microcavities. *Phys. Rev. Lett.* **91**, 107402 (2003).
- [75] Krizhanovskii, D. N. *et al.* Self-organization of multiple polariton-polariton scattering in semiconductor microcavities. *Phys. Rev. B* **77**, 115336 (2008).
- [76] Whittaker, D. M. Effects of polariton-energy renormalization in the microcavity optical parametric oscillator. *Phys. Rev. B* **71**, 115301 (2005).
- [77] Baas, A., Karr, J.-P., Eleuch, H. & Giacobino, E. Optical bistability in semiconductor microcavities. *Phys. Rev. A* **69**, 023809 (2004).
- [78] Tredicucci, A., Chen, Y., Pellegrini, V., Börger, M. & Bassani, F. Optical bistability of semiconductor microcavities in the strong-coupling regime. *Phys. Rev. A* **54**, 3493 – 3498 (1996).
- [79] Gippius, N. A., Tikhodeev, S. G., Kulakovskii, V. D., Krizhanovskii, D. N. & Tartakovskii, A. I. Nonlinear dynamics of polariton scattering in semiconductor microcavity: bistability vs stimulated scattering. *Europhys. Lett.* **67**, 5 (2003).
- [80] Baas, A., Karr, J.-P., Romanelli, M., Bramati, A. & Giacobino, E. Optical bistability in semiconductor microcavities in the nondegenerate parametric oscillation regime: Analogy with the optical parametric oscillator. *Phys. Rev. B* **70**, 161307 (2004).
- [81] Whittaker, D. M. Effects of polariton-energy renormalization in the microcavity optical parametric oscillator. *Phys. Rev. B* **71**, 115301 (2005).

- [82] Wouters, M. & Carusotto, I. Goldstone mode of optical parametric oscillators in planar semiconductor microcavities in the strong-coupling regime. *Phys. Rev. A* **76**, 043807 (2007).
- [83] Renucci, P. *et al.* Microcavity polariton spin quantum beats without a magnetic field: A manifestation of coulomb exchange in dense and polarized polariton systems. *Phys. Rev. B* **72**, 075317 (2005).
- [84] Ciuti, C., Savona, V., Piermarocchi, C., Quattropani, A. & Schwendimann, P. Role of the exchange of carriers in elastic exciton-exciton scattering in quantum wells. *Phys. Rev. B* **58**, 7926 – 7933 (1998).
- [85] Gippius, N. A. *et al.* Polarization multistability of cavity polaritons. *Phys. Rev. Lett.* **98**, 236401 (2007).
- [86] Liew, T. C. H., Kavokin, A. V. & Shelykh, I. A. Optical circuits based on polariton neurons in semiconductor microcavities. *Phys. Rev. Lett.* **101**, 016402 (2008).
- [87] Amo, A. *et al.* Exciton - polariton spin switches. *Nature. Photon.* **4**, 361 – 366 (2010).
- [88] Shelykh, I. A., Liew, T. C. H. & Kavokin, A. V. Spin rings in semiconductor microcavities. *Phys. Rev. Lett.* **100**, 116401 (2008).
- [89] Krizhanovskii, D. N. *et al.* Effect of interactions on vortices in a nonequilibrium polariton condensate. *Phys. Rev. Lett.* **104**, 126402 (2010).
- [90] Onsager, L. Statistical hydrodynamics. *Il Nuovo Cimento Series 9* **6**, 279 – 287 (1949).

- [91] Feynman, R. P. Application of quantum mechanics to liquid helium. In Gorter, C. J. (ed.) *Progress in Low Temperature Physics*, vol. 1, chap. 2, 17 – 53 (North-Holland, Amsterdam, 1955).
- [92] Lagoudakis, K. G. *et al.* Observation of half-quantum vortices in an exciton-polariton condensate. *Science* **326**, 974 – 976 (2009).
- [93] Sanvitto, D. *et al.* Persistent currents and quantized vortices in a polariton superfluid. *Nature Phys.* **6**, 527 – 533 (2010).
- [94] Nardin, G. *et al.* Hydrodynamic nucleation of quantized vortex pairs in a polariton quantum fluid. *Nature Phys.* **7**, 635 – 641 (2011).
- [95] Roumpos, G. *et al.* Single vortex-antivortex pair in an exciton-polariton condensate. *Nature Phys.* **7**, 129 – 133 (2011).
- [96] Bennett, C. R., Boussiakou, L. G. & Babiker, M. Electric and magnetic monopoles in rotating Bose-Einstein condensates. *Phys. Rev. A* **64**, 061602 (2001).
- [97] Solnyshkov, D., Flayac, H. & Malpuech, G. Stable magnetic monopoles in spinor polariton condensates. *Phys. Rev. B* **85**, 073105 (2012).
- [98] Bogoliubov, N. N. On the theory of superfluidity. *J. Phys. USSR* **11**, 23 (1947).
- [99] Carusotto, I., Hu, S. X., Collins, L. A. & Smerzi, A. Bogoliubov-Čerenkov radiation in a Bose-Einstein condensate flowing against an obstacle. *Phys. Rev. Lett.* **97**, 260403 (2006).

- [100] Keeling, J. Response functions and superfluid density in a weakly interacting Bose gas with nonquadratic dispersion. *Phys. Rev. B* **74**, 155325 (2006).
- [101] Ciuti, C. & Carusotto, I. Quantum fluid effects and parametric instabilities in microcavities. *Phys. Status Solidi B* **242**, 2224 – 2245 (2005).
- [102] Wouters, M. & Carusotto, I. Excitations in a nonequilibrium Bose-Einstein condensate of exciton polaritons. *Phys. Rev. Lett.* **99**, 140402 (2007).
- [103] Pigeon, S., Carusotto, I. & Ciuti, C. Hydrodynamic nucleation of vortices and solitons in a resonantly excited polariton superfluid. *Phys. Rev. B* **83**, 144513 (2011).
- [104] El, G. A., Gammal, A. & Kamchatnov, A. M. Oblique dark solitons in supersonic flow of a Bose-Einstein condensate. *Phys. Rev. Lett.* **97**, 180405 (2006).
- [105] Kamchatnov, A. M. & Pitaevskii, L. P. Stabilization of solitons generated by a supersonic flow of Bose-Einstein condensate past an obstacle. *Phys. Rev. Lett.* **100**, 160402 (2008).
- [106] Flayac, H., Solnyshkov, D. D. & Malpuech, G. Oblique half-solitons and their generation in exciton-polariton condensates. *Phys. Rev. B* **83**, 193305 (2011).
- [107] Hivet, R. *et al.* Half-solitons in a polariton quantum fluid behave like magnetic monopoles. *Nature Phys.* **8**, 724 – 728 (2012).
- [108] Freixanet, T., Sermage, B., Tiberj, A. & Thierry-Mieg, V. Propagation of excitonic polaritons in a microcavity. *Phys. Status Solidi A* **178**, 133 – 138 (2000).

- [109] Amo, A. *et al.* Collective fluid dynamics of a polariton condensate in a semiconductor microcavity. *Nature* **457**, 291 – 295 (2009).
- [110] Barland, S. *et al.* Cavity solitons as pixels in semiconductor microcavities. *Nature* **419**, 699 – 702 (2002).
- [111] Taranenko, V., Ganne, I., Kuszelewicz, R. & Weiss, C. Spatial solitons in a semiconductor microresonator. *Appl. Phys. B* **72**, 377 – 380 (2001).
- [112] Spinelli, L., Tissoni, G., Brambilla, M., Prati, F. & Lugiato, L. Spatial solitons in semiconductor microcavities. *Phys. Rev. A* **58**, 2542 – 2559 (1998).
- [113] Taranenko, V., Weiss, C. & Schpers, B. From coherent to incoherent hexagonal patterns in semiconductor resonators. *Phys. Rev. A* **65**, 138121 – 138124 (2002).
- [114] Egorov, O. A., Gorbach, A. V., Lederer, F. & Skryabin, D. V. Two-dimensional localization of exciton polaritons in microcavities. *Phys. Rev. Lett.* **105**, 073903 (2010).
- [115] Egorov, O. A., Skryabin, D. V., Yulin, A. V. & Lederer, F. Bright cavity polariton solitons. *Phys. Rev. Lett.* **102**, 153904 (2009).
- [116] Egorov, O. A., Skryabin, D. V. & Lederer, F. Polariton solitons due to saturation of the exciton-photon coupling. *Phys. Rev. B* **82**, 165326 (2010).
- [117] Yulin, A. V., Egorov, O. A., Lederer, F. & Skryabin, D. V. Dark polariton solitons in semiconductor microcavities. *Phys. Rev. A* **78**, 061801 (2008).

- [118] Larionova, Y., Stolz, W. & Weiss, C. O. Optical bistability and spatial resonator solitons based on exciton-polariton nonlinearity. *Opt. Lett.* **33**, 321 – 323 (2008).
- [119] Talanina, I. B., Collins, M. A. & Agranovich, V. M. Polariton trapping by a soliton near an excitonic resonance. *Phys. Rev. B* **49**, 1517 – 1520 (1994).
- [120] Talanina, I. B. Polariton solitons in semiconductors: Quantitative study. *Solid State Commun.* **97**, 273 – 277 (1996).
- [121] Sarkar, D. *et al.* Polarization bistability and resultant spin rings in semiconductor microcavities. *Phys. Rev. Lett.* **105**, 216402 (2010).
- [122] Kitano, M., Yabuzaki, T. & Ogawa, T. Optical tristability. *Phys. Rev. Lett.* **46**, 926–929 (1981).
- [123] Cecchi, S., Giusfredi, G., Petriella, E. & Salieri, P. Observation of optical tristability in sodium vapors. *Phys. Rev. Lett.* **49**, 1928 – 1931 (1982).
- [124] Wouters, M. Resonant polariton-polariton scattering in semiconductor microcavities. *Phys. Rev. B* **76**, 045319 (2007).
- [125] Krizhanovskii, D. N. *et al.* Rotation of the plane of polarization of light in a semiconductor microcavity. *Phys. Rev. B* **73**, 073303 (2006).
- [126] Sanvitto, D. *et al.* Spatial structure and stability of the macroscopically occupied polariton state in the microcavity optical parametric oscillator. *Phys. Rev. B* **73**, 241308 (2006).

- [127] Krizhanovskii, D. N. *et al.* Impact of exciton localization on the optical non-linearities of cavity polaritons. *Solid State Commun.* **119**, 435 – 439 (2001).
- [128] Inoue, J.-i., Brandes, T. & Shimizu, A. Renormalized bosonic interaction of excitons. *Phys. Rev. B* **61**, 2863 – 2873 (2000).
- [129] Paraïso, T. K., Wouters, M., Léger, Y., Morier-Genoud, F. & Deveaud-Plédran, B. Multistability of a coherent spin ensemble in a semiconductor microcavity. *Nature Mater.* **9**, 655 – 660 (2010).
- [130] Adrados, C. *et al.* Spin rings in bistable planar semiconductor microcavities. *Phys. Rev. Lett.* **105**, 216403 (2010).
- [131] Sich, M. *et al.* Observation of bright polariton solitons in a semiconductor microcavity. *Nature Photon.* **6**, 50 – 55 (2012).
- [132] Eiermann, B. *et al.* Bright Bose-Einstein gap solitons of atoms with repulsive interaction. *Phys. Rev. Lett.* **92**, 230401 (2004).
- [133] Fleischer, J. W., Segev, M., Efremidis, N. K. & Christodoulides, D. N. Observation of two-dimensional discrete solitons in optically induced nonlinear photonic lattices. *Nature* **422**, 147 – 150 (2003).
- [134] Gibbs, H. M., Khitrova, G. & Koch, S. W. Exciton-polariton light-semiconductor coupling effects. *Nature Photon.* **5**, 275 – 282 (2011).
- [135] Akhmediev, N. & Ankiewicz, A. (eds.) *Dissipative solitons*, vol. 661 of *Lecture Notes in Physics* (Springer, 2005).
- [136] Saffman, M. & Skryabin, D. V. Coupled propagation of light and matter waves: Solitons and transverse instabilities. In Trillo, S. & Torruellas, W. (eds.) *Spatial Solitons* (Springer, 2001).

- [137] Carusotto, I. & Ciuti, C. Probing microcavity polariton superfluidity through resonant Rayleigh scattering. *Phys. Rev. Lett.* **93**, 166401 (2004).
- [138] Langbein, W. Spontaneous parametric scattering of microcavity polaritons in momentum space. *Phys. Rev. B* **70**, 205301 (2004).
- [139] Liew, T. C. H., Kavokin, A. V. & Shelykh, I. A. Excitation of vortices in semiconductor microcavities. *Phys. Rev. B* **75**, 241301 (2007).
- [140] Pedaci, F. *et al.* All-optical delay line using semiconductor cavity solitons. *Appl. Phys. Lett.* **92**, 011101 (2008).
- [141] Langbein, W. *et al.* Polarization beats in ballistic propagation of exciton-polaritons in microcavities. *Phys. Rev. B* **75**, 075323 (2007).
- [142] Skryabin, D. V. Private communication.
- [143] Schäpers, B., Feldmann, M., Ackemann, T. & Lange, W. Interaction of localized structures in an optical pattern-forming system. *Phys. Rev. Lett.* **85**, 748–751 (2000).
- [144] Rozanov, N. N., Fedorov, S. V. & Shatsev, A. N. Nonstationary multi-vortex and fissionable soliton-like structures of laser radiation. *Optics and Spectroscopy (English translation of Optika i Spektroskopiya)* **95**, 843 – 848 (2003).
- [145] Scroggie, A. J., McSloy, J. M. & Firth, W. J. Self-propelled cavity solitons in semiconductor microcavities. *Phys. Rev. E* **66**, 036607 (2002).
- [146] Aitchison, J. S. *et al.* Experimental observation of spatial soliton interactions. *Opt. Lett.* **16**, 15 – 17 (1991).

- [147] Shalaby, M., Reynaud, F. & Barthelemy, A. Experimental observation of spatial soliton interactions with a $\pi/2$ relative phase difference. *Opt. Lett.* **17**, 778 – 780 (1992).